

# Theoretical and Experimental Investigations in MEMS-Based Force-Detected NMR

Thesis by  
Ramez Ahmed Elgammal

In Partial Fulfillment of the Requirements  
for the Degree of  
Doctor of Philosophy



California Institute of Technology  
Pasadena, California

2005  
(Defended May 24, 2005)

© 2005

Ramez Ahmed Elgammal

All Rights Reserved

To my parents and to Sara

# Acknowledgements

As my graduate career comes to an end, I am duly reminded of the tremendously talented group of scientists and engineers I have met at Caltech. While it is impossible to properly thank all those that contributed to and enriched my experience at Caltech, I would like to point out those that impacted me the most.

First and foremost, I would like to thank my advisor Dan Weitekamp. Dan took me in his group even though I came in as a synthetic chemist and gave me the opportunity to work on very interesting projects spanning many disciplines. Dan is a vast source of knowledge, is impressively creative, and had remarkable patience for my erratic work style.

In the Weitekamp group, I had a very fruitful interaction with Dr. Bruce Lambert. While we never worked on a project together, Bruce was always ready to talk about my project or about physics in general. His approach to problem solving is amazing. Outside the lab, Bruce provided enough distractions to keep me sane. It may be possible that we took too many coffee breaks; my guess would be over 2000 of them. Bruce has become a great friend and I'll certainly miss all the fun we had. Thanks for all your help! Other former Weitekamp group members I would like to thank include: Dr. Jim Kempf (thanks for getting me started on the optical project), Dr. Gary Leskowitz (for never hesitating to answer my questions remotely), and Dr. Lou Madsen. Valerie Norton and Mark Butler provided an interesting dynamic to the lab and I wish you both the best of luck in wrapping up your degrees.

I would also like to thank my various committee members: Professors Mitchio Okumura, Bob Grubbs, Harry Gray, Vince McKoy, and Peter Dervan. My committee has given me very helpful feedback throughout all of the examinations. I sincerely appreciate the advice and guidance Harry has given me. He has made me feel like part of his group since I first arrived at Caltech. Thanks for all your help Harry in writing letters and having your door open.

Shane Foister impressed me from the first day of grad school on. You've been a great friend throughout the years. Thanks for teaching me about handicapping horse racing, for being a college basketball fanatic, and for being argumentative.

The Bercaw group has been a second home to me. I'd like to thank my classmate Susan Schofer for always making me laugh. A special thanks to Dave Weinberg for all of the good times. I'd say your only fault is being a Duke fan. Dr. Parisa Mehrkokavandi has been a fun hiking buddy and I know you'll do an amazing job at UBC. I still have a perfect record against you in hearts. So I'll document it here so you don't forget. Dr. Jonathan Owen has been a blast. I'll be waiting for him to make a name for himself very soon.

I also had the pleasure of knowing Dr. Shantanu Sharma. While he is adamant about blaming me for ending up at Caltech, it did work out for the best. Shantanu is a man of many talents and I expect to have a partial share of your empire. Dr. William Wehbi was always a source of constant optimism. Thanks for re-inspiring my interest in Middle Eastern cuisine and helping me practice my Arabic. Dr. Ali Husain is another remarkable scientist. I enjoyed all of our discussions about science, economics, and policy.

My family is due a very big thank you for putting up with me not calling when I really should have. This thesis is dedicated in part to my parents and all of my sisters: Tammie, Temara, Suzanne, and Sonya. I am truly lucky to have two wonderful parents. My father, Dr. Attia Elgammal, was my first and most inspiring teacher of mathematics and science. It was he that truly got me psyched about science at a very early age. I love you very much dad, and without you this wouldn't have been possible. Thanks mom for always being there to help when I was growing up. I miss and love you tremendously. A very happy note during my stay at Caltech was the marriage of my sister Temara and me becoming an uncle. I wish I had more time to see you; you're just down the road. But I know that you, Khalid, and Dina will be very happy.

Finally, I would like to thank Dr. Sara Klamo for all of her support and companionship over the years. Thank you for being my best friend, for always making me smile, and for providing the balance in my life that I very much need. I look forward to our future together.

# Abstract

This thesis describes a method of mechanically detecting magnetic resonance. The detector consists of a ferromagnet harmonically bound to a mechanical resonator and measures a magnetic force of interaction with a nearby sample via dipole-dipole coupling. Flexural modes of vibration of the resonator are induced by inversion of the sample magnetization at the mechanical resonance frequency of the device. In this method, a nominally homogeneous field at the sample allows coherent spectroscopy over the entire sample volume.

Sensitivity analyses suggest that encoding an NMR signal into mechanical oscillations favors inductive detection at the micron scale and below with Brownian motion of the detection being the predominant source of noise and azimuthal eddy currents being the predominant source of damping. As such, the design issues of a MEMS-based spectrometer optimized for 50 micron samples have been investigated. Finite element methods were used and the results for magnetic softening effects, mechanical stresses, field homogeneity, magnet design, radiofrequency excitation, and the utility of capacitive transduction to provide tuning of the oscillator's mechanical resonance frequency and active shimming are discussed. A piezoelectrically actuated microvalve is proposed as part of a microfluidic device to allow shuttling of liquid samples. We present a new means of fiber-optic interferometry for geometrically confined regions in which the light exits transverse to core axis. The use of a composite magnetic array of packed nanoparticles may reduce the damping by  $10^4$ .

The portability of the spectrometer will allow in situ spectroscopy and towards that end  $^{14}\text{N}$  overtone experiments were simulated. Force-detection of this transition is superior not only at reduced size scales, but over a broad range of magnetic field strengths. The line narrowing observed by detecting the overtone transition should allow detailed spectroscopic analysis not possible by observing the quadrupolar broadened first-order spectrum. Simulations for a representative class of tholins suggest that the overtone linewidths is of order tens of kHz.

We conclude by discussing the feasibility of nanoscale NMR using torque detection of spin-locked, transverse magnetization, include a derivation of the signal-to-noise and detector optimization, and comment on the fundamental limitations of quantum statistical noise.

# Contents

<b>Acknowledgements</b>	<b>iv</b>
<b>Abstract</b>	<b>vi</b>
<b>1 Introduction</b>	<b>1</b>
1.1 NMR Physics . . . . .	2
1.1.1 Classical Mechanical Description . . . . .	2
1.1.2 Quantum Mechanical Description . . . . .	4
1.2 NMR Spectroscopy . . . . .	6
1.3 Force-Detected NMR . . . . .	8
1.3.1 Introduction . . . . .	8
1.3.2 Homogeneous Fields . . . . .	10
1.3.3 Theory . . . . .	11
1.3.4 Encoding NMR into Mechanical Oscillations . . . . .	13
1.3.5 Signal-to-Noise Analysis . . . . .	14
1.3.6 Scaling Arguments . . . . .	17
1.4 Thesis Outline . . . . .	19
<b>2 Design of MEMS-Based Force-Detected Spectrometer</b>	<b>20</b>
2.1 General Design Issues . . . . .	21
2.2 The Finite Element Method . . . . .	21
2.3 Magnetic Assembly . . . . .	23
2.3.1 Detector and Annular Magnet . . . . .	23
2.3.1.1 Magnetic Softening . . . . .	23
2.3.1.2 Detector Optimization . . . . .	25
2.3.1.3 Magnetic Materials . . . . .	30

2.3.2	Static Magnetic Field . . . . .	32
2.3.3	Field Homogeneity and Lineshape Analysis . . . . .	34
2.4	Mechanical Oscillator Design . . . . .	36
2.4.1	Rectangular Beams . . . . .	36
2.4.2	Capacitive Transduction . . . . .	39
2.4.3	Resonator Characterization . . . . .	42
2.5	Damping . . . . .	43
2.5.1	Air Damping . . . . .	43
2.5.2	Thermoelastic Damping . . . . .	44
2.5.3	Clamping Losses . . . . .	45
2.5.4	Surface Damping . . . . .	47
2.5.5	Eddy Current Damping . . . . .	47
2.6	Radiofrequency Excitation . . . . .	52
2.6.1	Spin Inversion . . . . .	52
2.6.2	Excitation Coil . . . . .	54
2.7	Sample Transport . . . . .	57
2.8	Detection of Oscillator Motion . . . . .	61
2.8.1	Transverse Fiber-optic Interferometry . . . . .	61
2.8.2	Other Displacement Sensing Methods . . . . .	69
2.9	System Noise Analysis . . . . .	69
2.10	Microfabrication Overview and Results . . . . .	73
2.11	Parallel Analysis . . . . .	76
2.12	Conclusions . . . . .	76
<b>3</b>	<b>Force-Detected <math>^{14}\text{N}</math> Overtone NMR</b>	<b>78</b>
3.1	Introduction . . . . .	78
3.2	Theory . . . . .	79
3.2.1	Coordinate Systems . . . . .	79
3.2.2	Quadrupole Physics . . . . .	80
3.2.3	Overtone NMR . . . . .	81
3.3	Signal-to-Noise . . . . .	83
3.4	Simulations . . . . .	84

3.4.1	Electric Field Gradients . . . . .	84
3.4.2	NMR Simulations . . . . .	86
3.5	Conclusions . . . . .	87
<b>A</b>	<b>Torsional BOOMERANG</b>	<b>88</b>
A.1	Introduction . . . . .	88
A.2	Signal-to-Noise . . . . .	89
	<b>Bibliography</b>	<b>93</b>

# List of Figures

1.1	Bloch equation simulation showing magnetization trajectories on a Bloch sphere.	3
1.2	(a) Zeeman energy splitting of nuclear spin states. (b) A basic NMR experimental apparatus. . . . .	7
1.3	(a) The magnitude of the nuclear magnetic moment is shown which is determined by the Zeeman splitting and Boltzmann distribution of spins. (b) Precession of $\mathbf{M}$ about $\mathbf{B}_0$ after application of a resonant $\frac{\pi}{2}$ pulse. . . . .	7
1.4	A time-domain NMR signal is converted to the frequency domain by the operation of a Fourier transform. . . . .	8
1.5	Flexible-sphere model of an idealized mechanical detector. . . . .	11
1.6	Cross-section of a force-detected NMR spectrometer designed to have high magnetic field homogeneity at the sample. . . . .	12
1.7	The force field between a sample moment $\mu_s$ and an axial detector moment $\mu_d$ .	13
1.8	Encoding of NMR into mechanical oscillations. . . . .	14
1.9	Detector magnet dimensions used in signal-to-noise definition. $r_d$ is the detector radius, $h_d$ the height, and $R_{\max}$ the distance from the sample center to the detector. . . . .	16
1.10	Signal-to-noise and scaling simulations for inductive detection and force detection. (a) $^1\text{H}$ NMR of gypsum, $\text{CaSO}_4 \cdot 2\text{H}_2\text{O}$ and (b) $^{29}\text{Si}$ NMR of scapolite. (c) $^{13}\text{C}$ NMR of a single crystal 50 kD protein with a single labeled carbon atom. . . . .	18
2.1	Plots of $k_{\text{mag}}$ versus gap $g$ , saturation magnetization $M_s$ , detector height $h_d$ , and detector radius $r_d$ . The fit from the data in Table 2.1 is shown as a dotted line. . . . .	26

2.2	Signal-to-noise ratio versus the detector radius $r_d$ and height $h_d$ scaled by $R_{\max}$ . The optimal sensitivity is observed for a detector with no added inert mass. . . . .	28
2.3	Signal-to-noise ratio versus the detector radius $r_d$ and height $h_d$ scaled by $R_{\max}$ . In this case, the inert mass equals 2.9 times the detector mass. . . . .	29
2.4	Ternary plot of saturation magnetization $M_s$ as a function of nickel, cobalt, and iron concentrations in electrodeposited magnetic materials. . . . .	30
2.5	SEM images of microfabricated magnetic device structures showing both micromicrofabricated annular and detector magnets with radial slits and the photoresist molds used to create the magnetic structures. . . . .	31
2.6	A cross-section of the truncated conical iron pole piece with top diameter $d_{ct}$ , bottom diameter $d_{cb}$ , pole height $h_c$ , and cone angle $\theta_c$ . . . . .	33
2.7	Plots of absolute value of the magnetic flux through field magnets. (a) Symmetric arrangement NdFeB50 right cylinders capped by saturated iron truncated cones with cone angle $\theta_c = 33^\circ$ . (b) NdFeB50 cylindrical magnets with the same dimensions as (a). . . . .	33
2.8	Calculation of the magnetic field at positions along the symmetry axis for the proposed spectrometer for a detector-annular gap $g$ of $1 \mu\text{m}$ (a) and $g$ of $3 \mu\text{m}$ (b). . . . .	35
2.9	Distribution of magnetic fields with a $50 \mu\text{m}$ diameter spherical sample with $r_d = 26 \mu\text{m}$ and $g = 1 \mu\text{m}$ . These lineshapes are for perfectly centered detector magnets and for detector magnet displacements of $\pm 500 \text{ nm}$ along the magnetization axis. The simulated lineshapes adjusted for sensitivity variations in the sample volume. . . . .	35
2.10	Distribution of magnetic fields with a $50 \mu\text{m}$ diameter spherical sample with $r_d = 26 \mu\text{m}$ and $g = 3 \mu\text{m}$ . These lineshapes are for perfectly centered detector magnets and for detector magnet displacements of $\pm 500 \text{ nm}$ along the magnetization axis. The simulated lineshapes adjusted for sensitivity variations in the sample volume. . . . .	36
2.11	Components of normal stress. . . . .	37
2.12	Calculated von Mises stress for flexural vibration of a resonator without a stress buttress. The units of stress are given in $\text{N}/\text{m}^2$ . . . . .	38

2.13	Calculated von Mises stress for flexural vibration of a resonator with a stress buttress. The units of stress are given in $\text{N}/\text{m}^2$ . . . . .	39
2.14	Model of electromechanical tunable three parallel plate capacitive transducer. . . . .	41
2.15	Three-plate capacitive force transducer allowing both actuation of the resonator and tuning of its mechanical resonance frequency. . . . .	42
2.16	FEM analysis of three-plate capacitive transducer. (a) The force on the center plate as a function of distance separation $d_1$ . (b) The force on the center plate as a function of potential difference. . . . .	42
2.17	Scanning electron microscope image of a microfabricated mechanical oscillator. . . . .	43
2.18	Thermoelastic damping as a function of beam height $b$ and beam length $L$ for a rectangular silicon beam. In the first plot, $L$ was fixed at $400\ \mu\text{m}$ and in the second plot $b$ was fixed at $5.3\ \mu\text{m}$ . . . . .	45
2.19	Azimuthal eddy currents due to relative motion of magnets. . . . .	48
2.20	Experimental measurement of eddy current damping effects for the millimeter scale spectrometer. The oscillator ringdown time $\tau_h$ is plotted as a function of the number of radial slits in the annulus for three detector configurations. . . . .	49
2.21	Spherical magnetic nanoparticle. Symmetry requires that the eddy currents to be azimuthal where $\frac{dB}{dt}$ is along $\hat{\mathbf{z}}$ . . . . .	50
2.22	The basis of adiabatic rapid passage (ARP). In the rotating-frame, the offset frequency $\Delta(t)$ is swept such that the angle $\theta(t) = \tan^{-1}(\Delta(t)/\gamma_n B_1)$ . . . . .	53
2.23	Illustration of driving the mechanical oscillator with efficient ARP. . . . .	53
2.24	Phase cycling for efficient ARP in the rotating frame. . . . .	54
2.25	Radiofrequency excitation coil and silicon coil and sample holder. . . . .	55
2.26	$B_1$ magnetic field homogeneity provided by parallel-plate rf coil. (a) $B_{yz}$ contour map through the sample center. (b) $B_{xy}$ contour map of magnetic field through the sample center. . . . .	56
2.27	$B_1$ magnetic field homogeneity provided by parallel-plate rf coil. (a) $B_{xy}$ contour map of magnetic field $10\ \mu\text{m}$ above the sample center. (b) $B_{xy}$ contour map of magnetic field $20\ \mu\text{m}$ above the sample center. . . . .	56
2.28	SEM image of sample and radiofrequency coil support. Image courtesy of Choonsup Lee. . . . .	57

2.29	Cross-section of silicon microfluidic channel. There are three piezoelectrically controlled microvalves indicated in purple. On the right hand side, the two narrow channels allow samples to leave and reenter or to allow multiple samples to enter allowing study of chemical reactions. . . . .	58
2.30	Simulation of Navier-Stokes equations in a silicon microfluidic channel with piezoelectric microvalves. The contour plots show the velocity field $\mathbf{u}$ in m/s. . . . .	60
2.31	Constant current controller for Sharp LT023 laser diode. . . . .	61
2.32	Schematic diagram indicating pathway, detection, and optical power of laser light in the fiber-optic interferometer. . . . .	62
2.33	Interference waveform of the voltage output of the transimpedance amplifier as a function of $z_0/\lambda$ . . . . .	64
2.34	Optical microscope image of $45^\circ$ cleaved, $125\ \mu\text{m}$ diameter fiber. . . . .	65
2.35	Transverse fiber-optic interferometer. A $45^\circ$ polish at the fiber end causes light to be launched perpendicular to the fiber axis by total internal reflection. . . . .	66
2.36	Angle sensitivity of the TFOI. Only positive angular deviations are shown due to the symmetry of the plot. . . . .	67
2.37	Feedback circuit for locking the interferometer to the sensitive portion of the interference waveform. All voltages shown were provided by dc power sources to minimize electrical noise. . . . .	68
2.38	Signal conditioning path. The selected gain factors are shown for important connections in the signal path. TIA stands for transimpedance amplifier and converts a current to a voltage. The photodiode has a responsivity of $0.58\frac{\text{A}}{\text{W}}$ , the transimpedance is $10^7\Omega$ , and the displacement sensitivity as observed experimentally is $12\frac{\text{nm}}{\text{V}}$ . The transverse fiber-optic interferometer is shown in the inset and the interfering wave is depicted as a dotted line. . . . .	70
2.39	Proposed spectrometer assembly and arrangement. The optical fiber used for interferometry has been omitted for clarity. . . . .	74
2.40	Microfabrication overview. There are five steps in the process that involve photolithography. PR stands for photoresist, BOE for buffered oxide etch, PECVD for plasma enhanced chemical vapor deposition, TO for thermal oxide, and RIE for reactive ion etch. . . . .	75
2.41	Massively parallel analysis with an array of BOOMERANG detectors. . . . .	76

3.1	Spin energy level diagrams for $^{14}\text{N}$ NMR. . . . .	79
3.2	Electrostatic potential surfaces for aminopyridine. . . . .	85
3.3	Electrostatic potential surfaces for leucine-like molecule. . . . .	86
3.4	Electrostatic potential surfaces for histidine. . . . .	86
3.5	Calculated first-order quadrupole (left) and second-order quadrupole (right) spectrum for the leucine-like derivative. The overtone spectrum (right) has a line width over two orders of magnitude smaller than the first-order spectrum.	87
A.1	Cross-sectional view showing a sample's spin magnetization precessing at the Larmor frequency via a dipole-dipole coupled torque to a cylindrical detector magnet suspended about a torsion axis. . . . .	88
A.2	Side views of torque-based detector showing relevant geometric parameters. .	90
A.3	Signal-to-noise contour plot for torque-detected NMR as a function of scaled height and radius. The global maximum is marked by an "x." . . . . .	92

# List of Tables

2.1	Finite element simulations of the effective of $k_{mag}$ on detector radius, height, annular gap, and saturation magnetization. . . . .	25
2.2	Magnetic field and field homogeneity as a function of saturated iron pole cone angle. . . . .	33
2.3	Temperature dependent material properties of silicon. . . . .	36
2.4	Oscillator resonance frequency as a function of beam height. . . . .	39
3.1	Spherical tensor operators. . . . .	82
3.2	Electric field gradient tensor elements, asymmetry parameters, and quadrupolar coupling constant. . . . .	85

# Chapter 1

## Introduction

In a nuclear magnetic resonance (NMR) experiment, the properties and local environment of atomic nuclei are probed by inducing transitions between nuclear spin energy levels whose energy separation is determined by the Zeeman interaction. The magnitude of this splitting is unique to a given nucleus and is determined by the nuclear gyromagnetic ratio. NMR spectroscopy allows assignment of molecular structure by acquiring the energy spectrum of nuclear spins in a molecule, and by interpreting the symmetry and positions of resonance lines in the spectrum. As such, NMR has become one of the most versatile and ubiquitous spectroscopic methods. Despite these tremendous successes, NMR experiments suffer from inherent low sensitivity due to the relatively low energy of photons in the radiofrequency (rf) region of the electromagnetic spectrum.

This thesis describes a general methodology to address these shortcomings with an emphasis on high-resolution spectroscopy in samples with diameters in the micron range and below. In this chapter, we will begin by discussing the basic physics of NMR and then give an extensive description of the new method of detection developed in our laboratory that promises improved sensitivity over inductive detection. In our method, the NMR signal is a magnetic force that is encoded in the motion of a mechanical oscillator. In the following chapters we will present the design issues and progress towards a microfabricated spectrometer, discuss the issues important for NMR at the nanoscale, and illustrate the improvement in force detection of inductive detection in  $^{14}\text{N}$  overtone experiments.

## 1.1 NMR Physics

We aim to provide a heuristic description of the theoretical framework of NMR which will serve as a guide to the simulations and calculations in the following chapters. To this end, both the classical and quantum mechanical treatments of NMR is presented.

### 1.1.1 Classical Mechanical Description

The basic tenet of the classical description of NMR is a magnetic dipole interacting with some external magnetic field. This interaction is easily described by a first order differential equation

$$\frac{d\mathbf{M}}{dt} = -\gamma_n \mathbf{M} \times \mathbf{B}_0 \quad (1.1)$$

which is known as the Bloch equation.[1] The magnetization  $\mathbf{M}$  is typically considered to be a bulk property of the sample and the magnetic moment of an individual spin is given by  $\boldsymbol{\mu} = \gamma_n \mathbf{I}$  where  $\gamma_n$  is the nuclear gyromagnetic ratio and  $\mathbf{I}$  is the spin angular momentum. Equation (1.1) illustrates the torque on the magnetic moment due to the external field  $\mathbf{B}_0$ . We will define the  $z$ -axis to be parallel to  $\mathbf{B}_0$  which gives three equations of motion

$$\frac{d}{dt} \begin{pmatrix} M_x \\ M_y \\ M_z \end{pmatrix} = \begin{pmatrix} -\gamma_n B_z M_y \\ \gamma_n B_z M_x \\ 0 \end{pmatrix}. \quad (1.2)$$

The effects of spin-lattice  $\frac{1}{T_1}$  and spin-spin  $\frac{1}{T_2}$  relaxation may be included by adding appropriate decay terms to equation (1.2) and (1.5).

As a matter of convenience, we will choose to work in the rotating frame, which transforms equation (1.1) to

$$\frac{d\mathbf{M}}{dt} = \mathbf{M} \times \boldsymbol{\Omega}_r + \left[ \frac{d\mathbf{M}}{dt} \right]_r \quad (1.3)$$

where  $\boldsymbol{\Omega}_r$  is the rotational frequency of the rotating frame and  $\left[ \frac{d\mathbf{M}}{dt} \right]_r$  describes evolution of  $\mathbf{M}$  in the rotating frame. For the magnetization to be stationary in the rotating frame we have  $\left[ \frac{d\mathbf{M}}{dt} \right]_r = 0$ . Typically in NMR experiments, we have an offset field such that

$$\frac{d\mathbf{M}}{dt} = -\gamma_n \mathbf{M} \times (\mathbf{B}_z + \Delta\mathbf{B}) \quad (1.4)$$

which gives the following equations of motion

$$\frac{d}{dt} \begin{pmatrix} M_x \\ M_y \\ M_z \end{pmatrix} = \begin{pmatrix} -\gamma_n ((B_z + \Delta B_z) M_y - \Delta B_y M_z) \\ \gamma_n ((B_z + \Delta B_z) M_x - \Delta B_x M_z) \\ -\gamma_n (\Delta B_y M_x - \Delta B_x M_y) \end{pmatrix}. \quad (1.5)$$

In Figure 1.1 below we see numerical solutions to equation (1.5).

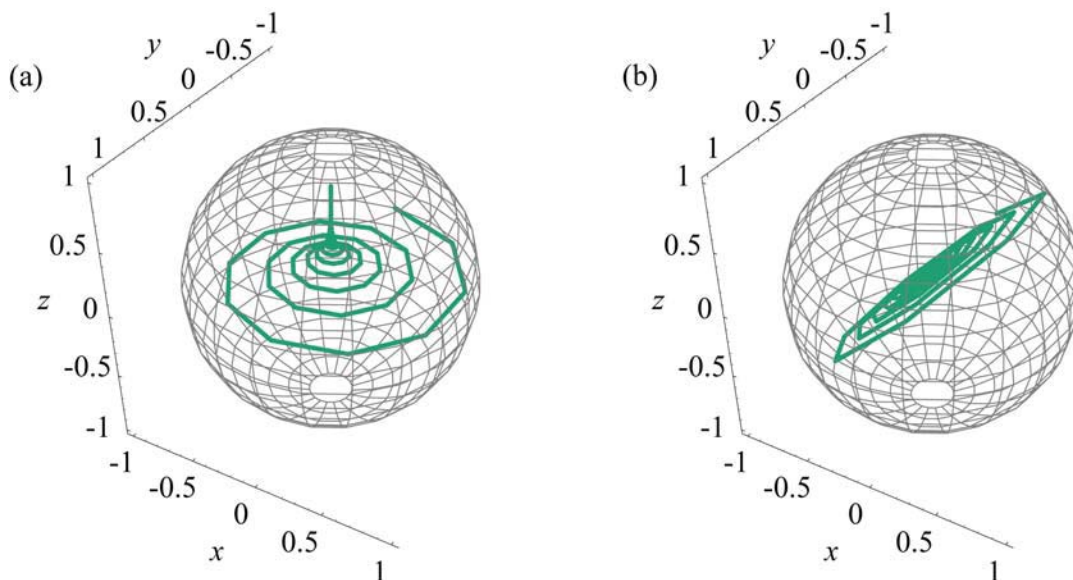


Figure 1.1: Bloch equation simulation showing magnetization trajectories on a Bloch sphere. These simulations include the effects of relaxation. (a)  $T_1 = 10T_2$  with an offset field of 10 Hz, no rf field, and with magnetization initially along the  $y$ -axis. (b) The same conditions as (a) except an rf field strength of 10 Hz.

The effect of rf pulses may also be considered classically, and their field will be noted by  $\mathbf{B}_1$ . Our equation of motion in the non-rotating frame becomes

$$\frac{d\mathbf{M}}{dt} = -\gamma_n \mathbf{M} \times (\mathbf{B}_z + \mathbf{B}_1(t)). \quad (1.6)$$

The desired rotating frame is that in which the oscillating  $\mathbf{B}_1$  term becomes stationary and if we assume that  $B_z \gg \mathbf{B}_1$ , then

$$\left[ \frac{d\mathbf{M}}{dt} \right]_r = -\gamma_n \mathbf{M} \times \mathbf{B}_1^r(t) \quad (1.7)$$

with  $\mathbf{B}_1(t) = \mathbf{R}\mathbf{B}_1^r(t)$  where  $\mathbf{R}$  is a rotation matrix

$$\mathbf{R} = \begin{pmatrix} \cos(\Omega_z t) & \sin(\Omega_z t) & 0 \\ -\sin(\Omega_z t) & \cos(\Omega_z t) & 0 \\ 0 & 0 & 1 \end{pmatrix} \quad (1.8)$$

thus

$$\mathbf{B}_1(t) = \begin{pmatrix} B_{1,x}^r(t) \cos(\Omega_z t) + B_{1,y}^r(t) \sin(\Omega_z t) \\ B_{1,y}^r(t) \cos(\Omega_z t) - B_{1,x}^r(t) \sin(\Omega_z t) \\ B_{1,z}^r(t) \end{pmatrix}. \quad (1.9)$$

Therefore, for the externally applied pulse to remain stationary in the rotating frame, it must be rotating at the same frequency as the rotating frame.

### 1.1.2 Quantum Mechanical Description

If we consider the Hamiltonian  $\mathcal{H}$  of a spin system in which there is evolution of a density operator  $\rho$  instead of magnetization, then this evolution may be described by the Liouville–von Neumann equation

$$\frac{d\rho}{dt} = -i\hbar [\mathcal{H}, \rho]. \quad (1.10)$$

The density operator will be defined as

$$\rho = \sum_{mn} \overline{c_m c_n^*} |\psi_m\rangle \langle \psi_n| \quad (1.11)$$

which is Hermitian and has a unit trace. The density operator allows for simple computation of the expectation values of quantum mechanical operators  $\mathbf{O}$

$$\langle \mathbf{O} \rangle = \text{Tr}[\rho \mathbf{O}] = \text{Tr}[\mathbf{O} \rho] \quad (1.12)$$

and provides an elegant machinery for studying time evolution. This is illustrated by considering a unitary operator  $\mathbf{U}(t, t_0) = \exp\left[-\frac{i}{\hbar} \mathcal{H}(t - t_0)\right]$  where

$$|\psi(t)\rangle = \mathbf{U}(t, t_0) |\psi(t_0)\rangle \quad (1.13)$$

leading to a variant of the Liouville-von Neumann equation

$$\rho(t) = \mathbf{U}(t, t_0) \rho(0) \mathbf{U}^\dagger(t, t_0). \quad (1.14)$$

Analogous to the classical case, a rotating-frame form of the density operator may be constructed. The effect of rf pulses on the density operator may be evaluated using the rotations discussed below.

The mathematics of NMR may be treated in the context of rotations on quantum mechanical operators. Two methods that have been used are Cartesian and spherical tensor based rotations. In Cartesian based rotations, all three dimensional rotations can be reduced to three angles  $\Omega = (\phi, \theta, \gamma)$ . The angle  $\phi$  rotates the  $xy$ -plane around the  $z$ -axis into transformed axes  $x'$  and  $y'$ ,  $\theta$  transforms the original  $y$ -axis to the  $z$ -axis creating three new rotated bases  $x''$ ,  $y''$ , and  $z'$ , finally  $\gamma$  rotates  $x''$  and  $y''$  about the  $z'$ -axis into the final rotated state  $(x''', y''', z')$ . This rotation is typically represented by a  $3 \times 3$  matrix

$$\mathbf{R}(\Omega) = \begin{pmatrix} \cos \gamma \cos \phi - \cos \theta \sin \gamma \sin \phi & \cos \gamma \sin \phi - \cos \theta \sin \gamma \cos \phi & \sin \gamma \sin \theta \\ -\sin \gamma \cos \phi - \cos \theta \cos \gamma \sin \phi & -\sin \gamma \sin \phi - \cos \theta \cos \gamma \cos \phi & \cos \gamma \sin \theta \\ \sin \theta \sin \phi & -\cos \phi \sin \theta & \cos \theta \end{pmatrix} \quad (1.15)$$

which can be considered as three rotations:  $\mathbf{R}(\Omega) = R_x(\phi) R_y(\theta) R_z(\gamma)$ .

The study of symmetry and invariants of angular momentum in quantum mechanics lead to the development of the spherical tensor rotation representation. The Wigner matrix elements are common forms for rotation of angular momentum and provide a convenient means to use spherical tensors. For a total angular momentum  $L$ , there are  $(2L + 1)^2$  elements to rotate each of the  $2L + 1$  eigenvectors. The matrix elements will be denoted by  $D_{m,m'}^l$ , where  $l$  is the rank of the matrix and the  $m, m'$  correspond to a particular matrix element. This may be expressed in terms of the reduced Wigner element

$$e^{i(m\gamma + m'\phi)} d_{m,m'}^l(\theta). \quad (1.16)$$

These rotations may also be generated from individual rotations

$$\mathbf{R}(\Omega) = R_z(\gamma) R_y(\theta) R_x(\phi) = e^{iI_x\phi} e^{iI_y\theta} e^{iI_z\gamma}. \quad (1.17)$$

The Hamiltonian is readily expressed in a spherical tensor basis and because it is invariant under rotation we may write

$$\mathcal{H} = \sum_l \alpha_l \mathcal{T}_l \quad (1.18)$$

where  $\alpha_l$  is a complex constant and  $\mathcal{T}_l$  is a spherical tensor basis element with  $\mathcal{T}_l = A_l \otimes T_l$  where  $\otimes$  is a tensor product,  $A_l$  is a spatial tensor and  $T_l$  is a spin tensor.  $\mathcal{T}_l$  may be expressed explicitly as

$$\mathcal{T}_l = \sum_{m=-l}^l (-1)^m A_{l,m} T_{l,-m} = \sum_{m=-l}^l (-1)^m A_{l,-m} T_{l,m}. \quad (1.19)$$

## 1.2 NMR Spectroscopy

In Figure 1.2(a), we illustrate the Zeeman interaction, which is linear in the applied magnetic field  $\mathbf{B}_0$ . The observed energy level splitting also reflects the local environment of the nucleus being probed by the NMR experiment, because it is dependent upon the response due to interactions with electrons and the magnetic coupling of the nucleus to nearby spins. Figure 1.2(b) depicts a typical apparatus used in NMR experiments. A large, homogeneous field  $\mathbf{B}_0$  at the sample is provided by an electromagnet or superconducting magnet. The sample resides in a coil of conducting wire which provides the rf irradiation used to induce NMR transitions. An ac voltage is applied across the coil circuit at a frequency  $\omega$  which provides a linearly-polarized time-dependent magnetic field with amplitude  $2B_1$  orthogonal to  $\mathbf{B}_0$ . Resonance is achieved when the irradiation frequency equals the nuclear Larmor frequency

$$\omega_0 = \Delta E/\hbar = -\gamma_n B_0, \quad (1.20)$$

where  $\hbar$  is Planck's constant divided by  $2\pi$  and  $\gamma_n$  is the nuclear gyromagnetic ratio. The homogeneity of  $\mathbf{B}_0$  ensures that the transitions observed are due to the local environment of the nucleus as opposed to variations of the Zeeman interaction across the sample.

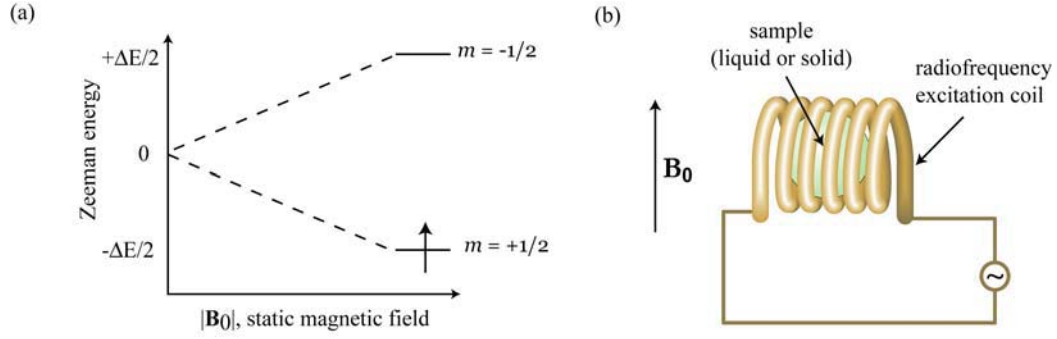


Figure 1.2: (a) Zeeman energy splitting of nuclear spin states, which are labeled according to the allowed values of  $m$ , the projection of the dimensionless nuclear spin angular momentum  $\mathbf{I}$  along  $\mathbf{B}_0$ , for the case where  $I = |\mathbf{I}| = \frac{1}{2}$ . (b) A basic NMR experimental apparatus. The static magnetic field  $\mathbf{B}_0$ , may be provided by superconducting magnets, electromagnets, or permanent magnets.

The advent of Fourier transform methods has allowed modern NMR experiments to be done in the time-domain where pulses of broadband irradiation excite transitions that yield subsequent time evolution of the nuclear magnetic moment  $\mathbf{M}$

$$\mathbf{M} = N\gamma_n\hbar\langle\mathbf{I}\rangle, \quad (1.21)$$

where  $N$  is the number of spins in the ensemble and  $\mathbf{I}$  is the dimensionless nuclear spin angular momentum operator. A short resonant rf pulse tips  $\mathbf{M}$  away from  $\mathbf{B}_0$  and if the pulse duration  $t_p$  is such that  $-\gamma_n B_1 t_p = \frac{\pi}{2}$ , then the tip angle is  $90^\circ$  and the magnetization is placed in the transverse plane. This is shown in Figure 1.3.

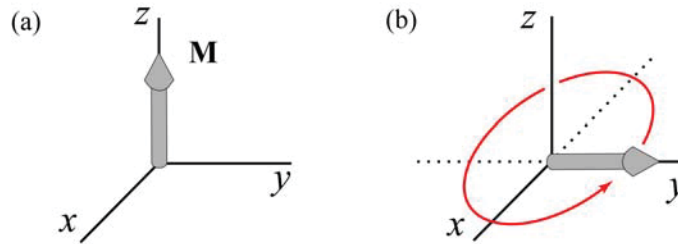


Figure 1.3: (a) The magnitude of the nuclear magnetic moment is shown which is determined by the Zeeman splitting and Boltzmann distribution of spins. (b) Precession of  $\mathbf{M}$  about  $\mathbf{B}_0$  after application of a resonant  $\frac{\pi}{2}$  pulse.

As the magnetization evolves in the transverse plane, a voltage is induced in the rf coil

via Faraday's law of induction and is proportional to  $\frac{d}{dt}\mathbf{M}$ . The signal voltage is given by

$$S(t) = A \cos(\omega_0 t) e^{-t/T_2}, \quad (1.22)$$

where  $A$  is a scaling factor proportional to  $\mathbf{M}$  and  $T_2$  is the transverse nuclear relaxation time due to spin-spin coupling.  $S(t)$  is typically expressed as a free-induction decay, and by Fourier transforming this time-domain signal, the frequency-domain spectrum is obtained as a single Lorentzian peak with full width at half maximum (FWHM) of  $(\pi T_2)^{-1}$  as shown in Figure 1.4. Fourier transform methods have also allowed sophisticated pulse sequences to be designed to selectively edit the spin Hamiltonian to provide specific chemical or spatial information. Despite these advantages, inductively detected NMR suffers from poor sensitivity. The low fractional polarization,  $\sim 10^{-6}$ , and weak magnetic moments per spin result in the need for samples that have  $\sim 10^{18}$  nuclear spins for adequate sensitivity. We will now discuss an alternative strategy which promises to improve the sensitivity tremendously for micron and nanometer scale samples.

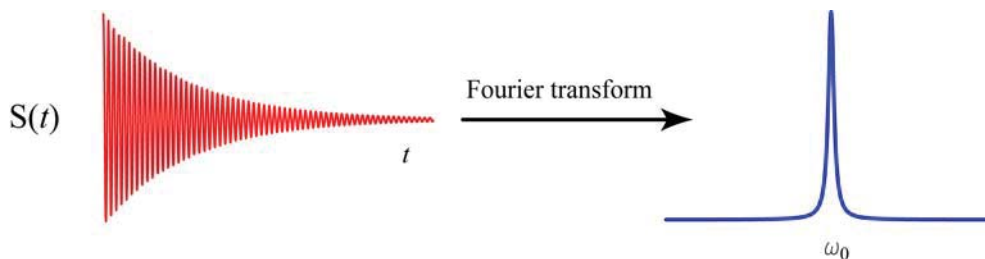


Figure 1.4: A time-domain NMR signal is converted to the frequency domain by the operation of a Fourier transform.

## 1.3 Force-Detected NMR

### 1.3.1 Introduction

The first observation of magnetic resonance was actually a force-detected experiment. In his classical molecular beam experiment, Rabi [2] utilized the Stern-Gerlach effect to spatially separate eigenstates by the projection of their spin angular momentum. The intensity of the molecular beam was modulated by application of an rf field and, on resonance, spin flips were induced. This was accomplished by having the spins pass through an inhomogeneous

magnetic field such that a force  $\mathbf{F}$  existed on the spins due to a gradient  $\mathbf{G}$

$$\mathbf{F} = \boldsymbol{\mu} \cdot \mathbf{G} \quad (1.23)$$

where  $\mathbf{G} = \frac{\partial \mathbf{B}}{\partial \mathbf{r}}$  where  $\mathbf{r}$  is a spatial coordinate. This methodology was later used by Bloom and coworkers [3, 4] to deflect the molecules by the interaction with the transverse components of spin angular momentum. The poor spectroscopic resolution and sensitivity of these methods was improved upon by Pizarro and Weitekamp [5] by confining the spins for longer periods of time where their motion was harmonically driven. In this case, the trajectory of electromagnetically trapped ions was altered by resonance induced changes via electromagnetically switched field gradients.

The first experiment which utilized encoding of force-detection in mechanical oscillations was done by Gozzini in the 1960's.[6, 7] These continuous wave (CW) experiments were done in a homogenous magnetic field. A free radical sample was bound to a torsional resonator and an rf field was applied at the resonance frequency of the spins. The absorption of the rf photons, followed by rapid thermalization through the resonator produced a torque on the resonator which was then related to a magnetic resonance signal. While these experiments proved to be an interesting example of mechanically detected magnetic resonance, the thermalization of angular momentum with the lattice is a weak effect and is not of practical interests, especially for nuclear spins.

In the early 1990's, it was realized that detection of magnetic forces scales more favorably than inductive detection at small size scales.[8, 9] This observation lead to the development of the magnetic resonance force microscope (MRFM).[10, 11, 12] In these experiments a cantilever with a harmonically bound ferromagnet is driven by cyclically inverting the spin magnetization in a nearby sample at the mechanical resonance frequency of the oscillator. The geometry of the MRFM results in large field gradients at the sample and in accordance with equation (1.23) improves the sensitivity of these experiments. Recently, gradients as large as  $5 \times 10^5$  T/m have been produced allowing the observation of magnetic resonance of a single electron spin.[13] The sub-attoNewton per root hertz sensitivity of state-of-the-art MRFM should allow imaging of  $10^2$  nuclear spins, if appropriate means are taken to reduce the quantum mechanical effects of spin noise.[14]

Despite the advantages provided by MRFM, coherent spectroscopic measurements on

anything but a “sensitive slice” of the samples is not possible. The sensitive slice thickness is of order  $B_1/G_{zz}$  where  $G_{zz} = \partial B_z/\partial z$  is the field gradient of the sensor magnet. Practical limitations set  $B_1$  at  $\sim 100$  kHz and the distribution of Larmor frequencies in the sample can vary as much as 30 MHz and only those spins within the bandwidth of the applied rf field will be inverted and detected. Furthermore, the range of fields even with the sensitive slice in MRFM experiments limits sophisticated NMR experiments that require multiple rf pulses, rendering MRFM incompatible with nearly all coherent spectroscopy.

The restrictions of reduced spectroscopic resolution, sensitivity, and coherent control may be mitigated by placing the sample in a nominally homogeneous field. We have dubbed this detection method BOOMERANG: better detection of magnetization, enhanced resolution, and no gradient. Our laboratory [15, 16] has been successful in demonstrating this phenomenon and has shown that by judicious application of multiple-pulse sequences, spectral resolution adequate for chemical purposes is possible. In the remainder of this section, we will discuss the theory behind the experiment, give a detailed signal-to-noise analysis, and present scaling arguments that show the regime in which force detection becomes superior to inductive detection.

### 1.3.2 Homogeneous Fields

An idealized detector would include no field gradients at the sample. We can imagine a flexible spherically symmetric array of detector magnets surrounding a sample. The sample will exert forces on the detector causing elliptical distortions which are induced by cyclically inverting the sample magnetization at the mechanical resonance frequency of the detector. Because the field will remain homogeneous during the “breathing sphere” modes, this allows resolution of chemical shifts and spin-spin couplings, eliminates gradient-based dephasing, and permits coherent control of all the spins in the sample. This idealized detector is shown in Figure 1.5.

However, we require a means of easily detecting the mechanical oscillator excitation. A natural choice that maintains nominally homogeneous fields at the sample is shown in Figure 1.6. In this case, cyclically driving the spins in a sample excites a flexural mode in the mechanical oscillator causing an axial displacement along the symmetry and magnetization axis. The detector is surrounded by an annulus where the gap is chosen to be small

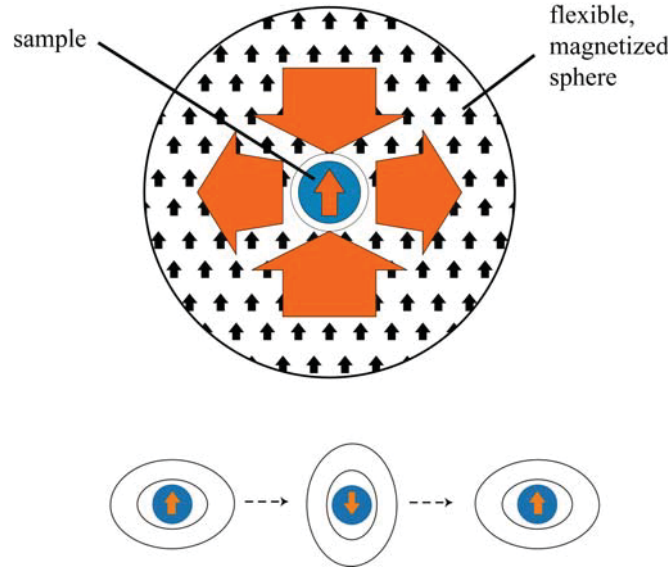


Figure 1.5: Flexible-sphere model of an idealized mechanical detector. The sample is immersed in a hollowed sphere of flexible magnetic material magnetized along the axis of the vertical arrows. Cyclically inverting the sample magnetization at a mechanical resonance frequency of the detector causes elliptical distortions proportional to the magnetization. The field throughout the sample remains homogeneous during the distortions.

enough to allow free movement of the detector while minimizing resulting inhomogeneities. In the equilibrium configuration, the annulus and sensor are coplanar. The flexible silicon membrane is shown in a clamped-clamped arrangement with the sensor harmonically bound to the center.

### 1.3.3 Theory

The force between a spin-bearing sample and a nearby ferromagnetic detector is given by the gradient of the potential energy of interaction with respect to the relative coordinate of the system,  $\mathbf{F} = -\partial E/\partial \mathbf{r} = -\nabla E$ . The coordinate  $\mathbf{r}$  is chosen to be a harmonic oscillator coordinate that corresponds to the detector mode. If we assume that the sample is spherical and uniformly polarized, then the magnetic field can be represented as a point dipole allowing the interaction force to be expressed as

$$\mathbf{F} = -\nabla_d(-\mathbf{B}_s \cdot \boldsymbol{\mu}_d) = +\nabla_d \left( \frac{\mu_0}{4\pi} \boldsymbol{\mu}_s \cdot \left( \frac{3\hat{\mathbf{r}}\hat{\mathbf{r}} - 1}{r^3} \right) \right) \cdot \boldsymbol{\mu}_d, \quad (1.24)$$

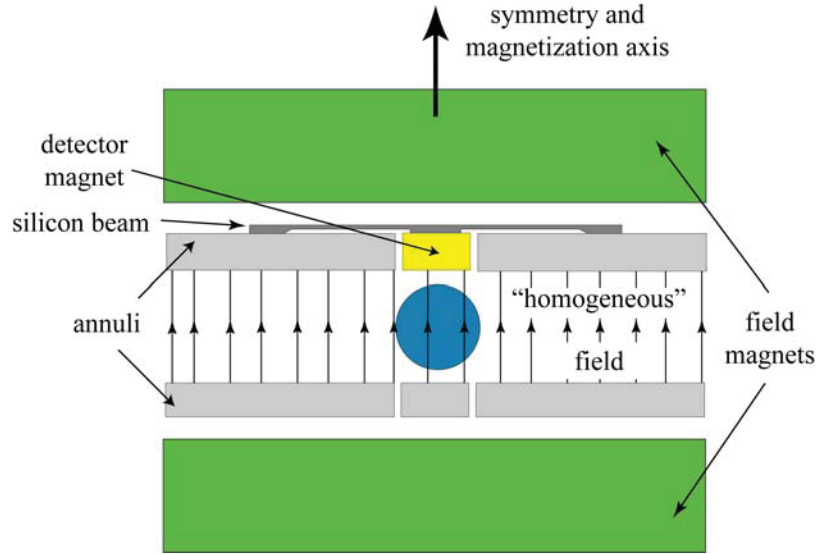


Figure 1.6: Cross-section of a force-detected NMR spectrometer. The dimensions of the magnet are chosen to maximize the field homogeneity at the sample and odd-order field gradients are eliminated by maintaining reflection symmetry. The detector magnet is bound to the center of the silicon beam.

where  $\hat{\mathbf{r}}$  is the unit vector pointing from the position of the sample dipole moment  $\boldsymbol{\mu}_s$  to that of the detector  $\boldsymbol{\mu}_d$ ,  $\nabla_d$  is the gradient with respect to the coordinates of  $\boldsymbol{\mu}_d$ , and  $\mathbf{B}_s$  is the sample's magnetic field. In our experimental configuration, we have cylindrical symmetry and if we replace the dipole by  $\mathbf{M}_n(\mathbf{r}_n) dV_n$  ( $n = s, d$ ) and integrate over the volume of both bodies we find that

$$\mathbf{F} = \frac{\mu_0 V_s M_s M_d}{4\pi r^4} [\cos \theta (9 - 15 \cos^2 \theta) \hat{\mathbf{z}} + (3 - 15 \cos^3 \theta) \hat{\boldsymbol{\rho}}]. \quad (1.25)$$

In equation (1.25) we have assumed that both the magnetization of the sample  $M_s$  and detector  $M_d$  are constant vectors along the symmetry axis of the cylinder,  $\hat{\mathbf{z}}$ . This interaction force is shown in Figure 1.7.

The steady-state displacement of the mechanical oscillator is given by

$$z = \frac{F(\omega_h) Q_h}{m\omega_h^2} = \frac{F(\omega_h) Q_h}{k_{eff}} \quad (1.26)$$

where  $Q_h$  is the quality factor of the oscillator,  $m$  its motional mass,  $\omega_h$  is its resonance frequency, and  $k_{eff}$  is its effective spring constant. We observe that the enhancement of resonant driving is of factor  $Q_h$ . A more useful parameter to characterize an oscillator is

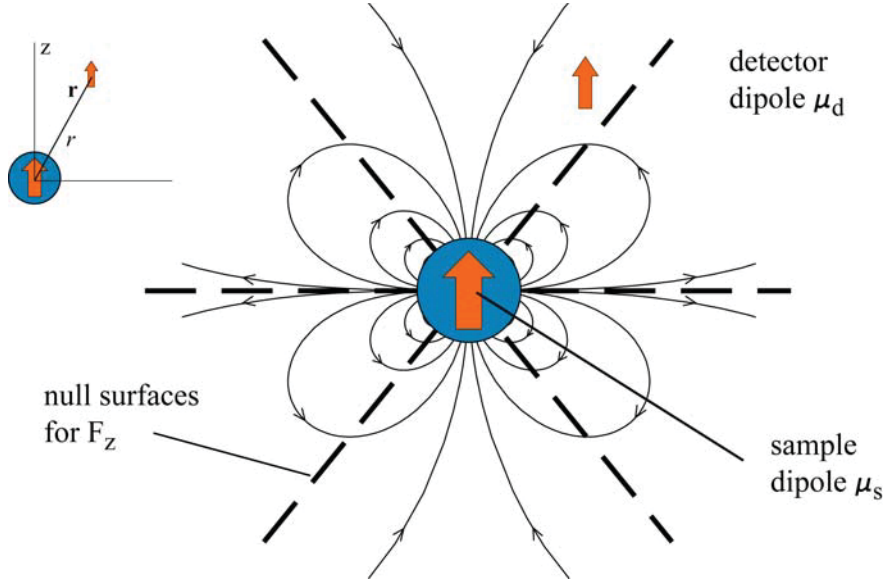


Figure 1.7: The force field between a sample moment  $\mu_s$  and an axial detector moment  $\mu_d$ . The dotted lines indicate nodal surfaces of revolution at angles of  $90^\circ$  and  $\theta = \arccos \sqrt{3/5} \approx 39.2^\circ$  upon which the  $z$ -component of the force vanishes. An idealized detector is confined to lie within this nodal surface.

its ringdown time,  $\tau_h = \frac{2Q_h}{\omega_h}$ . The ringdown time is the time required for the amplitude of the oscillator's excitation to decay to  $\frac{1}{e}$  of initial value.

### 1.3.4 Encoding NMR into Mechanical Oscillations

Most NMR experiments in the time-domain detect Larmor precession in the transverse plane. As illustrated in Figure 1.6, the silicon mechanical oscillator is excited along the symmetry axis which means that we are detecting longitudinal magnetization. Therefore, it is necessary to reconfigure the detection scheme to measure the sample's longitudinal magnetization  $M_z$ . The detection scheme is shown below in Figure 1.8.

During the encoding period, the sample magnetization is tipped into the transverse plane by application of a  $\frac{\pi}{2}$  pulse. The spins evolve during a period  $t_1$  either freely or under the influence of an NMR pulse sequence. Following evolution, the spins are flipped back to the  $z$ -axis by a second  $\frac{\pi}{2}$  pulse and then the spin magnetization is cyclically inverted at the mechanical oscillator's resonance frequency driving a picometer scale motion of the oscillator during the time period  $t_2$ . The Fourier transform of this signal gives a spectrum whose area is proportional to the sample magnetization at the onset of the detection period. Weighting

this Fourier transform gives a single point in a “free-induction decay”, and modulation of the spins during successive periods in  $t_1$  allows pointwise acquisition of the time-domain NMR signal. Application of a second Fourier transform gives the spectrum of transition energies.

The spins are cyclically inverted twice per mechanical oscillator period using a novel phase-cycled, tangent-frequency-modulated adiabatic rapid passage sequence (for more detail see Chapter 2.6). Spurious driving of the oscillator that would be observed in other methods such as sinusoidal or continuous sweeps, is diminished by inverting at twice the oscillator resonance frequency and by sweeping from the same side on each inversion.

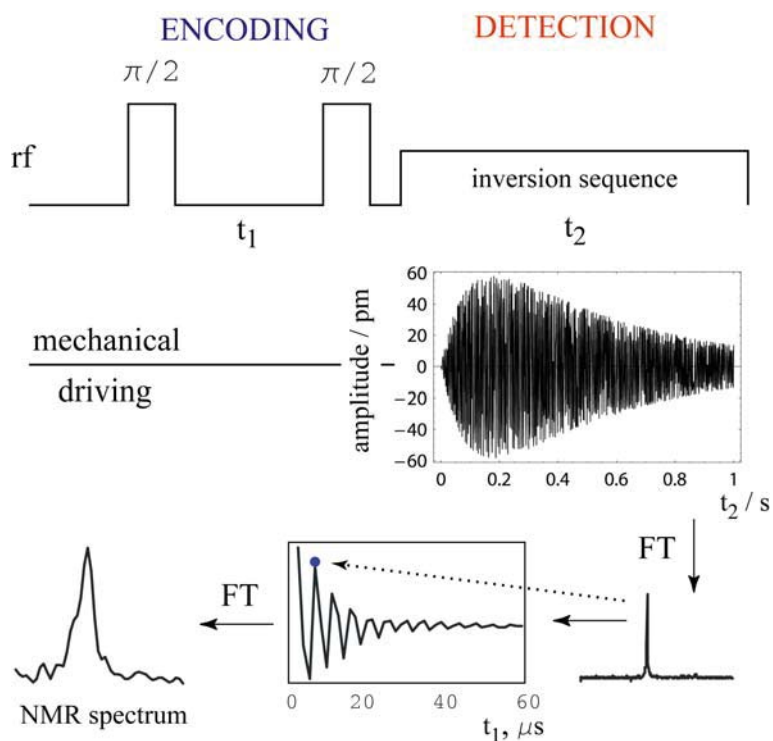


Figure 1.8: Encoding of NMR into mechanical oscillations.

### 1.3.5 Signal-to-Noise Analysis

The signal-to-noise ratio of the BOOMERANG NMR experiment is given by

$$SNR_F = \frac{F_{z,rms}}{F_N} \quad (1.27)$$

with the root-mean square (rms) signal force  $F_{z,rms} = \frac{4}{\pi\sqrt{2}}F_z$  where the factor of  $\frac{4}{\pi}$  comes from the Fourier component of the spin inversion sequence. The predominant source of noise is the time-averaged noise force  $F_N$ , which is due to the Brownian motion of the mechanical oscillator assembly. For a given temperature  $T$ , the noise force is given by

$$F_N = \sqrt{4k_B T \alpha \Delta\nu} \quad (1.28)$$

where  $\alpha$  is a damping parameter and is equal to  $\frac{2m}{\tau_h}$  and  $\Delta\nu = \frac{1}{4T_{1a}}$  is the measurement bandwidth. Here we use McCombie's [17, 18] definition of bandwidth for a process with transfer function  $Z(\nu)$  as

$$\Delta\nu = \int_0^\infty |Z(\nu)|^2 d\nu / |Z(\nu_{\max})|^2. \quad (1.29a)$$

$T_{1a}$  is the spin-lattice relaxation time during adiabatic rapid passage, our spin inversion scheme. The signal amplitude is obtained by integrating equation (1.25) over the detector volume. Doing so gives

$$F_z = \kappa_F \mu_0 V_s M_s M_d / R_{\max}. \quad (1.30)$$

where  $\kappa_F$  is a dimensionless shape factor,  $\mu_0$  is the magnetic permeability of free space, and  $V_s$  is the sample volume.  $\kappa_F$  is given by

$$\kappa_F = \frac{R_{\max}}{4\pi} \int \frac{1}{r^4} (9 \cos \theta - 15 \cos^3 \theta) dV_d, \quad (1.31)$$

and in the case of a cylindrical detector of radius  $r_d$  and height  $h_d$  placed a distance  $R_{\max}$  from the center of the sample, the shape factor takes the simplified form

$$\kappa_F = \frac{r_d^2 R_{\max}}{2} \left( \frac{1}{[(R_{\max} + h_d)^2 + r_d^2]^{3/2}} - \frac{1}{[R_{\max}^2 + r_d^2]^{3/2}} \right). \quad (1.32)$$

The SNR for force detection is then

$$SNR_F = \frac{\kappa_F \mu_0 V_s M_s M_d / R_{\max}}{\sqrt{8k_B T \alpha \Delta\nu}}. \quad (1.33)$$

The signal-to-noise ratio for inductive detection has been considered in detail.[19] It may

be expressed as  $SNR_I = V_{rms}/V_N$ , where  $V_{rms}$  is the rms electromotance of the detection coil and  $V_N$  is the Johnson noise dominated time-averaged voltage noise

$$V_N = \sqrt{4k_B T R \Delta\nu} \quad (1.34)$$

where  $R$  is the total resistance in the coil at the nuclear Larmor frequency, which includes both skin and proximity effects. The skin depth is defined to be

$$\delta = \left( \frac{2}{\omega \sigma \mu} \right)^{1/2} \quad (1.35)$$

where  $\sigma$  is the electrical conductivity and  $\mu$  the permeability. Here we take the detection bandwidth to be  $\Delta\nu = \frac{1}{4T_{1\rho}}$  where  $T_{1\rho}$  is the rotating-frame relaxation time, which may be maximized using spin-locking methods.

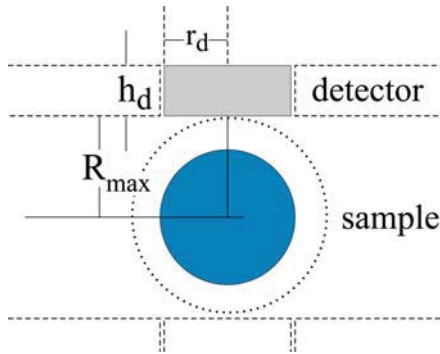


Figure 1.9: Detector magnet dimensions used in signal-to-noise definition.  $r_d$  is the detector radius,  $h_d$  the height, and  $R_{\max}$  the distance from the sample center to the detector.

The most common geometry of detection coils is a solenoid. For an  $n$ -turn coil of length  $2g$  and radius  $r_c$ , we have a similar phenomenological shape factor

$$\kappa_I = \frac{nR_{\max}}{\sqrt{g^2 + r_c^2}} \quad (1.36)$$

where  $R_{\max}$  is defined here as the distance from the sample center to the inner edge of the coil. The amplitude  $V$  of the oscillating electromotance is given by

$$V = \frac{\kappa_I \mu_0 V_s M_s \omega}{R_{\max}} \quad (1.37)$$

and thus the SNR is

$$SNR_I = \frac{\kappa_I \mu_0 V_s M_s \omega}{\sqrt{8k_B T R \Delta\nu}}. \quad (1.38)$$

### 1.3.6 Scaling Arguments

For the case of force-detection, we see that by equation (1.33), the only size dependent parameters are the  $V_s$  and  $R_{\max}$ . The signal force thus scales as  $r^2$  where  $r$  is a linear dimension of the sample and detector. It was shown in the Ph.D. thesis of Garrett Leskowitz [18] that the noise force scales as  $r^{3/2}$  assuming scale invariance of the damping parameter  $\tau_h$ . Thus the signal-to-noise for force detection scales as  $r^{1/2}$ . Similarly for inductive detection, the signal scales as  $r^2$ , and there exist two regimes in which the scaling dependence of the noise is considered. When the wire diameter is larger than the skin depth  $\delta$ , the resistance  $R = \rho \frac{L}{A}$  is scale invariant ( $\rho$  is the coil's resistivity,  $L$  is the length of the unwound conductor, and  $A$  is the coil's cross-sectional area). In this case,  $SNR_I$  scales as  $r^2$ . When wire diameter is less than the skin depth, current flows through the wire more uniformly and the noise term scales as  $r$ . Therefore,  $SNR_I$  will scale as  $r^{5/2}$ . These observations on scaling in inductive detection have been experimentally confirmed in microcoil NMR by several groups.[20, 21]

These scaling arguments suggest that  $SNR_F$  decreases significantly more slowly with size than  $SNR_I$  and that depending on the nuclear gyromagnetic ratio  $\gamma_n$  and static magnetic field strength  $B_0$ , there is a well-defined “break-even” point, typically for samples with diameters between 80-300  $\mu\text{m}$  diameter. We have chosen to fabricate a spectrometer that is optimized for 50  $\mu\text{m}$  sample sizes, which places  $R_{\max}$  at 34  $\mu\text{m}$ . Relevant samples for both terrestrial and biological applications are shown below in Figure 1.10. These signal-to-noise simulations assume idealized detectors. For force detection this is a detector whose mass is equal to that of the moving magnet and for inductive detection the parameters for an ideal solenoid,  $\frac{l_{\text{coil}}}{d_{\text{coil}}} = 0.7$ , were taken from Hoult and Lauterbur.[19]

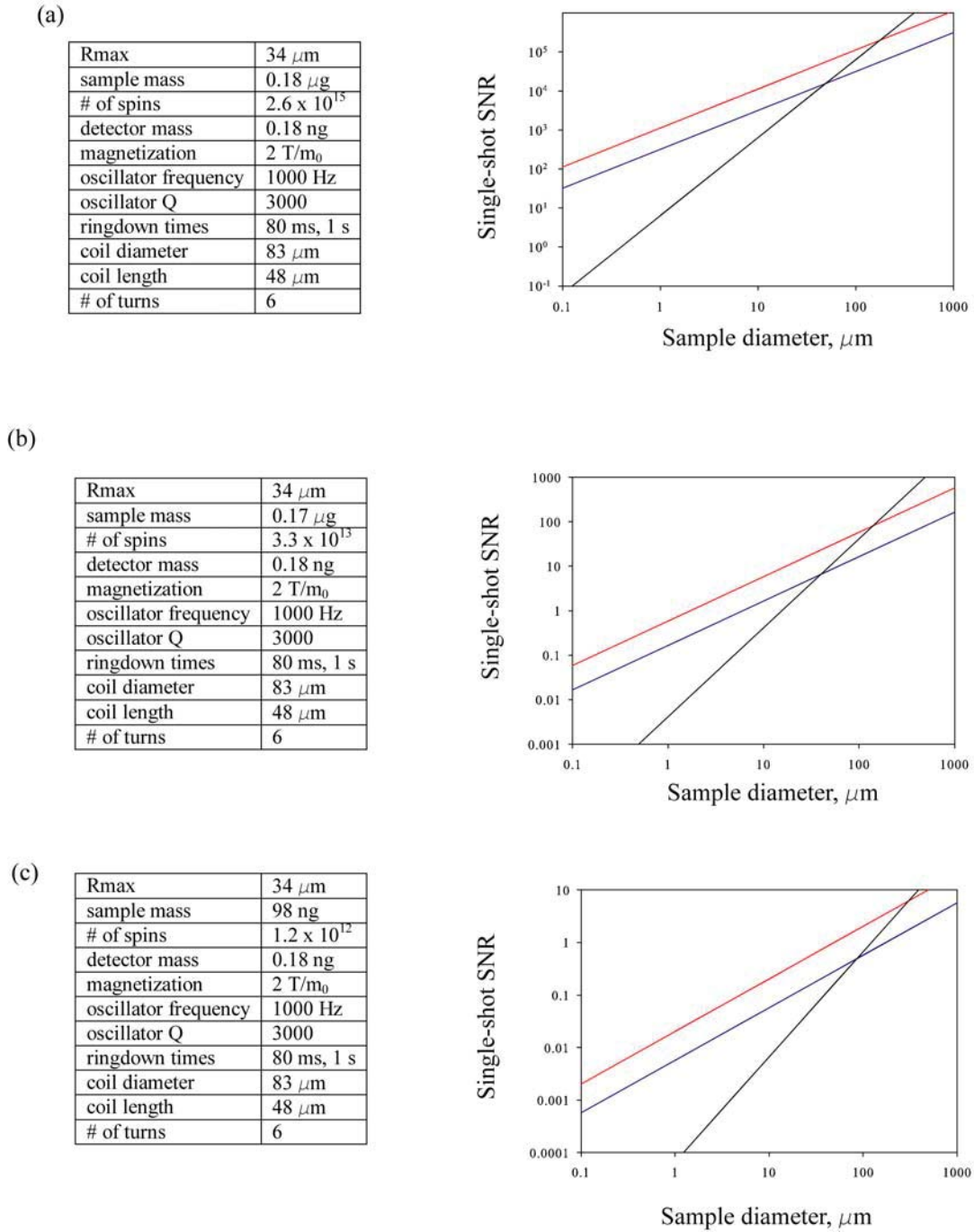


Figure 1.10: Signal-to-noise and scaling simulations for inductive detection (black curves) and force detection (red and blue curves). The red and blue curves correspond to  $\tau_h$  of 1 s and 80 ms respectively. In all cases a fully optimized detector, a one second relaxation time, and a  $B_0 = 2$  T are considered and the tabulated parameters are for a  $50 \mu\text{m}$  diameter sample. (a)  $^1\text{H}$  NMR of gypsum,  $\text{CaSO}_4 \cdot 2\text{H}_2\text{O}$  and (b)  $^{29}\text{Si}$  NMR of scapolite. Both are suspected to be in Martian soil. (c)  $^{13}\text{C}$  NMR of a single crystal 50 kD protein with a polarization enhanced carbon atom.

## 1.4 Thesis Outline

In Chapter 2, we give an extensive discussion of the design issues relevant for fabrication of a MEMS-based force-detected NMR spectrometer. This includes the design of magnet geometries, mechanical oscillator design, considerations of sources of damping, development of a method for capacitive transduction of positioning of the detector magnet as well as tuning of the mechanical oscillator resonance frequency, a detailed discussion of the method of spin inversion developed in our laboratory, the design parameters for a novel type of silicon-based microfluidic channel which uses piezoelectrically driven microvalves, the development of a new method of fiber optic interferometry, and an outline of the microfabrication procedure and initial microfabrication results.

We consider the case of force-detected NMR of nanoscale samples in Chapter 3. Devices of this size scale whose resonance frequency is in the audiofrequency range will be considerably difficult to fabricate and even if they could be fabricated, their thermal motion will exceed the device dimensions. As a result, it will be necessary to detect transverse magnetization. A derivation of the signal-to-noise ratio for detection of transverse magnetization with torsional oscillators is presented as well as a preliminary design for these oscillators. A method for detection of the angular displacements is suggested. We conclude Chapter 3 by discussing quantum statistical spin noise that will dominate for nanoscopic samples.

Chapter 4 is concerned with exploring the utility of overtone NMR, a variant of multiple quantum NMR, for studying  $^{14}\text{N}$ . This work was motivated by preliminary signal-to-noise calculations done by Bruce Lambert [22] that suggest our method of force detection will be favorable over conventionally detected spectroscopy. We include simulations on several molecule of astrobiological importance, tholins.

## Chapter 2

# Design of MEMS-Based Force-Detected Spectrometer

This chapter concerns the design issues of a microelectromechanical system (MEMS) based force-detected NMR spectrometer. The design is motivated by the signal-to-noise calculations presented in Chapter 1 and will be based upon practicality, robustness, high field homogeneity, and optimal sensitivity for samples with  $50\ \mu\text{m}$  diameters. As a means of directing the steps towards microfabrication, we wish to consider structures with: 1) narrow, unobstructed detector/annular magnet gaps to maintain high field homogeneity, 2) low stress electroplated magnetic films, 3) mechanical oscillator structures with low dissipation and inertial mass, 4) fine control over observed resonance frequencies, 5) a means of mitigating damping due to eddy currents, and 6) low power and portability to allow both terrestrial and laboratory spectroscopic studies.

We will begin by discussing general design issues that reflect both our needs to have a device for detailed spectroscopic studies and limitations in standard microfabrication methods. In cases where analytical solutions were not possible, we have made use of finite element methods and a short description of this methodology is presented. The design of the silicon oscillator and magnetic assembly is then presented, followed by a detailed analysis of sources of damping during experiments. Several schemes for radiofrequency excitation of the spins are presented along with a description of our method for spin inversion, tangent-phased adiabatic rapid passage. Methods to shuttle liquid samples in and out of the spectrometer are proposed. A novel means of detecting sub-picometer motion will be shown that offers advantageous over other methods, especially in geometrically confined structures. We conclude by discussing sources of instrumental noise.

## 2.1 General Design Issues

The mechanical oscillator should be designed such that the inertial mass is small compared to that of the detector magnet, with low mechanical dissipation, high torsional rigidity to counteract the torsional stress placed on the detector magnet in the annulus. Of particular importance is the balancing of the resonator's elastic  $k_{elas}$  and magnetic  $k_{mag}$  spring constants.  $k_{elas}$  is due to the restoring force of the beam, and  $k_{mag}$  is due to magnetic forces between the detector and annulus. The magnetic spring constant is negative and will soften the effective spring constant  $k_{eff} = k_{elas} + k_{mag}$ . Therefore,  $k_{eff}$  will depend upon the magnetic field strength, the relative sizes of the magnets, and the gap between the detector and annulus.

We also seek a device with a resonance frequency in a  $\sim 2$  T magnetic field of 1-10 kHz in order to efficiently invert the spin magnetization with adiabatic rapid passage. The  $\sim 2$  T field is chosen based upon the use of soft and low stress magnetic materials that can be readily fabricated into a device with saturation magnetization between  $1.6-2$  T/ $\mu_0$  and the restriction of the use of hard permanent magnets to provide the static field. This restriction is based upon the goal of a portable, low-power spectrometer, where we have restricted the total power to be less than  $100 \mu\text{W}$  and the majority of this power will be utilized by the radiofrequency excitation circuit.

Mechanisms to eliminate sources of damping, whenever possible, will also be executed. As we will see, the primary contribution to damping is through azimuthal eddy currents that are generated by the moving detector magnet. Recalling the signal-to-noise expression from Chapter 1, the total damping  $\alpha$  is related to the oscillator ringdown time  $\tau_h$

$$SNR_F = \frac{\kappa_F \mu_0 V_s M_s M_d / R_{\max}}{\sqrt{8k_B T \alpha \Delta \nu}} = \frac{\kappa_F \mu_0 V_s M_s M_d / R_{\max}}{\sqrt{16k_B T m \Delta \nu / \tau_h}} \quad (2.1)$$

and we can see how it limits the signal-to-noise. Appropriate choices of materials and experimental modifications will be discussed as a means to minimize  $\alpha$ .

## 2.2 The Finite Element Method

The finite element method (FEM) is a numerical technique for obtaining approximate solutions to boundary-value problems (BVPs) of mathematical physics. For a comprehensive

reference, consult [23]. It was first proposed in the 1940's and was first applied to mechanical and structural problems in the 1950's. Two approaches have led to the success of FEM: Ritz's variational method and Galerkin's method. These techniques showed tremendous success in solving BVPs where a governing differential equation in a domain  $\Upsilon$  is defined by  $\mathcal{L}\phi = f$  with the boundary conditions on the boundary  $\Lambda$  that encloses  $\Upsilon$ .  $\mathcal{L}$  is a differential operator,  $f$  is the excitation function, and  $\phi$  is the unknown quantity. Electromagnetic problems typically involve Dirichlet or Neumann boundary conditions.

The Ritz method expresses the BVP in terms of a functional whose minimum corresponds to the governing differential equation under the given boundary conditions. The approximate solution is obtained by minimizing the functional with respect to variables that define an approximate solution. In Galerkin's method, approximate solutions  $\tilde{\phi}$  are found by a weighted residual method where weighting functions are selected such that integrating  $\mathcal{L}\tilde{\phi} - f$  over the domain is zero. While these methods showed early success, for most problems in electromagnetism solutions are not possible. This difficulty is overcome by dividing the problem into subdomains, each having a trial function. Then either the Ritz or Galerkin method can be employed. This is the basis of the finite element method.

During the past decade, important progress was achieved in finite element methods with regard to electromagnetic field simulations. The main idea behind the numerical solution of differential equations by the finite element method is the approximation of the solution by a linear combination of basis functions. The coefficients of the linear combinations are obtained from the variational or weighted residual problem, equivalent to a minimization problem. This involves a discretization of the solution domain into subdomains called finite elements. This discretization is often referred to as mesh generation and offers flexible approaches to two-dimensional (combining convex quadrangles with triangles) and three-dimensional (using four-node tetrahedra, right prisms, and general hexahedrons) problems. This is often the most computationally intensive part of the calculation and is most efficient when the aspect ratio of the elements is roughly one.

After mesh generation, the next step is interpolation. The solution is typically determined in terms of the unknown set of nodes on each element. The solution field is then configured by interpolating from the nodal values of that element, where the number of nodes per element and the choice of interpolation is dictated by the order of required accuracy and the degree of continuity needed for the governing equations. Following

this step, the element properties are derived. This involves assessing the contribution of each element to the coefficients of the nodal variables of the system of equations. The system is then assembled and all of the element properties are cast into one set of equations with the constraints of the boundary conditions of the problem. Finally, the system is solved and the assembled matrix gives a system of equations which can be solved for the unknown nodal variables. For linear problems, the equations are solved iteratively or by sparse matrix methods. Nonlinear problems are solved by Newton-like methods yielding linear systems which are then solved iteratively.

The problems solved in this thesis using finite element methods were based upon the Galerkin approach. In all cases, Maxwell 2D/3D<sup>©</sup> software from Ansoft Corporation<sup>1</sup> was used. Solution convergence was determined by two criteria: energy error and variable convergence. Maxwell computes the energy of the solution region by computing  $\mathbf{E} \cdot \mathbf{D}$  for electrostatic cases or  $\mathbf{B} \cdot \mathbf{H}$  for magnetic problems. The energy error is defined as the deviation from the zero divergence criteria imposed by Maxwell's equations, viz.  $\nabla \cdot \mathbf{D} - \rho$  and  $\nabla \cdot \mathbf{B}$ . The elements with the largest deviations are identified and adaptive mesh refinement is then used in these regions to improve the numerical approximations. The metric of convergence is set in this case by the user, typically an energy error of 0.1%. Alternatively, if Maxwell is computing a specific variable of the system, e.g. forces, torques, stresses, this solution can be monitored to determine convergence.

## 2.3 Magnetic Assembly

In this section, we consider the design of the magnet assembly including the symmetric array of detector and annulus as well as shaped magnetic pole pieces. Attention will be paid to configurations which optimize homogeneity and sensitivity.

### 2.3.1 Detector and Annular Magnet

#### 2.3.1.1 Magnetic Softening

The design of the detector and annular magnet is concerned with a system that provides good field homogeneity at the sample, results in maximization of the sensitivity, and gives a

---

<sup>1</sup>1. Ansoft Corporation, Pittsburg, PA. <http://www.ansoft.com>

contribution from magnetic softening such that the resonance frequency of the mechanical oscillator in the desired magnetic field is between 1 and 10 kHz.

The effects of magnetic softening may initially be considered by treating the detector magnet as a point dipole on axis with the annular magnet.[24] The dipole moment  $\mu$  has magnitude  $\pi M h_d r_d^2$  where  $M$  is the magnetization,  $h_d$  is the detector height, and  $r_d$  is the detector radius. If the assumptions of uniformly magnetized magnets directed along the  $z$ -axis is made, then magnetic field generated by the annulus at the detector is due to surface currents along the top and bottom cylindrical surfaces of the annulus and is given by

$$B_z(0) = \mu_0 M h_d \left[ (4r_o^2 + h_d^2)^{-1/2} - (4r_i^2 + h_d^2)^{-1/2} \right] \quad (2.2)$$

where  $r_{o,i}$  are the outer and inner radii of the annulus respectively. The gradient of the annulus' field exerts a force on the detector and for small detector displacement we find that this force is  $F(z) \approx \mu \frac{d^2 B_z}{dz^2}(0)$ . The sign of the magnetic spring constant  $k_{mag}$  is then shown to be negative,  $k_{mag} = -\mu \frac{d^2 B_z}{dz^2}(0)$ . The dipole approximation gives some intuition about how  $k_{mag}$  scales with detector height, radius, and annular gap. However, we have experimentally observed the dipole approximation underestimates the magnitude of  $k_{mag}$  by roughly a factor of four. Therefore, we now focus our attention on FEM simulations.

Table 2.1 shows the results of an extensive study of finite element simulations. Again, the approximation was made that both the detector and annular magnets were uniformly magnetized with the given  $M_s$ . This assumption should be valid in our experimental configurations given that the static magnetic field felt by these magnets will be 2 T. The simulations were conducted as follows: The force on the detector magnet was calculated at five positions along the  $z$ -axis where the maximum displacements were chosen such that  $k_{mag} = -\mu \frac{d^2 B_z}{dz^2}(z)$  was valid, typically  $\pm 5\%$  of  $h_d$ . The calculated force was plotted as a function of distance yielding a linear fit with slope  $-k_{mag}$ . During each simulation, only one parameter was varied in order to ascertain the geometric effects on  $k_{mag}$ . These are plotted in Figure 2.1. In Figure 2.1 (a) the  $k_{mag}$  dependence on  $g$  was found to be  $k_{mag} = -469.1 + 246.3g^{1/2} - 10.6g^{3/2}$  with  $R^2 = 0.98$ . The fit in Figure 2.1 (b) gives  $k_{mag} = -8.0 + 8.5M_s - 4.0M_s^2$  with  $R^2 = 0.999$ . Similarly in Figures 2.1 (c) and (d) we have  $k_{mag} = -28.6 - 7.1h_d$  ( $R^2 = 0.99$ ) and  $k_{mag} = 5.892 - 3.867r_d$  ( $R^2 = 0.99$ ). We find that  $k_{mag}$  varies linearly with  $r_d$  and  $h_d$ , varies as  $g^{3/2}$ , and varies quadratically with  $M_s$ .

The dependence on magnet height was found to be approximately twice as strong as the radius. Therefore, the magnet design is quite flexible and can easily modified to observe a desired  $k_{mag}$ .

$r_d$ ( $\mu\text{m}$ )	$h_d$ ( $\mu\text{m}$ )	$g$ ( $\mu\text{m}$ )	$M_s$ ( $\text{T}/\mu_0$ )	$k_{mag}$ ( $\text{N}/\text{m}$ )
10	8	3	1.6	-33.7
20	8	1	1.6	-131.1
20	8	3	1.6	-69.0
26	4	3	1.6	-49.2
26	8	3	1.6	-96.2
26	20	3	1.6	-168.6
26	40	3	1.6	-313.9
26	8	0.25	1.6	-371.1
26	8	1	1.6	-195.7
26	8	5	1.6	-58.8
26	8	10	1.6	-19.9
26	8	3	1.3	-63.6
26	8	3	2.0	-148.8
26	8	3	2.5	-234.0
40	8	3	1.6	-148.8

Table 2.1: Finite element simulations of the effective of  $k_{mag}$  on detector radius, height, annular gap, and saturation magnetization.

### 2.3.1.2 Detector Optimization

We have chosen an  $R_{\max}$  of  $34 \mu\text{m}$  based upon a sample size of  $50 \mu\text{m}$ . The electrodeposited magnetic materials should be low stress to prevent delamination and undue forces on the spectrometer assembly. These limitations set a maximum  $h_d$  of  $8 \mu\text{m}$  and we will now consider the optimal detector size with this constraint.

The total root-mean-squared (rms) force on the detector is given by the integral of the forces on dipole elements in the detector

$$F_{z,rms} = \frac{\beta}{\sqrt{2}} \int_V \hat{\mathbf{z}} \cdot \mathbf{dF} \quad (2.3)$$

where  $\beta$  is a scaling factor accounting for the amplitude of the Fourier component of the

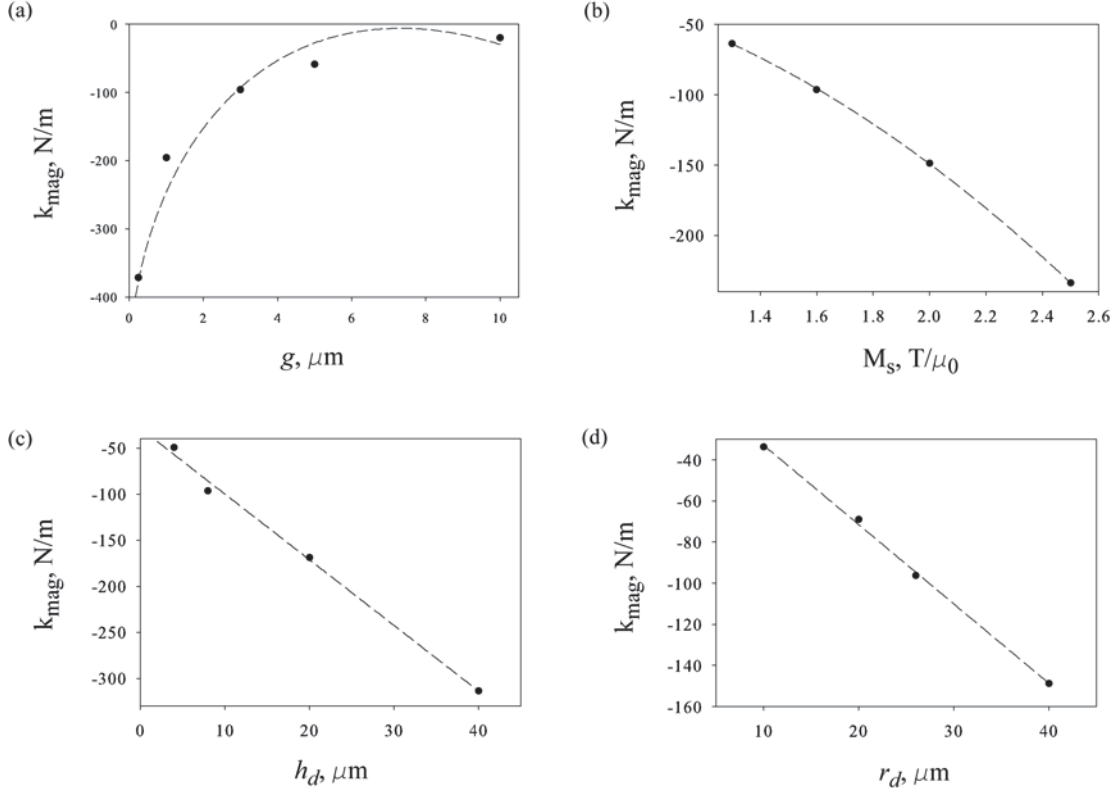


Figure 2.1: Plots of  $k_{mag}$  versus gap  $g$ , saturation magnetization  $M_s$ , detector height  $h_d$ , and detector radius  $r_d$ . The fit from the data in Table 2.1 is shown as a dotted line.

driving.[18] Using equation 1.25, this expression is equal to

$$F_{z,rms} = \frac{\beta}{\sqrt{2}} \frac{\mu_0}{4\pi} V_s M_s M_d \int_0^{2\pi} d\phi \int_{R_{\max}}^{\infty} z dz \int_0^{\rho(z)} \frac{9\rho^2 - 6z^2}{(z^2 + \rho^2)^{7/2}} \rho d\rho \quad (2.4)$$

$$= -\frac{3}{2} \frac{\beta}{\sqrt{2}} \mu_0 M_s M_d V_s \int_{R_{\max}}^{\infty} f(z, \rho(z)) dz \quad (2.5)$$

where  $f(z, \rho(z)) = \frac{z\rho^2}{r^5}$  and  $r = \sqrt{z^2 + \rho^2}$  is the the distance of the dipole element from the origin. The volume element of the detector id given by  $dV_d = \rho d\rho d\phi dz$ . Thus we have expressed the signal force as a functional that is parameterized by the shape function  $\rho$ . The noise force may be similarly calculated by considering the damping parameter  $\alpha$  and damping rate  $\gamma$

$$\alpha = m\gamma = \pi\gamma\eta \int_{R_{\max}}^{\infty} v(z, \rho(z)) dz \quad (2.6)$$

with  $v(z, \rho(z)) = \rho^2$ . Therefore, the optimal signal-to-noise ratio is given by extremizing

$$\frac{\left(\int_{R_{\max}}^{\infty} f(z, \rho(z)) dz\right)^2}{\int_{R_{\max}}^{\infty} v(z, \rho(z)) dz} \quad (2.7)$$

where the factors that do not depend on  $\rho$  have been eliminated. For the case of right cylindrical detectors this simplifies to a force

$$F_z = \frac{r_d^2}{2} \left[ \frac{1}{(r_d^2 + 1)^{3/2}} - \frac{1}{(r_d^2 + (h_d + 1)^2)^{3/2}} \right], \quad (2.8)$$

and the noise expression is equivalent to the volume of the detector plus added inertial mass,  $F_N = \pi r_d^2 h_d + \mathcal{M}$ .  $\mathcal{M}$  is actually an inert volume multiplied by the ratio of the inert material's density to the density of the magnet material. This can also be input as the inert mass divided by the magnet material's density and has units of volume.

In the signal-to-noise plots of Chapter 1, we considered a detector with no inert mass. For this idealized case, extremization of the signal-to-noise functional gives  $r_d^{opt} = 0.59R_{\max}$  and  $h_d^{opt} = 0.53R_{\max}$ . For a microfabricated spectrometer with a total mass of 2.9 times greater than the fiducial mass of the detector, a similar extremization gives  $r_d^{opt} = 0.83R_{\max}$  and  $h_d^{opt} = 1.17R_{\max}$  which gives a signal-to-noise ratio of 0.67 times that of the optimal case. In our case,  $h_d$  is fixed at  $8 \mu\text{m}$  giving an optimal detector radius of  $26 \mu\text{m}$ . In this configuration, the signal-to-noise ratio is 0.43 times that of the optimal case. Figures 2.2 and 2.3 show plots for both the optimal and our experimental case. We see for both configurations, the signal-to-noise is not sharply peaked.

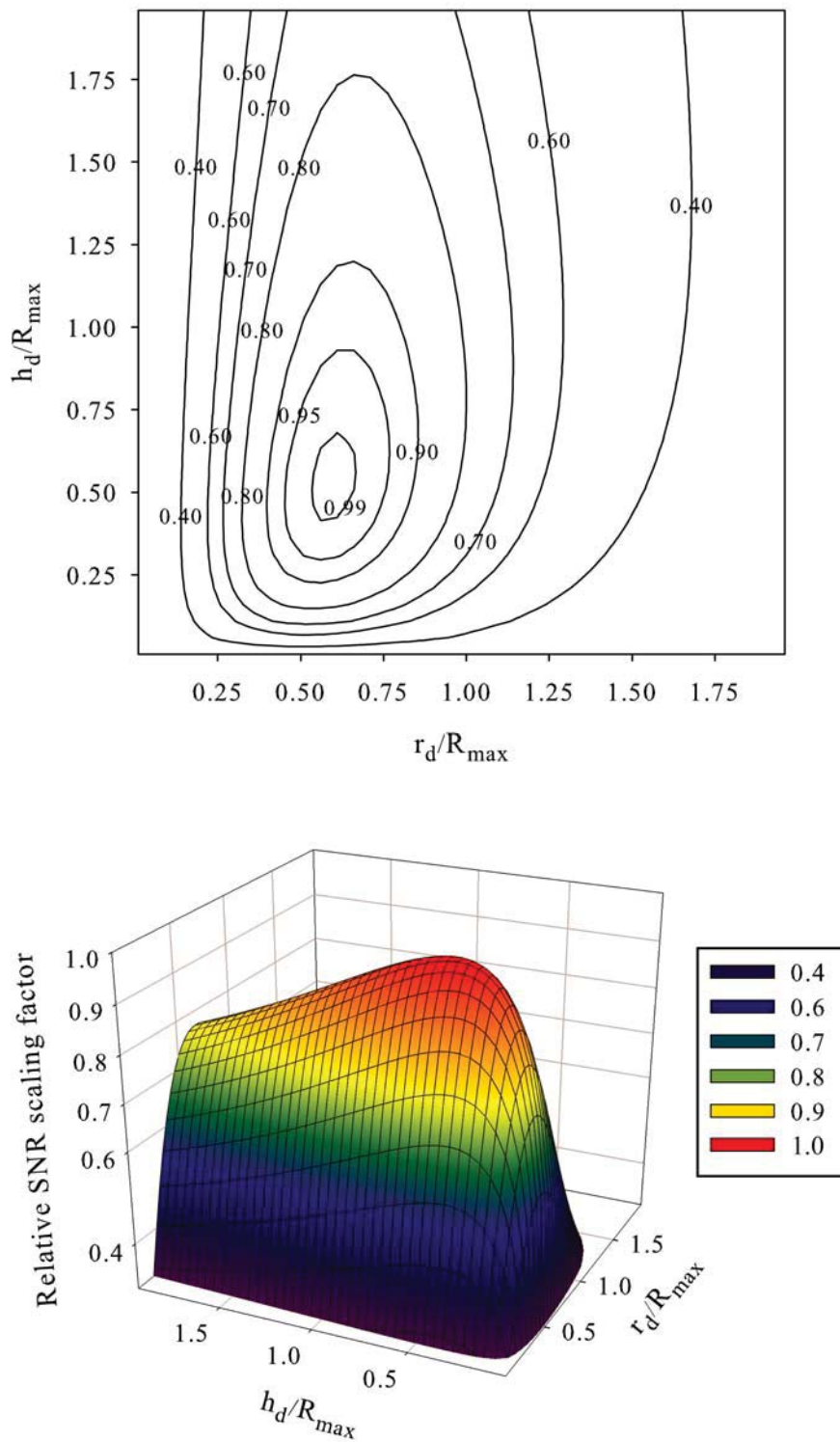


Figure 2.2: Signal-to-noise ratio versus the detector radius  $r_d$  and height  $h_d$  scaled by  $R_{\max}$ . The optimal sensitivity is observed for a detector with no added inert mass.

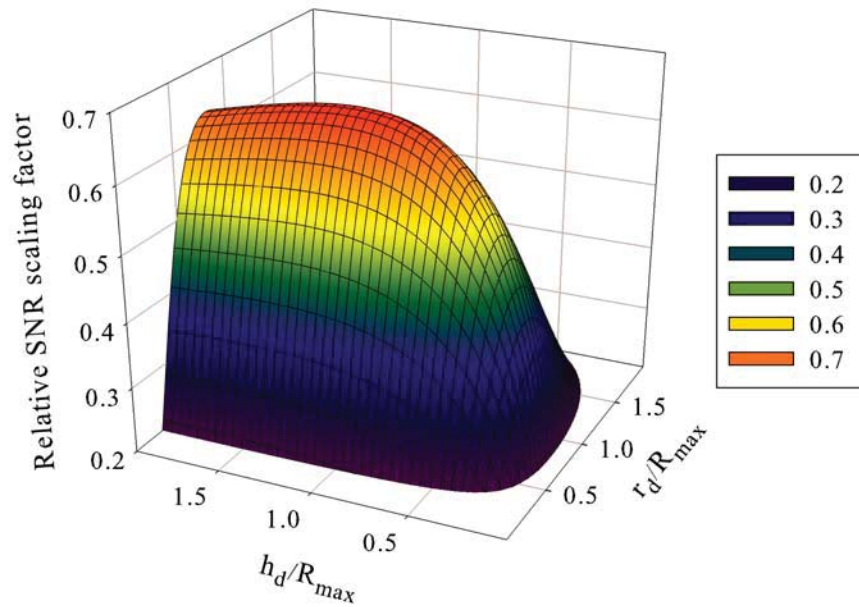
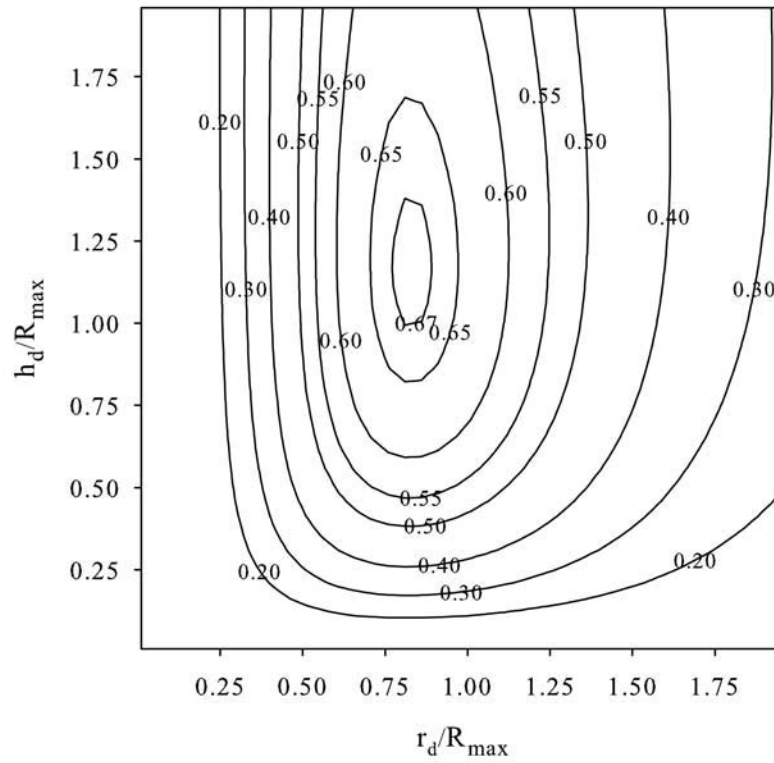


Figure 2.3: Signal-to-noise ratio versus the detector radius  $r_d$  and height  $h_d$  scaled by  $R_{\max}$ . In this case, the inert mass equals 2.9 times the detector mass.

### 2.3.1.3 Magnetic Materials

A goal of ours is to have a low-stress magnetic material for use in the detector and annular magnets. The magnetic material should have a  $M_s$  of  $1.6\text{-}2.0\text{ T}/\mu_0$  and have good resistance to corrosion by the buffered oxide etch (BOE) used during microfabrication. A ternary plot showing  $M_s$  as a function of common alloy concentrations is shown below in Figure 2.4. The data used to construct this plot was taken from [25, 26, 27]. Electrodeposition allows specifically patterned magnets to be incorporated onto the mechanical oscillator structures and may allow feature sizes below  $1\ \mu\text{m}$  to be incorporated for creation of the detector-annular gap and radial slits to mitigate eddy current damping by the use of appropriate photoresist molds. The alloy composition is controlled through adjusting bath salt and additive concentrations.

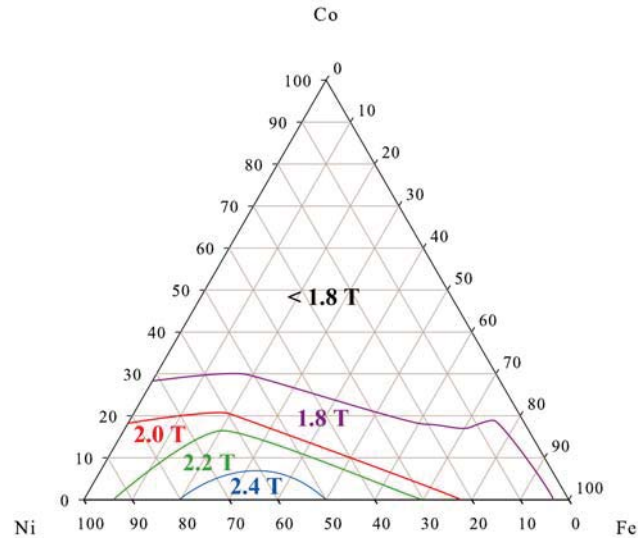


Figure 2.4: Ternary plot of saturation magnetization  $M_s$  as a function of nickel, cobalt, and iron concentrations in electrodeposited magnetic materials.

The electrodeposition process should allow the magnetic film to have optimized composition, deposition rate, internal stress, substrate-film adhesion, surface roughness, and magnetostriction. The permeability and coercivity of the magnetic film are secondary factors, as they do not effect the sensitivity or homogeneity of the device. Of greater importance is the conductivity of the film, which should be minimized to reduce eddy current damping effects.

Typically, materials with high  $M_s$  have very high stress, greater than 250 MPa, which will likely result in delamination of the film.[28, 29] Therefore, we seek materials with internal stresses of less than 80 MPa. Experimentally, we have observed that 85/15 Co:Ni films have saturation magnetizations of  $1.6 \text{ T}/\mu_0$  with internal stresses of 65 MPa. We are also investigating recent reports of CoNiFe alloys as superior candidates for future devices. SEM images of the annular and detector magnets as well as the photoresist molds used to fabricate them are shown below in Figure 2.5.

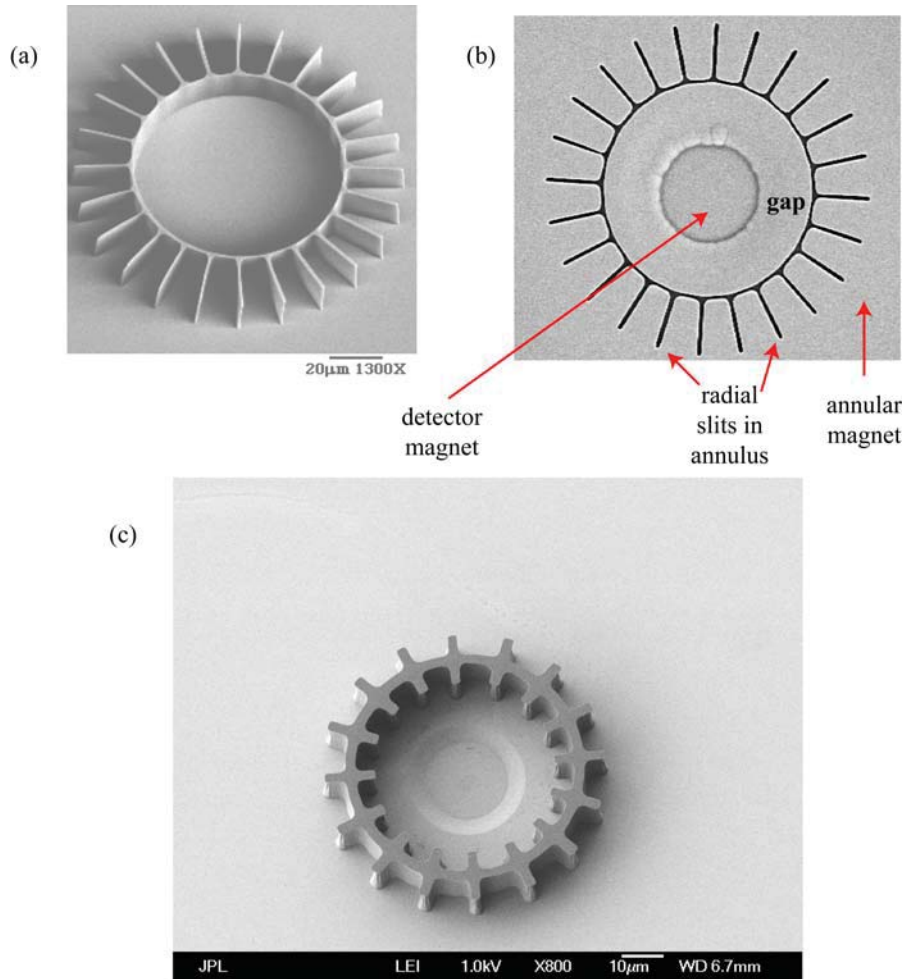


Figure 2.5: SEM images of microfabricated magnetic device structures. (a) Preliminary photoresist mold used to create the annular-detector magnet assembly. The “sunshine” pattern was used to create the annular radial slits to reduce eddy current damping [30]. The width of each slit is  $1 \mu\text{m}$  and the height  $10 \mu\text{m}$ . The ring of photoresist created the  $1 \mu\text{m}$  gap. (b) The results of using the photoresist mold in (a). (c) A modified photoresist design to include slits in both annular and detector magnets. The gap size is  $3 \mu\text{m}$  and the slits are  $3 \mu\text{m} \times 3 \mu\text{m}$ .

### 2.3.2 Static Magnetic Field

One of the biggest assets of the MEMS-based NMR spectrometer is its portability. In order to meet this goal and have a low-power device, permanent magnets must be used to provide the  $\mathbf{B}_0$  field. The on-axis magnetic field to a right cylindrical magnet may be calculated using the Biot-Savart law for a surface current  $\mathbf{K} = |\mathbf{M}| \hat{\phi}$  and is found to be

$$B_z(z) = \frac{\mu_0 M}{2} \left[ \frac{L/2 + z}{\sqrt{(L/2 + z)^2 + R^2}} + \frac{L/2 - z}{\sqrt{(L/2 - z)^2 + R^2}} \right] \quad (2.9)$$

for a cylinder of length  $L$  and radius  $R$ . As  $L \rightarrow \infty$ , we see that  $B_z(z) \rightarrow \frac{\mu_0 M}{2}$ . However, for spectroscopic studies in space we want to minimize this mass. Typical aspect ratios for these types of magnets are  $\frac{L}{R} = 1$ .

Conventional rare-earth magnetic materials such as NdFeB50 have magnetic retentivities  $B_r$  of 1.5 T and when cylindrical magnets of this material, even of optimized aspect ratio, are separated by 1 mm the magnetic field strength in the center of the two pole pieces was calculated to be 0.8 T. This limitation is illustrated by the following:

$$B_g = \frac{h_m}{d_m + h_m} \mu_0 H_c \approx \frac{h_m}{d_m + h_m} B_r \quad (2.10)$$

where  $B_g$  is the magnetic field strength between the pole pieces,  $h_m$  is the magnet height,  $d_m$  is the pole separation, and  $H_c$  is the coercive field strength of the permanent magnet material.[31]

It is possible to add a saturated iron truncated cone to each pole piece and shaping the iron piece in this manner causes a focusing of magnetic field lines, effectively providing a field higher than  $B_r$  between pole pieces.[32, 33] To ensure saturation magnetization for the annular magnets, the diameter of the bottom face of the iron pole must be at least the annular diameter, 2 mm. The iron pole piece is shown schematically in Figure 2.6. In the simulations  $d_{ct}$  was set at 20 mm,  $\theta_c$  was varied between  $0^\circ - 40^\circ$ , the field magnets used were cylindrical NdFeB50<sup>2</sup> magnets with a height of 10 mm and a diameter of 20 mm. The gap between the two iron pole faces was fixed at 1 mm. The focusing effect of the iron pole pieces is illustrated by observing the lines of magnetic flux, Figure 2.7. We observe

---

<sup>2</sup>These magnets are commercially available from Magnetic Solutions, Inc., <http://www.magnetic-solutions.com>.

that truncated cones significantly focus the magnetization into the desired region. Future designs may include the use of Halbach magnetic circuits given the recent development of homogeneous fields as high as 5 T generated inside them.[34, 35, 36, 37] Halbach designs may also reduce the fringing effects observed in Figure 2.7.

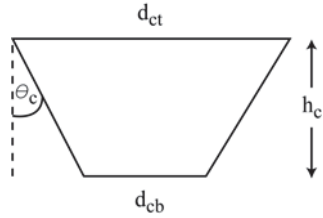


Figure 2.6: A cross-section of the truncated conical iron pole piece with top diameter  $d_{ct}$ , bottom diameter  $d_{cb}$ , pole height  $h_c$ , and cone angle  $\theta_c$ .

$\theta_c$ (deg)	$B_0$ at sample center (T)	Homogeneity (ppm)
0	0.61	0.2
10	0.82	1.9
20	1.39	4.5
30	1.76	11.8
33	1.98	25.6
40	2.87	57.1

Table 2.2: Magnetic field and field homogeneity as a function of saturated iron pole cone angle.

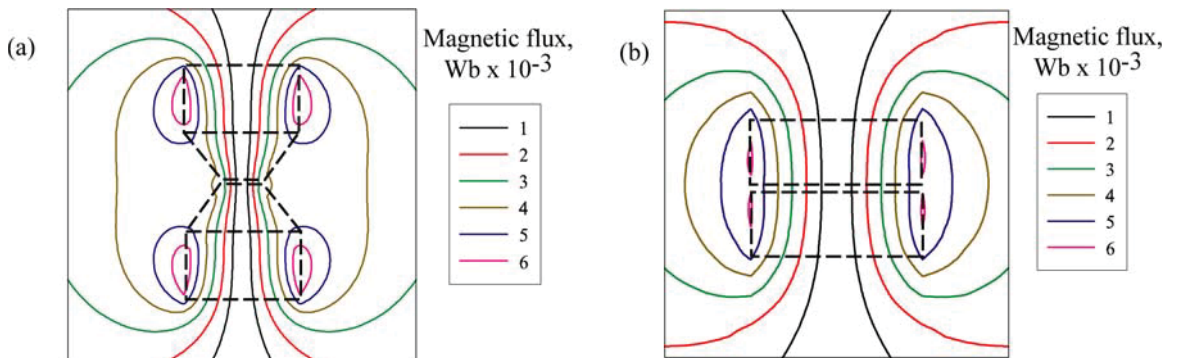


Figure 2.7: Plots of absolute value of the magnetic flux through field magnets. The values on the right hand side are negative. The gap is 1 mm in both cases. (a) Symmetric arrangement of 10 mm tall, 20 mm diameter NdFeB50 right cylinders capped by saturated iron truncated cones with a top diameter of 20 mm and  $\theta_c = 33^\circ$ . (b) NdFeB50 cylindrical magnets with the same dimensions as (a).

### 2.3.3 Field Homogeneity and Lineshape Analysis

In an optimal spectrometer configuration the gap between the detector and annular magnet  $g$  is minimized to maintain high field homogeneity at the sample. We will assume that by design of source magnets, the detector and annular magnets will be fully saturated acquiring a magnetization of  $1.6 \text{ T}/\mu_0$  for electroplated CoNi (85:15) alloys.

In the simulations that follow, the magnetic fields were calculated self-consistently by using a Legendre polynomial expansion to order 20 using Mathematica<sup>®</sup>. Contributions from the static field<sup>3</sup>, annular, and detector magnet were included in calculating the field at the sample. The annular planes were separated by  $2R_{\text{max}} = 68 \mu\text{m}$ . During the microfabrication process, it is likely that detector magnet will not be exactly coplanar with the annulus due to anisotropy during electroplating. Therefore, we have considered detector displacements of  $\pm 500 \text{ nm}$  from the annular plane. These simulations are plotted in Figure 2.8. Qualitatively, we observe that perfect detector alignment gives a nominally homogeneous field across the sample and field gradients of odd order essentially vanish. Minor shimming will be necessary to remove the second order gradients. For  $g = 1 \mu\text{m}$  and  $3 \mu\text{m}$   $|\partial^2 B_z / \partial z^2| = 9.2 \text{ T/m}$  and  $31.2 \text{ T/m}$  respectively. Significant inhomogeneities caused by misalignment of the detector were observed and method to correct for this will be discussed in the next section of this chapter.

We have also simulated the NMR lineshape for  $g = 1$  and  $3 \mu\text{m}$ . These simulations were conducted by expansion of the components of the total magnetic field in a series of Legendre polynomials followed by calculating the magnetic field at randomly chosen points in a  $50 \mu\text{m}$  spherical volume. The values of the magnetic field were then plotted as probability distribution functions, Figures 2.9(a) and 2.10(a). These simulations suggest that even for misalignment of the detector by  $\pm 500 \text{ nm}$ , the distribution of Larmor frequencies over the sample is significant. Variations across the sample were taken into consideration in Figures 2.9(b) and 2.10(b). The force between the dipole in the detector and the dipole element in the sample is sensitive to their relative positions and as expected, this local sensitivity weighted considerably distorts the lineshape for displaced detectors.

The lineshapes in Figures 2.9(b) and 2.10(b) for the centered detector were fitted to a

---

<sup>3</sup>The static field magnets in these simulations were assumed to be cylindrical, but with the appropriate magnetization and coercivity to provide the field of the truncated conical pole pieces. The validity of this assumption is based upon the homogeneous field at the sample provided by selective shape and placement of the pole pieces.

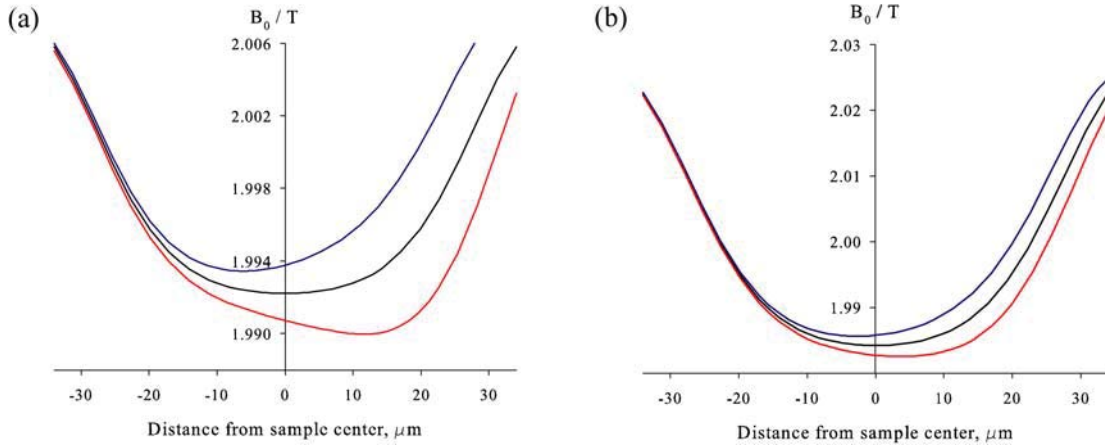


Figure 2.8: Calculation of the magnetic field at positions along the symmetry axis for the proposed spectrometer for a detector-annular gap  $g$  of  $1 \mu\text{m}$  (a) and  $g$  of  $3 \mu\text{m}$  (b). The black line represents a centered detector, the blue line represents the detector 500 nm above the plane, and the red line the detector 500 nm below the plane.

Lorentzian and the full-width at half maximum linewidths were found to be 16.6 kHz and 48.2 kHz respectively. An additional simulation for  $g = 250 \text{ nm}$  gave a linewidth of 5.3 kHz. Therefore, even for a relatively large gap, the expected linewidths are well under our target Rabi frequency of 100 kHz.

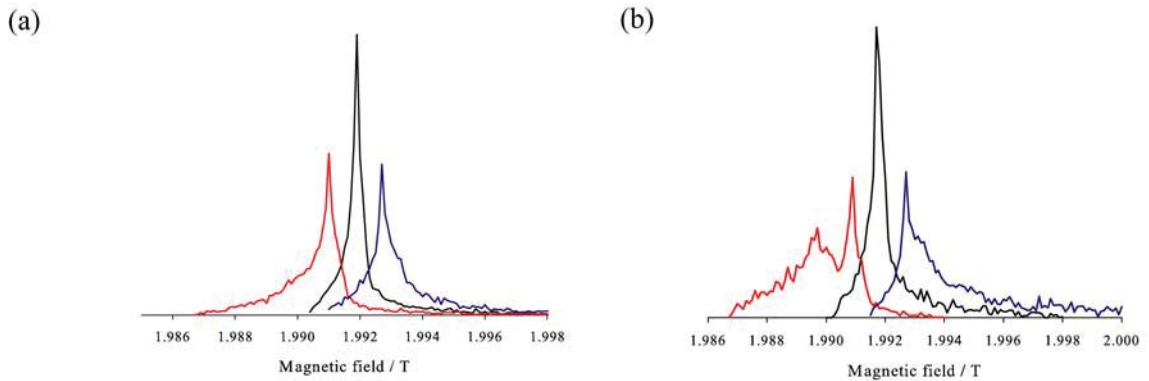


Figure 2.9: Distribution of magnetic fields with a  $50 \mu\text{m}$  diameter spherical sample with  $r_d = 26 \mu\text{m}$  and  $g = 1 \mu\text{m}$ . (a) The black line is for a centered detector, the red line for the detector displaced 500 nm above the annulus, and the blue line for the detector displaced 500 nm below the annulus. Simulated lineshapes adjusted for sensitivity variations in the sample volume.

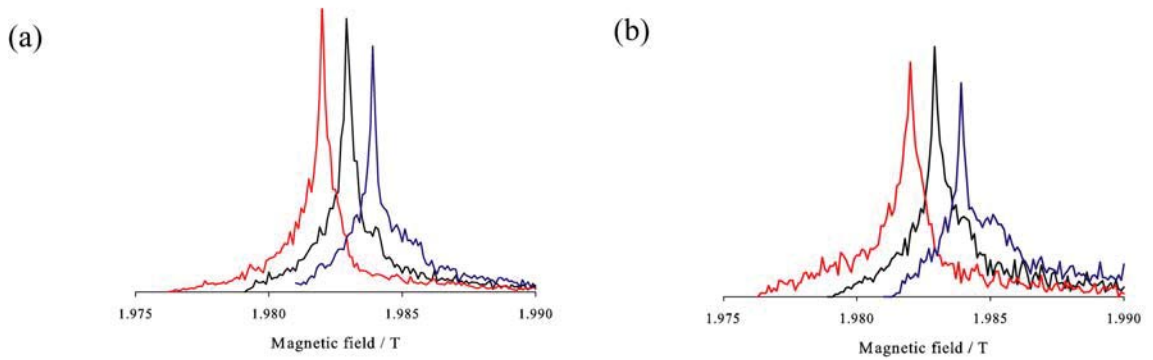


Figure 2.10: Distribution of magnetic fields with a  $50\ \mu\text{m}$  diameter spherical sample with  $r_d = 26\ \mu\text{m}$  and  $g = 3\ \mu\text{m}$ . (a) The black line is for a centered detector, the red line for the detector displaced  $500\ \text{nm}$  above the annulus, and the blue line for the detector displaced  $500\ \text{nm}$  below the annulus. Simulated lineshapes adjusted for sensitivity variations in the sample volume.

## 2.4 Mechanical Oscillator Design

The mechanical oscillator should be designed in a way to constrain the detector magnet motion to the  $z$ -axis, with torsional rigidity to prevent the detector magnet to torque in its bore, be constructed of a low-dissipation material that is relatively easy to use in standard microfabrication processes, and counteract the negative magnetic spring constant. A natural choice of a material is silicon, given the explosive volume of known microfabrication methods and its inherent low dissipation leading to high sensitivity to resonant driving as well as its relatively large Young's modulus. The material properties of silicon as a function of temperature are shown in Table 2.3.[38]

T (K)	$E_{[100]}$ (N/m <sup>2</sup> )	$\rho$ (kg/m <sup>3</sup> )	$\phi$	$C_p$ (J/m <sup>3</sup> -K)	$\alpha$ (1/K)	$\chi$ (m <sup>2</sup> /s)
300	$130 \times 10^9$	2330	0.28	$1.66 \times 10^6$	$2.60 \times 10^{-6}$	$8.6 \times 10^{-5}$
150	$130 \times 10^9$	2331	0.28	$9.91 \times 10^5$	$6.11 \times 10^{-7}$	$4.3 \times 10^{-4}$
70	$130 \times 10^9$	2331	0.28	$3.45 \times 10^5$	$-4.46 \times 10^{-7}$	$2.48 \times 10^{-3}$

Table 2.3: Temperature dependent material properties of silicon.

### 2.4.1 Rectangular Beams

From the standpoint of fabrication ease, a rectangular beam fixed at both ends (clamped-clamped) with a concentrated mass at the center is the simplest oscillator geometry to

consider. The clamped-clamped beam requires that the displacement of the beam and its first derivative at the clamped points is zero. An oscillator with this shape and boundary conditions has a resonance frequency  $\nu_h$  in Hz of

$$\nu_h = 13.86 \sqrt{\frac{EI}{L^3 (M + 0.375m_b)}} \quad (2.11)$$

where  $E$  is the elastic modulus,  $L$  is the beam length,  $M$  is the concentrated mass at the center of the beam,  $m_b$  is the mass of the beam, and  $I$  is the polar moment of inertia given by  $I = \frac{1}{12}b^3c$  where  $b$  is the beam height and  $c$  is the beam width.[39] The factor of 0.375 accounts for the motional mass of the beam. Equation (2.11) assumes small displacements of the beam and purely elastic materials allowing the use of Euler-Bernoulli equations. The polar moment of inertia is derived by considering flexural vibration of the oscillator in the  $xz$ -axis where  $I = \int x^2 dx dy$  where  $I$  is the area moment of inertia of the beam's cross section about the  $y$ -axis. In the limit  $M \gg 0.375m_b$ ,  $\nu_h$  scales as  $L^{-3/2}b^{3/2}c^{1/2}$ .

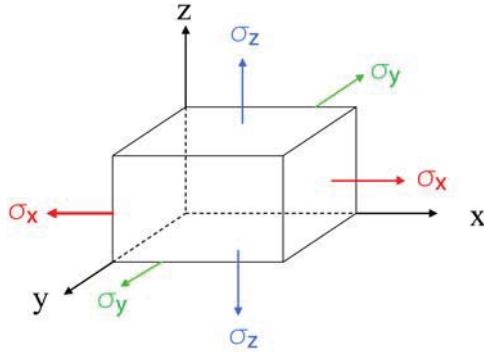


Figure 2.11: Components of normal stress.

It is useful at this point to consider the stresses in the beam during excitation. A stress quantity that is proportional to the strain energy density associated with a change in shape (with a zero volume change) at a material point is the von Mises stress which is defined by

$$\sigma_{vm} = \frac{1}{\sqrt{2}} \sqrt{(\sigma_x - \sigma_y)^2 + (\sigma_y - \sigma_z)^2 + (\sigma_z - \sigma_x)^2 + 6(\tau_{xy}^2 + \tau_{yz}^2 + \tau_{zx}^2)} \quad (2.12)$$

and is a scalar measure of the stress state (the normal and shear stresses) at any point within a body.[39] The von Mises criterion is an experimentally based law that can be used to determine whether the stress state in a material causes plastic flow (or yielding).

Note, the von Mises criterion is based on the strain energy density associated with a change in shape (with a zero volume change) at a material point.  $\sigma_{x,y,z}$  are the normal stress components as defined in Figure 2.11. These are defined by

$$\sigma_i = \frac{E}{(1 + \phi)(1 - 2\phi)} [\varepsilon_i(1 - \phi) + \phi\varepsilon_j + \phi\varepsilon_k]$$

where  $\varepsilon_{i,j,k}$  are the components of strain and  $i, j$ , and  $k$  cycle over the Cartesian axes. The  $\tau$  components are sheer stress tensors and found from the product the the sheer modulus and sheer strain. When  $\sigma_{vm}$  is greater than the yield stress, the material will buckle, and thus we will examine the this using the finite element approach.

For a beam with dimensions ( $L = 400 \mu\text{m}$ ,  $b = 5.3 \mu\text{m}$ ,  $c = 20 \mu\text{m}$ ) the calculated von Mises stress during flexural vibration was found to be  $1.762 \text{ N/m}^2$  and the yield stress was found to be  $1.827 \text{ N/m}^2$ . This assumed a  $Q$  of 1000. These calculated values suggest that use of a mechanical stress buttress is necessary to prevent buckling of the mechanical oscillator. Adding a  $40 \mu\text{m} \times 40 \mu\text{m} \times 40 \mu\text{m}$  silicon cube to the beam, for the same  $Q$ , gives  $\sigma_{vm}$  equal to  $2.872 \text{ N/m}^2$  and a yield stress of  $9.784 \text{ N/m}^2$ .

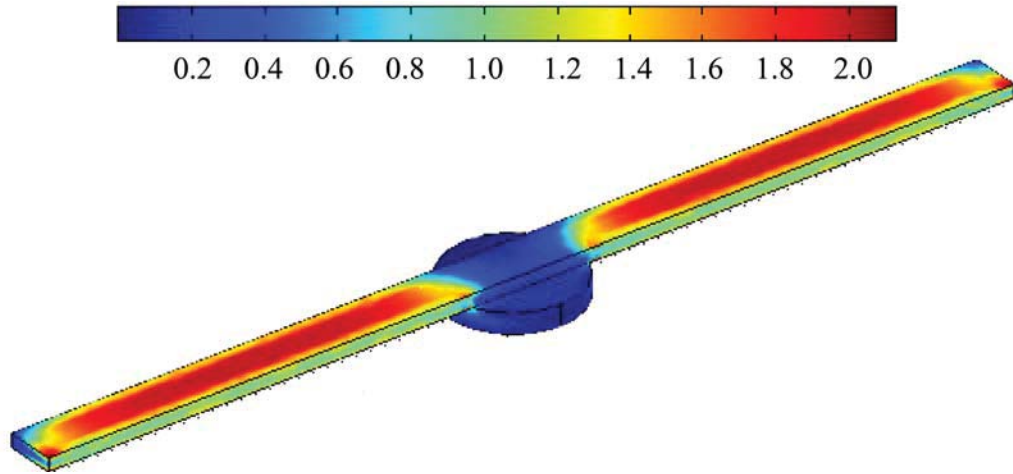


Figure 2.12: Calculated von Mises stress for flexural vibration of a resonator without a stress buttress. The units of stress are given in  $\text{N/m}^2$ .

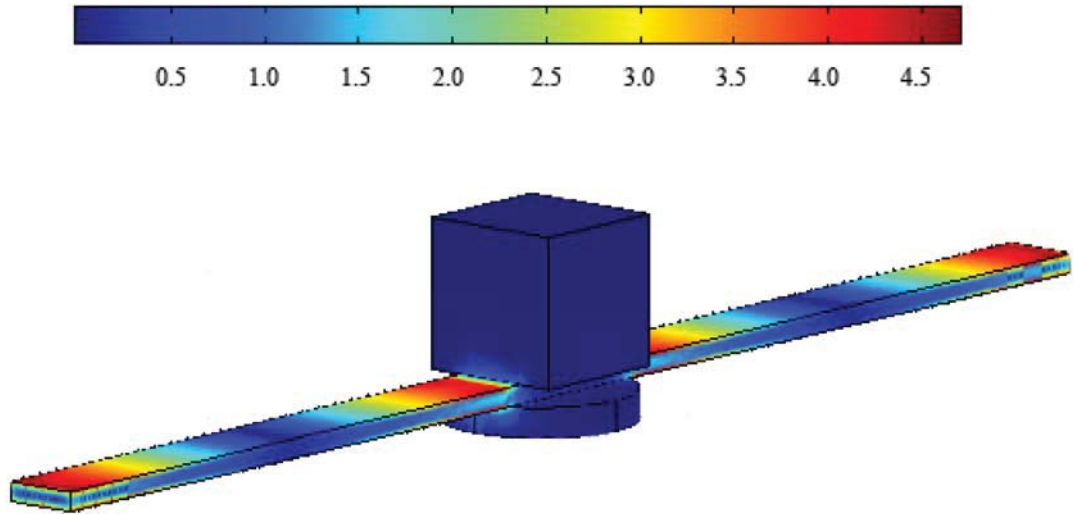


Figure 2.13: Calculated von Mises stress for flexural vibration of a resonator with a stress buttress. The units of stress are given in  $\text{N}/\text{m}^2$ .

Based upon our current magnetic assembly designs, ( $r_d = 26 \mu\text{m}$ ,  $h_d = 8 \mu\text{m}$ ,  $g = 26 \mu\text{m}$ ,  $M_s = 1.6 \text{T}/\mu_0$ ),  $k_{elas}$  must be larger than  $96.2 \text{N}/\text{m}$ , to prevent snapping of the beam due to a negative effective spring constant. The effective spring constant is given by  $k_{eff} = \omega_h^2 (M + 0.375m_b)$  and for a goal of  $\omega_h = 2\pi \cdot 1 \text{kHz}$  we observe that it will be necessary to balance to within a few percent. This is displayed in Table 2.4.

$c$ ( $\mu\text{m}$ )	$k_{elas}$ ( $\text{N}/\text{m}$ )	$\nu_h$ ( $\text{kHz}$ )
5	81.3	imaginary
5.1	86.3	imaginary
5.2	91.4	imaginary
5.3	96.8	7.0
5.4	102.4	22.3

Table 2.4: Oscillator resonance frequency as a function of beam height.

### 2.4.2 Capacitive Transduction

While it is possible to thin the beams with reasonable control by etching, control over the etch rate on the scale of  $100 \text{nm}$  is necessary. One method to avoid this is to use capacitive transduction. When a voltage is applied between the clamped-clamped beam and an electrode, an electrostatic force is induced on the beam. For a beam of width  $b$  coated with a conductor of width  $\xi$  and a separated electrode of width  $w$ , the parallel plate

capacitance is

$$C = \frac{\varepsilon_0 A}{\delta + \frac{b}{\varepsilon_r}} \quad (2.13)$$

where  $A$  is  $\xi w$ ,  $\varepsilon_r$  is the relative dielectric constant of the dielectric layer (in this case the silicon beam), and  $\delta$  is the distance separation between the beam and electrode. The electrostatic force applied to the beam is found by considering the power delivered to the capacitance

$$F_e = \frac{1}{2} V^2 \frac{\varepsilon \varepsilon_0 A}{\left(\delta + \frac{b}{\varepsilon_r}\right)^2} \quad (2.14)$$

where  $V$  is the potential difference between the beam and electrode and  $\varepsilon$  accounts for the reduction in the parallel-plate capacitance due to the roughness of the metal-to-dielectric interface. This is observed quite often in the MEMS shunt switch literature.[40] Note that when  $\delta = 0$ , the electrostatic force is

$$F_e = \varepsilon_r \left( \frac{1}{2} \frac{\varepsilon \varepsilon_r \varepsilon_0 A V^2}{t_d^2} \right) = \varepsilon_r \left( \frac{QE}{2} \right) \quad (2.15)$$

compared to the case where there is no dielectric layer,  $F_e = \frac{QE}{2}$ . Therefore, even for very small metal-dielectric gaps, a large attractive force exists. The restoring force due to this electrostatic force results in actuation of the oscillator. This force is given by

$$F_r = k_{elas} (\delta - \delta_0) + k_s (\delta - \delta_0)^3 = k_{cap} (\delta - \delta_0). \quad (2.16)$$

It should be stated that this model neglects charge injection onto the dielectric, but should provide a reasonable account of the physics due to the quadrupolar field felt by the charge on the dielectric. The snap down voltage is given by

$$\begin{aligned} V_s &= \left( \delta + \frac{b}{\varepsilon_r} \right) \sqrt{\frac{2F_e}{\varepsilon \varepsilon_0 A}} \\ &= \left( \delta + \frac{b}{\varepsilon_r} \right) \sqrt{\frac{2k_{cap}}{\varepsilon \varepsilon_0 A} (\delta - \delta_0)} \end{aligned} \quad (2.17)$$

and should allow the oscillator to be shimmed by more than the 500 nm case we considered in the lineshape estimate.

While this design allows magnet shimming, it does not allow modulation of the resonance

frequency readily. A simple arrangement is to use a three-plate capacitor as shown in Figure 2.14. In addition to adjusting the oscillator's equilibrium position and its resonance frequency, this device will also be configurable to include active feedback with voltages at  $\omega_h$  on the detector magnet's position during spin inversion.

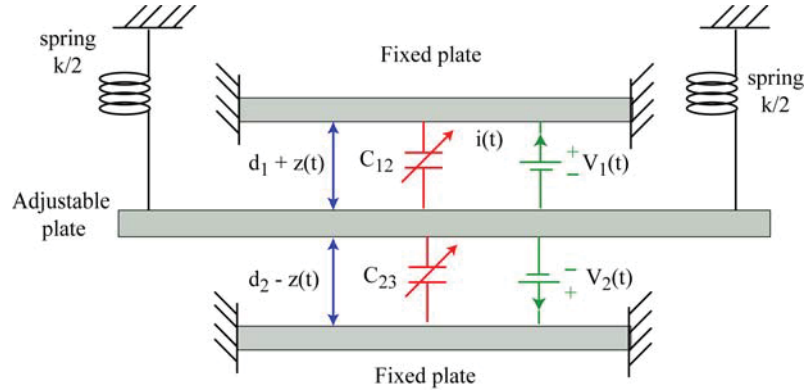


Figure 2.14: Model of electromechanical tunable three parallel plate capacitive transducer.

This model serves as a starting point to study the capacitive transducer. Here the top and bottom plates are mechanically fixed while the middle plate is suspended by two springs, each with a spring constants  $k/2$ . Without loss of generality, the voltages applied to the plates may be time-dependent. The equilibrium between the electrostatic and mechanical forces is given by

$$\begin{aligned}
 kz &= \frac{1}{2} \frac{dC_{12}}{dz} V_1^2 + \frac{1}{2} \frac{dC_{23}}{dz} V_2^2 \\
 &= -\frac{1}{2} \frac{\epsilon_0 A V_1^2}{(d_1 + z)^2} + \frac{1}{2} \frac{\epsilon_d \epsilon_0 A V_2^2}{(d_2 - z)^2}.
 \end{aligned} \tag{2.18}$$

Experimentally, we are consigned by the mechanical stress buttress and magnets and will therefore employ the design shown in Figure 2.15. Finite element simulations were conducted on a device with this geometry and those results are displayed in Figure 2.16. The force on the center plate was calculated as functions of  $d_1$  and the potential differences between the three plates. From the fitted data, we roughly find that the capacitive force constant is

$$k_{cap} \approx -\frac{AV_1^{5/2} \epsilon_0}{d_1^3} + \frac{AV_2^{5/2} \epsilon_0 \epsilon_{Si}}{d_2^3}.$$

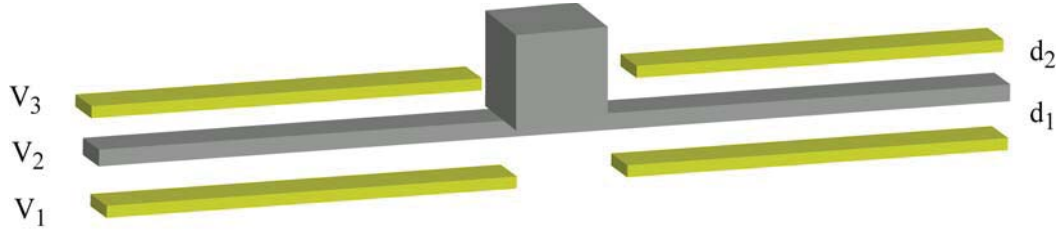


Figure 2.15: Three-plate capacitive force transducer. This arrangement allows relatively large surface area capacitor plates to be used to increase the force on the oscillator. In its working configuration the oscillator will have gold plated on the beam to act as the electrode at potential  $V_2$ . The plates are separated by distances  $d_1$  and  $d_2$ , with  $d_1$  fixed at  $5\ \mu\text{m}$ .

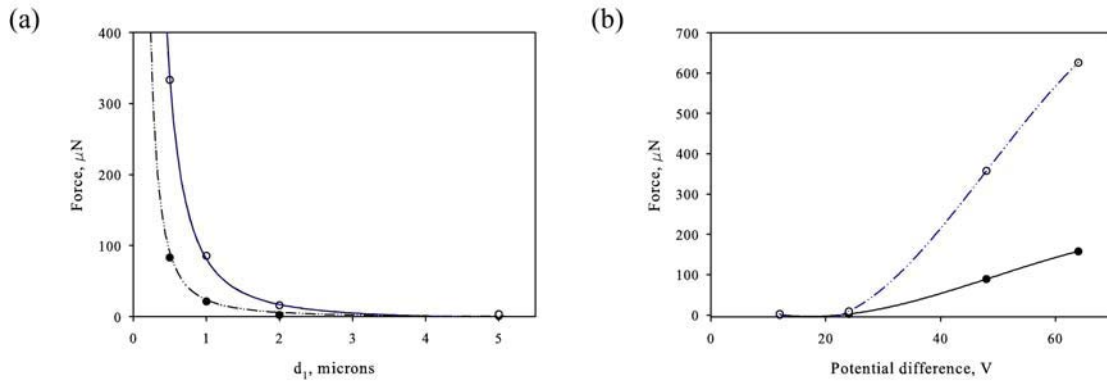


Figure 2.16: FEM analysis of three-plate capacitive transducer. (a) The force on the center plate as a function of distance separation  $d_1$ . The solid dots corresponds to a 48 V potential difference and the hollow dots correspond to a 24 V potential difference. The same potential difference existed between the middle and bottom plates. (b) The force on the center plate as a function of potential difference. The solid dots corresponds to a  $1\ \mu\text{m}$   $d_1$  separation, while the hollow dots correspond to a  $500\ \text{nm}$   $d_1$  separation. The same potential difference existed between the middle and bottom plates.

### 2.4.3 Resonator Characterization

In Figure 2.17, we see a scanning electron micrograph of a microfabricated mechanical oscillator. This device had a resonance frequency of 111 kHz in a  $B_0 = 0$  field. The measured  $Q$  in air was found to be 76 and the vacuum measurement gave a  $Q$  of 347. It is suspected that the low observed  $Q$  of this device is due to damping by magnetic material remaining in the  $1\ \mu\text{m}$  gap. The  $Q$  should be improved with the updated design of a  $1\ \mu\text{m}$  gap.

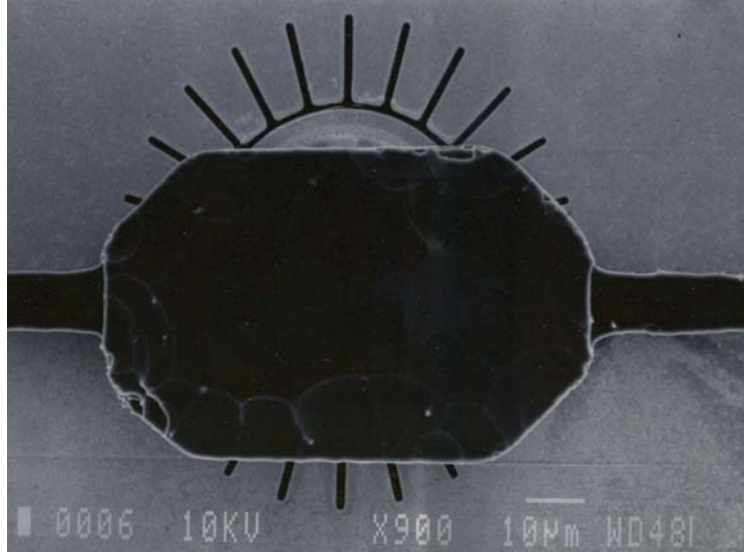


Figure 2.17: Scanning electron microscope image of a microfabricated mechanical oscillator. The detector and slitted annular magnets are clearly seen under the mechanical stress buttress. The buttress dimensions are  $40\ \mu\text{m} \times 40\ \mu\text{m} \times 40\ \mu\text{m}$ , the beam width is  $10\ \mu\text{m}$ , the beam height is  $6\ \mu\text{m}$  and the beam length is  $400\ \mu\text{m}$ . SEM image courtesy of Choonsup Lee.

## 2.5 Damping

The mechanical properties of micro- and nano-electromechanical systems is of great technological importance. For an optimized system, the force resolution of a detector is limited by the thermomechanical noise, which is a consequence of mechanical energy conversion to heat due to coupling of the mechanical oscillator with its environment. However, the sensitivity is ultimately determined by the sources of damping in the system. We will consider both internal and external sources of damping and will show that the greatest contribution is through generation of azimuthal eddy currents by the moving detector magnet.

### 2.5.1 Air Damping

Air damping increases as the resonator's surface-to-volume ratio and is proportional to pressure.[41] The damping is given by

$$Q_{air} = \frac{\omega_n b \rho}{k_m P} = \frac{k_n^2}{k_m P} \left(\frac{b}{L}\right)^2 \sqrt{\frac{E \rho}{12}} \quad (2.19)$$

where  $\omega_n$  is the resonator frequency in the  $n$ th mode with mode constant  $k_n$ ,  $b$  is the resonator thickness,  $\rho$  is the material density,  $L$  is the resonator length,  $P$  is the pressure and  $k_m$  is a molecular parameter of the air given by  $\sqrt{\frac{32M}{9\pi RT}}$  with  $M$  as the molecular weight of air, and  $R$  is the gas constant. For a beam with thickness  $5.3\ \mu\text{m}$ , length  $400\ \mu\text{m}$  at a pressure of  $1 \times 10^{-3}$  torr,  $Q_{air}$  is of order  $10^5$ . Therefore, air damping is insignificant at our size scales and experimental pressure. This is consistent with the observation that the mean free path of air molecules at this pressure is  $76\ \text{mm}$ .

### 2.5.2 Thermoelastic Damping

As acoustic modes propagate throughout a solid, there is a mode of damping due to a nonlinear interaction with a thermal bath of excited state elastic modes. If these modes, thermal phonons, have a mean free path smaller than the wavelength of the acoustic mode, then the system obtains regions of local temperature. If the phonon relaxes fast compared to acoustic mode, then the temperature distribution is well-defined and the phonon excitations may be treated collectively. This interaction is governed by the thermal expansion coefficient and in an isotropic solid  $\alpha = \frac{1}{L} \frac{\partial L}{\partial T}$ . The excitation of flexural modes in a thermoelastic solid creates a damping mechanism whereby the coupling between the strain and temperature fields is dissipated as heat through temperature gradients. This damping is known as thermoelastic damping and sets an upper bound on even an ideally designed mechanical resonator's ringdown time. The magnitude of thermoelastic damping depends on only the material's temperature dependent thermodynamic properties. For flexural vibrations of thin resonators, the peak damping as a function of frequency is dependent upon the beam dimensions.

The problem of thermoelastic damping was first treated by Zener [42, 43] who showed that the damping can be approximated by a single relaxation time which depends upon the height of the beam  $b$  and the material's thermal diffusivity  $\chi$ . This problem was recently treated exactly by Lifshitz and Roukes.[44] Their model considers a flexural excitation in a beam causing both displacement and temperature fields and their assumption that the length  $L$  of the beam is large compared to the width  $c$  and height  $b$  is valid in all resonator designs we have considered.

The thermoelastic damping in a thin beam is given by

$$\frac{1}{Q_{TED}} = \frac{E\alpha_T^2 T_0}{C_p} \left( \frac{6}{\xi^2} - \frac{6}{\xi^3} \frac{\sinh \xi + \sin \xi}{\cosh \xi + \cos \xi} \right) \quad (2.20)$$

where

$$\xi = \frac{a_n b^{3/2}}{2\sqrt[4]{3}L\sqrt{l_T}} \quad (2.21)$$

where  $a_n$  is the mode number ( $a$  for the fundamental mode is 4.73),  $\alpha_T$  is the thermal expansion coefficient,  $C_p$  is the heat capacity per unit volume at constant pressure, and  $l_T = \chi\sqrt{\frac{\rho}{E}}$  is the thermal diffusion length.

For a beam at 300 K of length  $400 \mu\text{m}$  and height  $5.3 \mu\text{m}$  we observe that  $Q_{TED}$  is  $2.64 \times 10^5$  corresponding to a  $\tau_h$  of 90 s for a 1 kHz resonance frequency. This drops off quite rapidly as  $\omega_h$  increases, falling to 800 ms for a 50 kHz oscillator. Therefore, we observe that thermoelastic damping will not contribute significantly unless the resonance frequency for the mechanical oscillator of this size scale is above 50 kHz. The magnetic softening effects will ensure this condition is met.

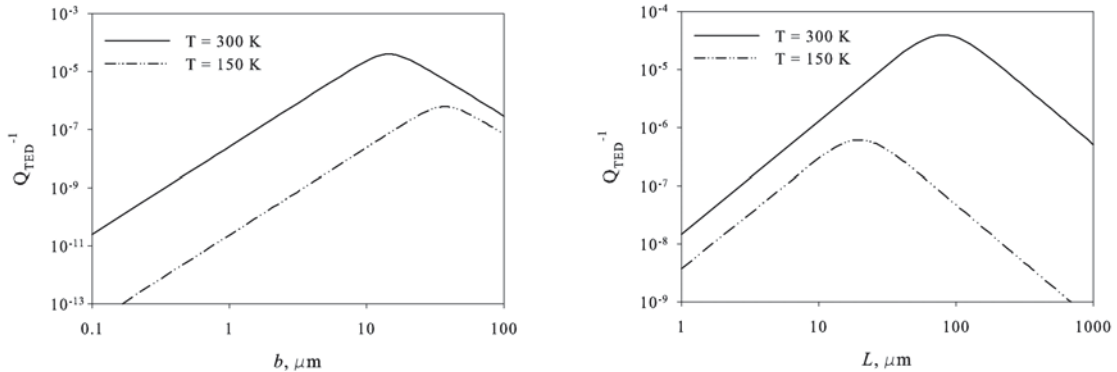


Figure 2.18: Thermoelastic damping as a function of beam height  $b$  and beam length  $L$  for a rectangular silicon beam. In the first plot,  $L$  was fixed at  $400 \mu\text{m}$  and in the second plot  $b$  was fixed at  $5.3 \mu\text{m}$ .

### 2.5.3 Clamping Losses

We now consider a mechanism of damping by which vibrational energy of a resonator is dissipated through its support. When a resonator undergoes flexural vibration, both a vibrating shear force and moment is exerted on its clamped ends resulting in excitation of

elastic waves in the support. We will make the assumption that the elastic wavelength of the transverse propagating wave is much larger than the beam thickness  $b$  and that the flow of vibrational energy into the clamping points is irreversible. This simplification has allowed Euler-Bernoulli theory to be used to derive an analytical expression of the damping due to clamping loss.[45] Furthermore, the losses due to the vibrating moment are several orders of magnitude smaller than the shear force and will be neglected.

For a clamped-clamped beam, this was found to be

$$Q_{clamp} = \left[ \frac{2.43}{(3 - \phi)(1 + \phi)} + \frac{1.91}{\Xi} \right] \frac{1}{(\beta_n \zeta_n)^2} \left( \frac{L}{b} \right)^3 \quad (2.22)$$

where  $\beta_n$  is the mode constant ( $\beta$  for the fundamental mode is 1.5056),  $\zeta_n$  is the mode shape factor ( $\zeta$  for the fundamental mode is  $-0.983$ )

$$\zeta_n = \frac{\sin(\pi\beta_n) + \sinh(\pi\beta_n)}{\cos(\pi\beta_n) + \cosh(\pi\beta_n)} \quad (2.23)$$

and  $\Xi$  arises from consideration of the Fourier transform of the two dimensional elastic wave propagating during excitation and is given by

$$\begin{aligned} \Xi = & (1 - \phi^2) \int_0^1 \frac{\varepsilon^2}{\sqrt{1 - \varepsilon^2}} \cos\left(\sqrt{1 - \varepsilon^2} \frac{\omega_h L}{c_L}\right) d\varepsilon \\ & + 2(1 + \phi) \int_0^1 \sqrt{1 - \varepsilon^2} \cos\left(\sqrt{1 - \varepsilon^2} \frac{\omega_h L}{c_L}\right) d\varepsilon. \end{aligned} \quad (2.24)$$

$\varepsilon$  is a parameter that relates the mode shape factor  $\zeta$  to the the longitudinal propagation velocity  $c_L$ ,  $\zeta = \varepsilon c_L / \omega_h$ . The longitudinal and transverse propagation velocities are given by

$$c_L^2 = \frac{E}{\rho(1 - \phi^2)} \text{ and } c_T^2 = \frac{E}{2\rho(1 + \phi^2)} \quad (2.25)$$

with corresponding wavelengths of  $\lambda_{L,T} = \frac{2\pi c_{L,T}}{\omega_h}$ . Substituting these values into equation 2.22 gives

$$Q_{clamp} = 0.44 \left( \frac{L}{b} \right)^3 \quad (2.26)$$

and for our case,  $L = 400 \mu\text{m}$  and  $b = 5 \mu\text{m}$ , this gives  $Q_{clamp} = 2.28 \times 10^5$ .

### 2.5.4 Surface Damping

As a resonator is scaled down, the surface-to-volume ratio increases, and it is possible that surface losses may become significant. The surface loss is mostly caused by surface stress, which arises from adsorbates on the surface or by surface defects. These defects usually arise from exposure to etching chemicals which leave tens of nanometer layers of SiO<sub>2</sub> or hydrides on the surface.[46] The surface dissipation is modeled by considering the complex Young's modulus  $E_c = E + iE_d$  where  $E_d$  is the dissipative component. For a clamped-clamped beam, the stored energy can be expressed as

$$W_0 = \frac{1}{6}cbE \int_0^L \sigma_{\max}^2(x) dx \quad (2.27)$$

where  $\sigma_{\max}$  is the strain occurring on the top or bottom surface of the beam during flexural vibration. For a surface thickness of  $\delta$  and complex modulus  $E_c$ , the energy loss per cycle due to the surface layer is

$$\Delta W_s = 2\delta E_d \left( c + \frac{b}{3} \right) \int_0^L \sigma_{\max}^2(x) dx \quad (2.28)$$

giving

$$Q_{surface} = \frac{bc}{b + 3c} \frac{E}{2E_d\delta}. \quad (2.29)$$

Typically, both  $E_d$  and  $\delta$  are difficult to estimate or even experimentally measure [46] but a  $Q_{surface}$  for similarly configured resonators has been found to be roughly  $1.5 \times 10^5$ . [47]

### 2.5.5 Eddy Current Damping

The primary means of experimentally observed damping is through eddy currents. Azimuthal eddy currents are generated due to the detector magnet moving up and down through the annular plane as shown in Figure 2.19. Garret Leskowitz presented an analytical model for eddy current damping for magnets at the millimeter scale.[18] This model neglected the time dependence of eddy currents.

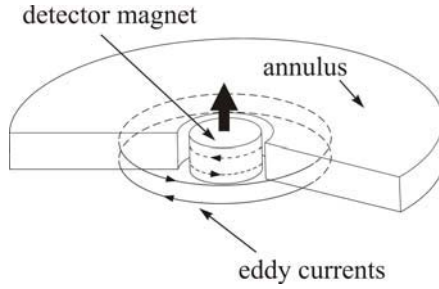


Figure 2.19: Azimuthal eddy currents due to relative motion of magnets.

If the motion of the magnet is confined to the symmetry axis, its velocity is given by  $\mathbf{v} = v\hat{\mathbf{z}}$ , and by this symmetry preservation the electric field can be expressed as

$$\mathbf{E} = -vB_\rho\hat{\phi} \quad (2.30)$$

where  $B_\rho$  is the azimuthal component of the magnetic field and  $\hat{\phi}$  is a unit vector in this cylindrical coordinate frame. The induced currents  $\mathbf{J}(r) = \rho\mathbf{E}(\mathbf{r})$  are also azimuthal and the dissipated power density is given by

$$W = \mathbf{J} \cdot \mathbf{E} = \sigma v^2 B_\rho^2. \quad (2.31)$$

The detector moves at a velocity  $v(t)$  whose frequency depends on the mechanical oscillator resonance frequency

$$v(t) = v_0 \cos \omega_h t \quad (2.32)$$

and the power density can be expressed as

$$\begin{aligned} P(t) &= \sigma v^2(t) \int_V B_\rho^2 dV \\ &= \alpha v^2(t) \end{aligned} \quad (2.33)$$

where  $\alpha$  is the damping parameter in equation (2.1). Leskowitz [18] also showed that this damping is scale-invariant and is given by

$$\alpha = 2 \frac{\rho \pi^2 r_d^2 h_d}{\tau_h}. \quad (2.34)$$

The scale invariance was confirmed by finite element simulations, but the observed damping

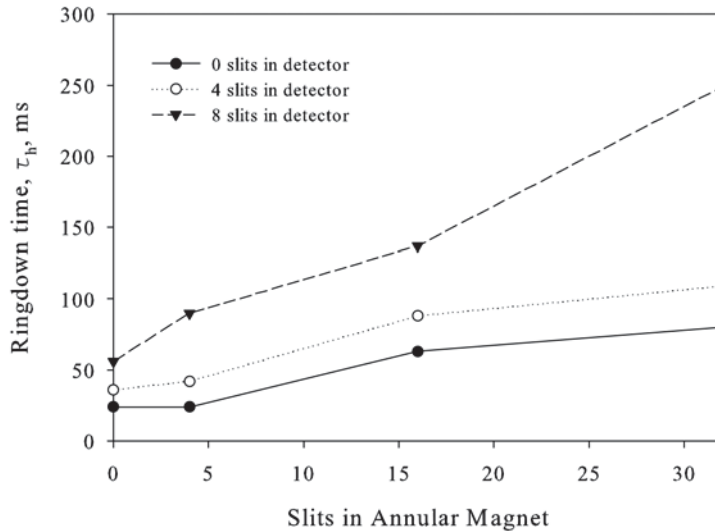


Figure 2.20: Experimental measurement of eddy current damping effects for the millimeter scale spectrometer. The oscillator ringdown time  $\tau_h$  is plotted as a function of the number of radial slits in the annulus for three detector configurations.

rate for the millimeter scaled device was a factor of 3.5 higher than the analytical result. The numerical result is in closer agreement with experiments.

We have measured the effects of eddy current damping for our millimeter-scale spectrometer. In these experiments, between zero and 32 radial slits were added to the annulus. The width of these slits was  $80\ \mu\text{m}$  and their length was  $500\ \mu\text{m}$ . The annulus was made from mu-metal (HyMu80) with a saturation magnetization of  $1\ \text{T}/\mu_0$  and a conductivity of  $1.61 \times 10^6\ \text{S/m}$ . The annulus had a radius of 15.25 mm and a height of 3 mm. The detector was also made of mu-metal and had  $60\ \mu\text{m}$  radial slits of length was  $200\ \mu\text{m}$ , with a radius of 1.5 mm and a height of 3 mm. The ringdown time measurements were made at a pressure of 1 m torr and the values of the motional mass were corrected in the cases of slitted detector magnets for removal of magnetic material. These results are plotted in Figure 2.20. We observed improvements in the ringdown time from the case of no slits in either magnet to 32 slits in the annulus and 8 in the detector of a factor of 10. In these experiments the size of the gap was  $100\ \mu\text{m}$ .

In his Ph.D. thesis, Louis Madsen described a case to minimize eddy current damping by using magnets made of packed nanoparticles.[30] For this case, we will consider spherical particles and calculate the dissipation in a single sphere. We will assume that the magnetic

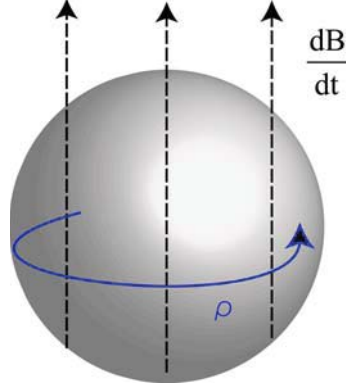


Figure 2.21: Spherical magnetic nanoparticle. Symmetry requires that the eddy currents to be azimuthal where  $\frac{d\mathbf{B}}{dt}$  is along  $\hat{\mathbf{z}}$ .

fields that arise from the induced eddy currents are small enough not to affect nearby particles. This assumption is analogous to assuming that the resistivity of the material is infinitely large or that the relative velocities of the moving and stationary magnets is small.

The first-order changes to the local field  $\mathbf{B}$  are given by  $\frac{d\mathbf{B}}{dt} = \frac{d\mathbf{B}}{dz} \frac{dz}{dt}$  where  $\frac{dz}{dt}$  is the longitudinal velocity of the moving magnet. If  $\frac{d\mathbf{B}}{dt}$  is uniform over the sphere, higher order terms may be neglected and we can calculate the electromotive forces in the sphere. We first note that along a circular path a distance  $\rho$  from the symmetry axis of the sphere,  $\int \mathbf{E} \cdot d\mathbf{l} = E \int dl = 2\pi\rho E$ . Therefore,

$$2\pi\rho E = \int \int \nabla \times \mathbf{E} \cdot \hat{\mathbf{n}} d\sigma \quad (2.35)$$

$$E = \frac{1}{2\pi\rho} \int \int \left| \frac{\partial \mathbf{B}}{\partial t} \right| d\sigma = \frac{\partial \mathbf{B}}{\partial t} \frac{1}{2}\rho \quad (2.36)$$

because  $\frac{\partial \mathbf{B}}{\partial t} \parallel \hat{\mathbf{n}}$  and we are assuming it is uniform over the particle.

The frictional coefficient  $\alpha$  is given by the dissipated power  $P = \sigma E^2$  where  $\sigma$  is the conductivity. This is also the rate at which work is done by the friction in a time  $\tau_f$ .

$$P = \frac{1}{\tau_f} \int \mathbf{F} \cdot d\mathbf{l} = \frac{1}{\tau_f} \int \alpha \mathbf{v} \cdot \mathbf{v} dt = \alpha v^2. \quad (2.37)$$

So

$$\alpha v^2 = \int \sigma E^2 dV = \int \sigma \left( v^2 \left( \frac{\partial \mathbf{B}}{\partial z} \right)^2 \frac{1}{4} \rho^2 \right) (r^2 \sin \theta dr d\theta d\phi) \quad (2.38)$$

$$\alpha = \frac{2}{15}\pi\sigma \left(\frac{\partial\mathbf{B}}{\partial z}\right)^2 r^5$$

where  $r$  is the sphere radius.

This gives a damping rate  $\gamma$  of

$$\gamma = \frac{\alpha}{m} = \frac{2}{15}\pi\frac{\sigma}{m} \left(\frac{\partial\mathbf{B}}{\partial z}\right)^2 r^5 \quad (2.39)$$

and since  $\gamma$  is calculated per particle, over the volume  $V$  of the packed magnet there are  $N_{mag}$  particles with

$$N_{mag} = \frac{V}{\frac{4}{3}\pi r^3} \varrho \quad (2.40)$$

where  $\varrho$  is the packing factor. The maximum packing density that can be observed is hexagonally closed packed,  $\varrho = 0.76$ . There the total damping  $\gamma_{tot}$  is given by  $\gamma N_{mag}$

$$\gamma_{tot} = \frac{1}{10}\varrho\frac{V}{m}\sigma r^2 \left(\frac{\partial\mathbf{B}}{\partial z}\right)_{vol}^2 \quad (2.41)$$

where  $\left(\frac{\partial\mathbf{B}}{\partial z}\right)_{vol}^2$  is averaged over the volume of the entire magnet. It would appear that  $\gamma_{tot}$  scales as the square of the nanoparticle radius, contrary to the prediction of Leskowitz.[18] However,  $r$  is a scaled radius depending on the fractionation of the total magnet volume over each nanoparticle and therefore equation (2.41) is consistent with the observation of Leskowitz when this is taken into consideration.

As an example, if the initial damping rate for a  $52\ \mu\text{m}$  diameter detector is broken into magnets of  $500\ \text{nm}$  size,  $\gamma$  is found by

$$\left(\frac{0.5\ \mu\text{m}}{52\ \mu\text{m}}\right)^2 \gamma \approx 10^{-4}\gamma. \quad (2.42)$$

Therefore, if a detector is fabricated out of packed nanoparticles it may be possible to remove eddy current damping as the primary limitation on the oscillator ringdown time. Ultimately, this must be balanced with the decreased homogeneity for packed nanoparticle detectors.

## 2.6 Radiofrequency Excitation

### 2.6.1 Spin Inversion

The oscillator is driven by inverting the nuclear magnetization of the sample twice per oscillator period. Even in an optimal spectrometer configuration, the spread of Larmor frequencies is of order 10's of kHz. Therefore, appropriate means must be taken to invert the inhomogeneously broadened spins with minimal loss in magnetization and with the avoidance of thermalization with the transverse magnetic field over a time period comparable to the spin-lattice relaxation time during inversion  $T_{1a}$ . The thermalization losses are given by  $\frac{\tau}{2T_{1a}}$  where  $\tau$  is the oscillator period. This requirement sets the relaxation time at  $\frac{T_{1a} + \tau}{2\varepsilon T_{1a} + \tau}$  with  $\varepsilon$  as the fraction of magnetization loss per pass.

Adiabatic rapid passage (ARP) is a well-documented means of efficient inversion of a population of inhomogeneously broadened spins.[48] In the rotating frame, the magnetization evolves according the torque equation described in Chapter 1 and is given by

$$\frac{d}{dt}\mathbf{M} = \gamma_n \mathbf{M} \times \mathbf{B}_{eff} = \gamma_n \mathbf{M} \times \left( B_1 \hat{\mathbf{i}} + \frac{\omega(t) - \omega_0}{\gamma_n} \hat{\mathbf{k}} \right) \quad (2.43)$$

where  $\hat{\mathbf{i}} = \hat{\mathbf{x}} \cos \phi(t) - \hat{\mathbf{y}} \sin \phi(t)$  and  $\hat{\mathbf{k}} = \hat{\mathbf{z}}$  are unit vectors in the rotating frame,  $\{\hat{\mathbf{x}}, \hat{\mathbf{y}}, \hat{\mathbf{z}}\}$  are laboratory-frame unit vectors, and  $\phi(t) = \frac{d}{dt}\omega(t)$ . In an efficient ARP cycle,  $\mathbf{B}_{eff}$  is followed by the sample magnetization vector  $\mathbf{M}(t)$  if the offset frequency  $\Delta(t) = \omega(t) - \omega_0$  is swept such that the angle  $\theta(t) = \tan^{-1}(\Delta(t)/\gamma B_1)$  changes linearly with time. This condition requires

$$\left| \frac{d\theta}{dt} \right| \ll \sqrt{\gamma_n^2 B_1^2 + \Delta^2} \quad (2.44)$$

and  $\left| \frac{d\theta}{dt} \right|$  is maximized when  $\Delta = 0$  which results in a relatively weak  $\mathbf{B}_{eff}$ .

Hardy [49, 50] observed that by using tangent-based sweeps, the ARP cycling could be done a faster rate far from resonance, therefore allowing more efficient inversion of spin magnetization. This frequency sweep has the form

$$\omega(t) = \omega_0 - \omega_s \tan(\omega_s \alpha_{ARP} t) \quad (2.45)$$

where  $\omega_s$  is a sweep shape parameter and where  $\alpha_{ARP} = \frac{2}{\omega_s T} \tan^{-1}\left(\frac{\Omega}{\omega_s}\right)$  where  $T$  is the total sweep time and  $2\Omega$  is the sweep width. This inversion sequence also requires much

less rf power than other methods, which reduces drift of the oscillator resonance frequency during experiments.

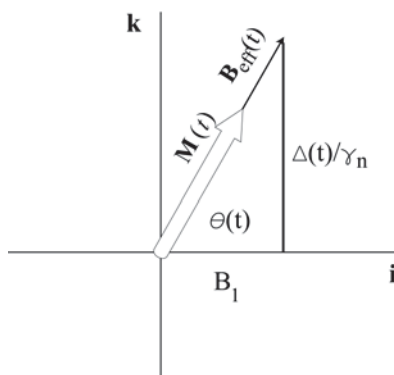


Figure 2.22: The basis of adiabatic rapid passage (ARP). In the rotating-frame, the offset frequency  $\Delta(t)$  is swept such that the angle  $\theta(t) = \tan^{-1}(\Delta(t)/\gamma_n B_1)$ .

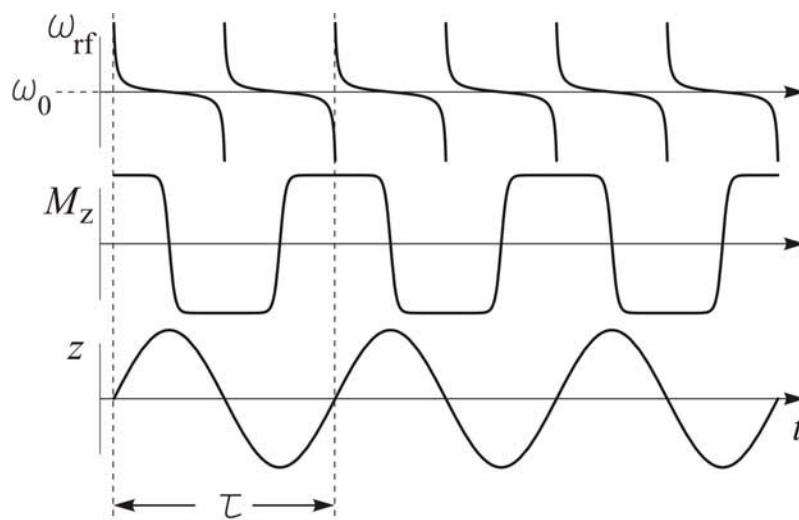


Figure 2.23: Illustration of driving the mechanical oscillator with efficient ARP.  $\omega_{rf}$  is swept in accordance with equation 2.45, and there are two sweeps per mechanical oscillator period  $\tau$ . Both sweeps occur from the same side of the center frequency  $\omega_0$ .  $d\omega_{rf}/dt$  is maximized when the magnetization  $\mathbf{M}$  is nearly along the static field. We observe that  $z(t)$  is  $90^\circ$  out-of-phase with the driving force.

In our experiments we sweep from the same side of the NMR line on every inversion to avoid spurious excitation of the oscillator by rf currents in the coil. This is illustrated in Figure 2.23. Thus, the predominant Fourier components due to non-NMR driving will be at twice the oscillator frequency. To avoid complications from the inversion ending at

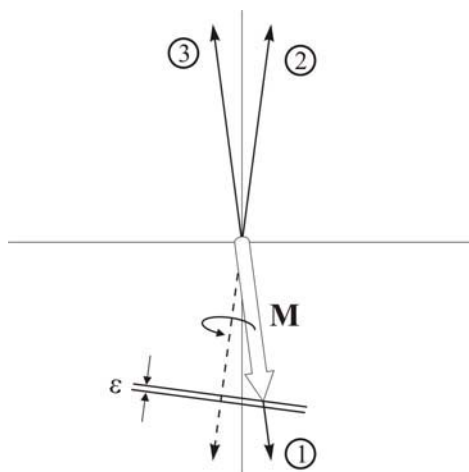


Figure 2.24: Phase cycling for efficient ARP in the rotating frame. After a single pass through resonance, the magnetization **1** is not perfectly inverted and on the second pass **2**, we observe that **M** will not be aligned with the effective field. A transverse component of **M** is dephased causing a fractional loss of  $\varepsilon = 1 - \cos 2\theta$ . A  $180^\circ$  phase shift of the rf, placing the effective field at **3**, eliminates this loss.

$\mathbf{B}_{eff}$ , which causes the the magnetization to have a non-vanishing transverse component, a  $180^\circ$  phase shift is applied on every other pulse. This phase-cycling improves the driving time by a factor of four.[30] Figure 2.24 details this phenomenon.

## 2.6.2 Excitation Coil

The most common excitation coil for NMR is the solenoid. Solenoids do not provide rigid structures for sample mounting and without significant modification do not allow for effective dissipation of heat during excitation. Heating of the mechanical oscillator causes the resonance frequency to drift during an experiment, resulting in decreased efficiency in driving. Therefore, we have constructed a new design which simply consists of two parallel conductive sheets evaporated on a silicon “I-beam.” The I-beam has dimensions  $10\text{ mm} \times 500\ \mu\text{m} \times 450\ \mu\text{m}$  (LxWxH) and has a  $50\ \mu\text{m}$  hole through the center to allow placement of samples. The silicon gap above and below the hole is kept at  $3\ \mu\text{m}$  to give our desired  $R_{max}$  of  $34\ \mu\text{m}$ . This arrangement is shown in Figure 2.25.

We would like to use a 100 kHz Rabi frequency for rf excitation of the spins to ensure complete inversion. Since the experiments will be done in the rotating frame, an additional factor of two is necessary and thus the  $B_1$  field must have a strength of 4.7 mT. In Figures

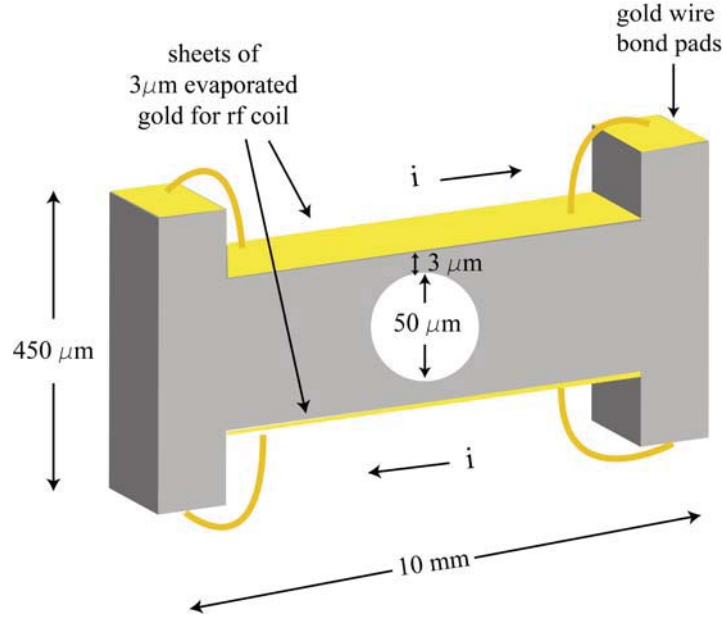


Figure 2.25: Radiofrequency excitation coil and silicon coil and sample holder. The length of the evaporated gold along the narrow portion of the silicon “I-beam” is chosen to be  $5.4 \mu\text{m}$  to allow the entire spectrometer to reside in this cavity. The posts in the I-beam will serve to align the two pieces of the spectrometer together and will provide a wire bond contact point for radiofrequency currents.

2.26 and 2.27 we show the results of a finite element simulation whose purpose was to identify the current necessary to generate this  $B_1$  field and to get a sense of the rf homogeneity across the sample. We find that the necessary current to generate a 4.7 mT  $B_1$  field is 0.527 A and the ac resistance  $R_{ac}$  at 90 MHz is  $0.216 \Omega$ . The field homogeneity is comparable to solenoidal microcoils, but requires a higher current to generate the  $B_1$  field.[51] At 90 MHz, the skin depth through gold is  $5 \mu\text{m}$  and since our coil thickness is  $3 \mu\text{m}$ , skin depth effects are not important.

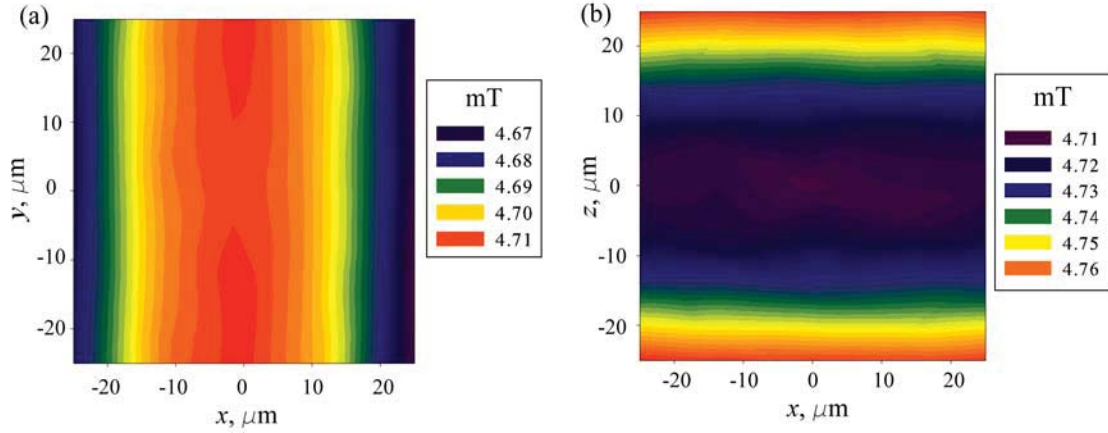


Figure 2.26:  $B_1$  magnetic field homogeneity provided by parallel-plate rf coil. (a)  $B_{yz}$  contour map through the sample center. (b)  $B_{xy}$  contour map of magnetic field through the sample center.

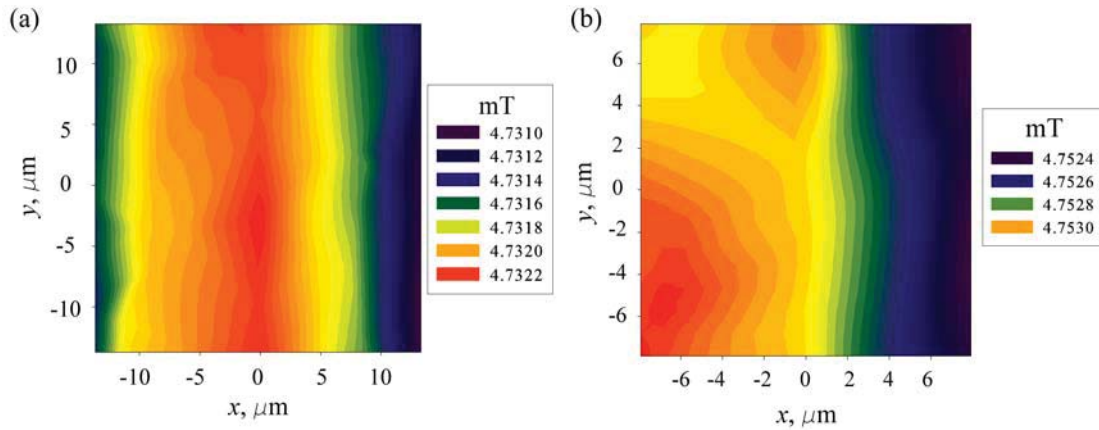


Figure 2.27:  $B_1$  magnetic field homogeneity provided by parallel-plate rf coil. (a)  $B_{xy}$  contour map of magnetic field 10  $\mu\text{m}$  above the sample center. (b)  $B_{xy}$  contour map of magnetic field 20  $\mu\text{m}$  above the sample center.

Operating at this current, the required power  $P = I^2R$  is 60 mW. The heat transport equations were solved numerically and it was found that for this power, the temperature rise of the mechanical oscillator is 2.1  $^\circ\text{C}$ . This relatively small temperature increase is due to mounting the coil on a large silicon support and the surrounding silicon in the mechanical oscillator structure. The spectrometer geometry is shown in Figure 2.39 and in Figure 2.28 we show a scanning electron micrograph of a wafer containing the I-beam structures and a rectangular sample hole.

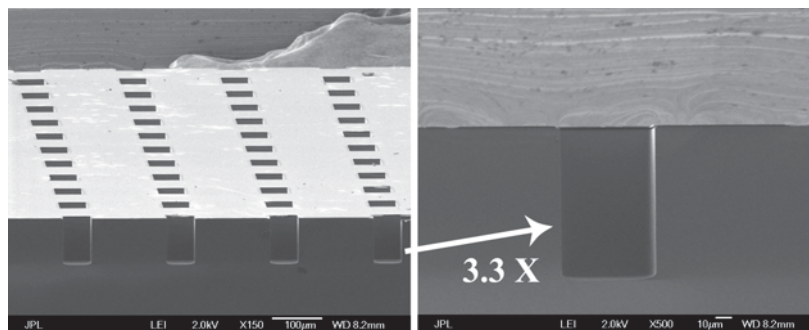


Figure 2.28: SEM image of sample and radiofrequency coil support. Image courtesy of Choonsup Lee.

## 2.7 Sample Transport

We have yet to discuss how micron-sized samples will be placed into the BOOMERANG spectrometer. Handling of these samples and placing them into the sample hole shown in Figure 2.28 by hand is relatively primitive and risks damage to the spectrometer. What we really seek, is an automated method of sample delivery that will shuttle samples in and out of the detection region with the possibility of moving the sample several diameters away during the NMR evolution period to improve the homogeneity and then back again for detection. A method that takes advantage of the microfabricated devices is to incorporate a microfluidic architecture into the spectrometer.

Microfluidics has seen an explosive growth in recent years and rather intricate circuitry can be readily designed, even allowing fine control of chemical reactions and mixing in pre-defined reactors. The primary material that has been used for microfluidic channel assembly is poly-dimethylsiloxane (PDMS). PDMS offers tremendous flexibility in design as well, is low-cost, and is rather chemically inert, but its substantial proton and carbon spin density makes it incompatible with  $^1\text{H}$  and  $^{13}\text{C}$  NMR spectroscopy. We will now outline methods to include silicon-based microfluidics.

This approach will mirror recent developments in piezoelectric microvalves integrated with silicon microfluidics.[52, 53, 54, 55] We see a cross-section of such a device in Figure 2.29. The diameter of the channel is  $40\ \mu\text{m}$  and the length is  $120\ \mu\text{m}$ . The sample channel has a piezoelectrically controlled microvalve on the left that lets fluid in initially. As a sample passes through it may be contained if the pair of microvalves on the left hand side

are closed or it may be selectively released and then reintroduced to allow NMR evolution to occur in a more homogeneous field.

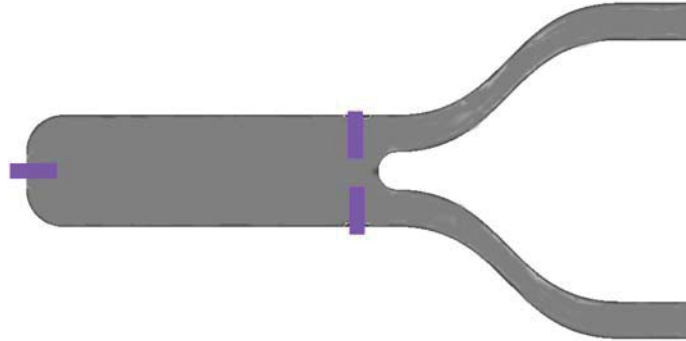


Figure 2.29: Cross-section of silicon microfluidic channel. There are three piezoelectrically controlled microvalves indicated in purple. On the right hand side, the two narrow channels allow samples to leave and reenter or to allow multiple samples to enter allowing study of chemical reactions.

The fluid flow was modeled<sup>4</sup> using the Navier-Stokes equations

$$\rho \frac{\partial \mathbf{u}}{\partial t} - \nabla \cdot \eta \left( \nabla \mathbf{u} + (\nabla \mathbf{u})^T \right) + \rho (\mathbf{u} \cdot \nabla) \mathbf{u} + \nabla p = 0 \quad (2.46)$$

$$\nabla \cdot \mathbf{u} = 0 \quad (2.47)$$

where  $\rho$  is the fluid density,  $\mathbf{u}$  is the velocity vector,  $\eta$  is the viscosity, and  $p$  is the pressure.[56] The fluid used in these simulations was water, with viscosity  $1 \times 10^{-3}$  Pa/s. The movement of the valve is described by  $pin$  which returns the value of one in the area corresponding to the valve pin and zero elsewhere. The actuation of the valve is given by

$$pin = x_{pin} y_{pin} \quad (2.48)$$

which is the cross-sectional area of the valve where

$$x_{pin} = (x > x_0) (x < x_1) \quad (2.49)$$

<sup>4</sup>The simulation was conducted using the fluidic mechanics component of ANSYS software, <http://www.ansys.com>, Canonsburg, PA. I would like to thank the Gharib group at Caltech for generous use of their software and workstations.

$$y_{pin} = 1 - (y > y_1) + (y > y_2) \quad (2.50)$$

where  $y_1$  and  $y_2$  depend on time  $t$  according to

$$y_1 = -y_0 + y_{max} \sin(2\pi t) \quad (2.51)$$

$$y_2 = y_0 + y_{max} \sin(2\pi t) \quad (2.52)$$

and where  $y_0$ ,  $x_0$ ,  $x_1$ , and  $y_{max}$  are fixed in time and describe the size of the valve pin and amplitude with which the pin moves.

At the inlet, the model uses fully developed laminar flow. The velocity is set to a parabolic profile with maximum velocity  $v_{max}$ . At the outlets, a neutral boundary condition states that the normal component of the stress tensor is zero:

$$\mathbf{n} \cdot \left[ -p\mathbf{I} + \eta(\nabla\mathbf{u}) + (\nabla\mathbf{u})^T \right] = 0 \quad (2.53)$$

and all other boundaries have condition  $\mathbf{u}=0$ .<sup>[56]</sup> The simulation of water transport through the channel is shown in Figure 2.30. In this simulation we consider the a model for a chemical reaction in which a reactant is introduced at time zero and then at a time of 100 ms a second reactant is added. We have assumed that the reaction is complete after 250 ms and that after this time the reaction mixture leaves the analysis area. At all times strictly laminar flow was observed with a maximum Reynolds number of 10.64. This simulation suggests that sample transport out of the detection area into a region of high magnetic field homogeneity and transport back for detection is feasible on time scales that compare with expected detector ringdown times, 80 ms-1 s.

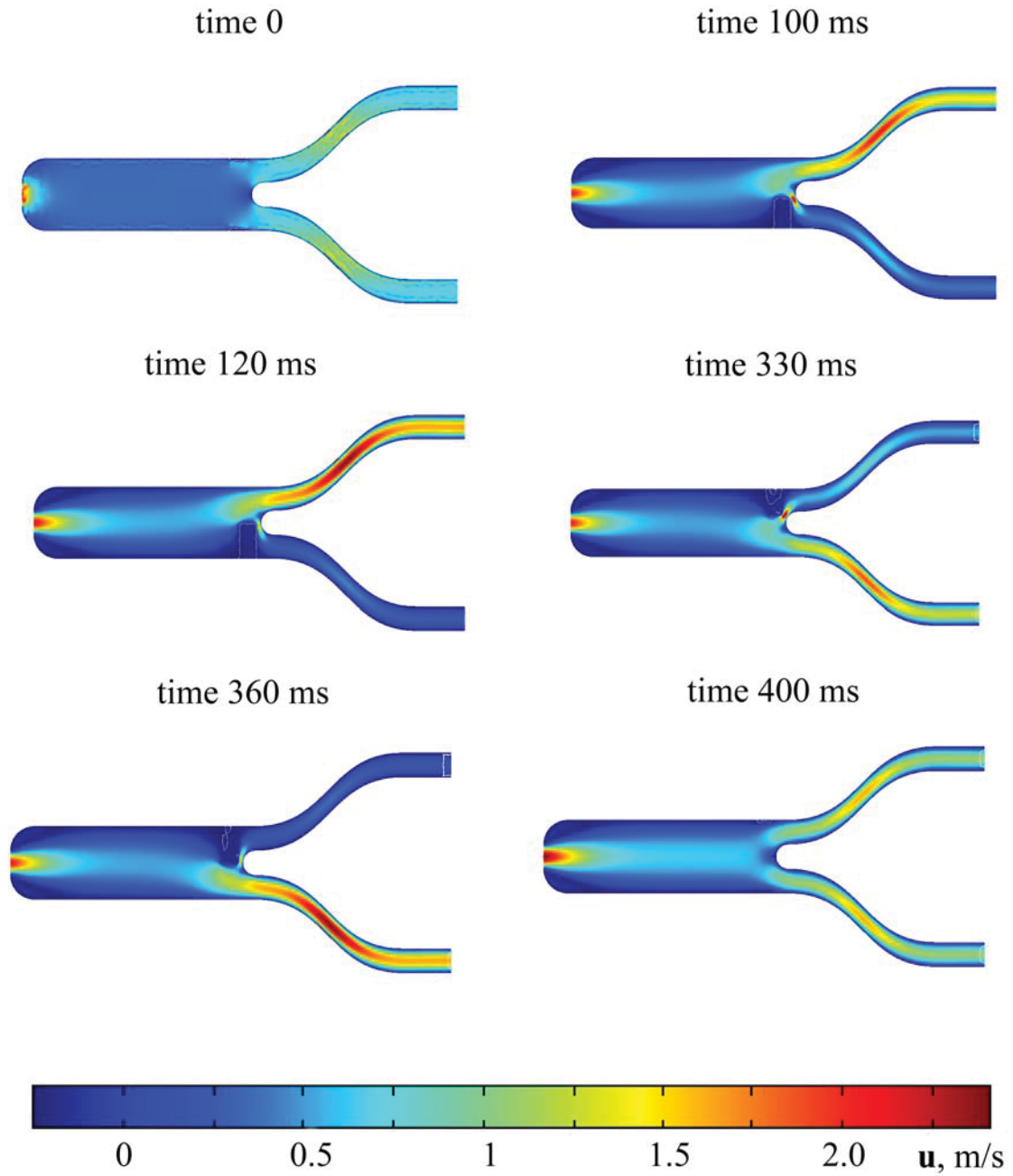


Figure 2.30: Simulation of Navier-Stokes equations in a silicon microfluidic channel with piezoelectric microvalves. The contour plots show the velocity field  $\mathbf{u}$  in m/s.

## 2.8 Detection of Oscillator Motion

### 2.8.1 Transverse Fiber-optic Interferometry

Fiber-optic interferometry (FOI) is a versatile method for displacement sensing of both micro- and macro-scale objects. One of the strongest motivations for using FOI for displacement sensing is its excellent sensitivity,  $\sim 0.1 \text{ pm}/\sqrt{\text{Hz}}$  [57], with large dynamic range. We will begin by discussing the theory of interferometric detection of oscillator motion.

The FOI consists of a laser (Sharp LT023 diode,  $\lambda = 780 \text{ nm}$ ), directional coupler (50/50, Gould Electronics), and photodiode detector (ThorLabs FDS010, Si, 9 V reverse-biased). The directional coupler delivers light from the laser to the sensing fiber and photodetector. The interference signal is formed between light reflected from a cleave at the end of the sensing fiber and light reflecting from the oscillator and re-entering the fiber. The light is directed through the coupler to the photodiode for detection. The circuit controlling the laser was adopted from [58] and is shown in Figure 2.31.

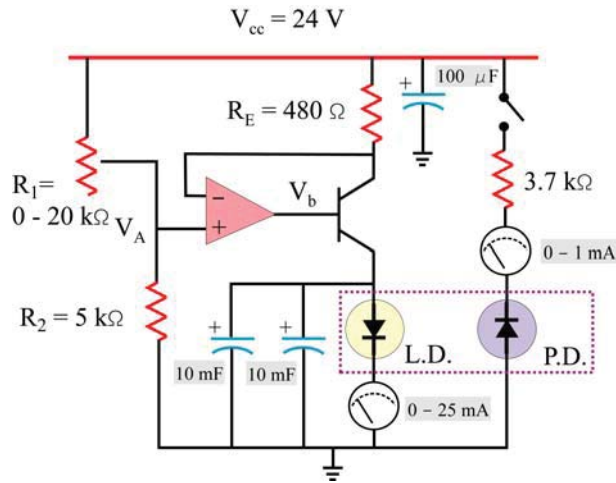


Figure 2.31: Constant current controller for Sharp LT023 laser diode.

The optical power emitted from the four fiber leads can be calculated from optical parameters. If the laser couples optical power  $P_f$  into the interferometer, and the directional coupler has power splitting ratio  $\frac{C_d}{C_s}$ , then the optical power delivered to the beam dump is  $P_f C_d$  and the power directed into the signal arm fiber is  $P_f C_s$ . The beam dump consists of a bare fiber end immersed in index of refraction matched fluid to stop reflected light from re-entering the coupler. At the end of the signal arm fiber, a fraction of the power

$R_{sig}$  is reflected back towards the coupler and has an amplitude dependence on the interference between a reflection from the cleaved fiber end  $R_{cl}$ . The amplitude changes as the fiber-to-oscillator spacing  $z$  changes. The optical power directed into the photodetector is  $P_f C_s C_d R_{sig}$  and the power reflected back into the laser is  $P_f C_d^2 R_{sig}$ . The light reflected back into the fiber is eliminated by using an optical isolator. These parameters along with the working circuitry of the interferometer used in experiments are displayed in Figure 2.32.

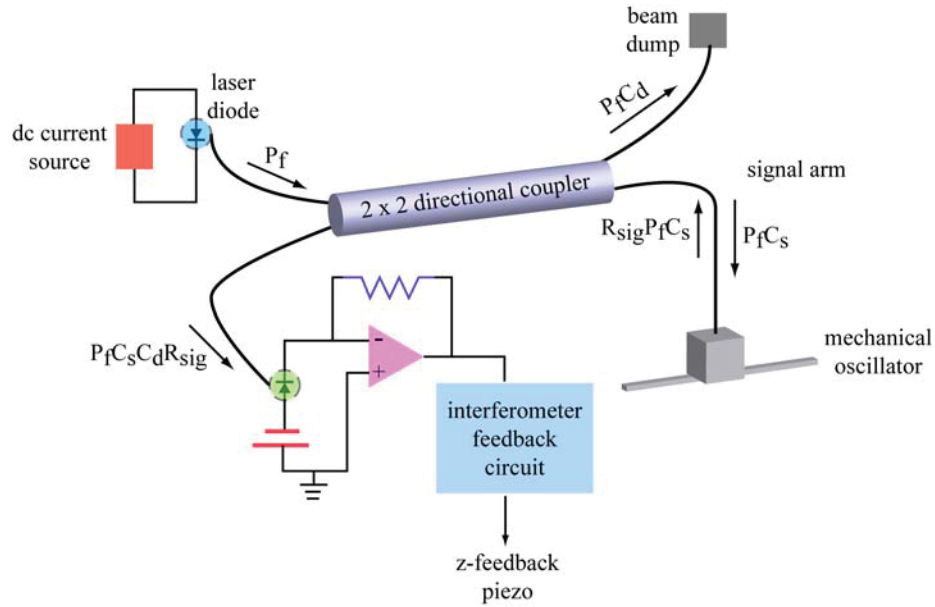


Figure 2.32: Schematic diagram indicating pathway, detection, and optical power of laser light in the fiber-optic interferometer.

For an optical fiber in vacuum, the reflectance at the fiber cleave is

$$R_{fc} = \left( \frac{n_{fib} - 1}{n_{fib} + 1} \right)^2 \quad (2.54)$$

where  $n_{fib}$  is the fiber core index of refraction. The oscillator reflection  $R_o$  is similar in magnitude. The optical amplitudes reflecting from these surfaces combine with a phase shift  $\phi(z)$  of  $4\pi$  radians for each wavelength  $\lambda$  of separation, and an additional shift of  $\pi$  occurs when light in a medium of low refractive index reflects from a surface of higher index of refraction

$$\varphi(z) = \pi + \frac{4\pi z}{\lambda}. \quad (2.55)$$

Thus, the resultant signal reflection is

$$\begin{aligned} R_{sig} &= \left( R_{fc}^{1/2} + R_{cl}^{1/2} e^{i\phi(x)} \right) \left( R_{fc}^{1/2} + R_{cl}^{1/2} e^{-i\phi(x)} \right) \\ &= R_{fc} + R_{cl} - 2\sqrt{R_{fc}R_{cl}} \cos(4\pi z/\lambda). \end{aligned} \quad (2.56)$$

The optical power that reaches the photodiode is then

$$\begin{aligned} P_{out} &= P_f R_{pd} C_s C_d \left( R_{fc} + R_{cl} - 2\sqrt{R_{fc}R_{cl}} \cos(4\pi z/\lambda) \right) \\ &= P_o \left( 1 - \bar{V} \cos(4\pi z/\lambda) \right) \end{aligned} \quad (2.57)$$

where  $R_{pd}$  is the power loss between the fiber and photodiode,  $P_o$  is the average output power, and  $\bar{V}$  is the fringe visibility

$$\bar{V} = \frac{\sqrt{R_{fc}R_{cl}}}{R_{fc} + R_{cl}}. \quad (2.58)$$

The interferometer is most sensitive to position changes at the center of a fringe, when  $4\pi z_0/\lambda = (2n + 1)\pi/2$ , or fringe center position  $z_0 = (2n + 1)\lambda/8$ , where  $n$  is an integer. Expanding  $P_{out}$  in a Fourier series for small deviations from the setpoint  $\Delta z_0$ , the interferometer output is

$$\frac{\Delta z}{P_{out}} = \frac{\lambda}{4\pi\bar{V}P_o}. \quad (2.59)$$

The signals observed during experiments are voltages and the maximum  $V_{\max}$  and minimum  $V_{\min}$  amplitudes of the interference signal may be used to define the fringe visibility as

$$\bar{V} = \frac{V_{\max} - V_{\min}}{V_{\max} + V_{\min}}. \quad (2.60)$$

This is shown in Figure 2.33.

Typical optical fibers have cladding diameters of 125  $\mu\text{m}$ , over two times the diameter of the detector magnet. If the fiber-optic interferometer were to operate in its normal longitudinal arrangement, where the fiber core sits directly above the measured oscillator, the hole required through the static field magnets would impart a severe reduction in magnetic field strength and would introduce large field inhomogeneity across the sample.

An alternative is to cleave the end of the fiber at 45° such that the fiber axis is parallel to

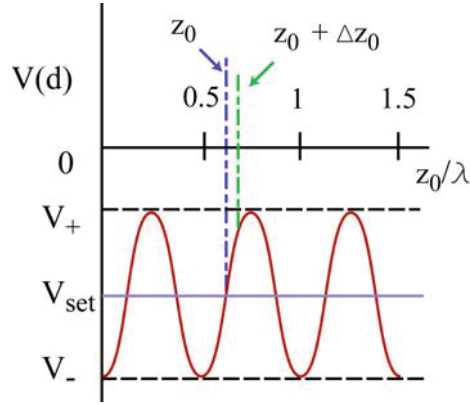


Figure 2.33: Interference waveform of the voltage output of the transimpedance amplifier as a function of  $z_0/\lambda$ .

the annular and detector magnets and the long axis of the oscillator. In this arrangement, we have a transverse, fiber-optic interferometer, TFOI. A Fabry-Perot cavity is formed between the cladding-air interface and the surface of the mechanical oscillator as shown in Figure 2.35. The guided wave in the fiber core is confined by the  $45^\circ$  cleave by total-internal-reflection and exits the fiber through its short axis. The fibers used in our experiments were either purchased from Oz Optics, Inc. or polished in our laboratory. Our polishing procedure is outlined as follows. First, the polyacrylate coating on the cladding was stripped by soaking the fiber end in acetone. The stripped fiber end was then placed through a stainless steel cylinder whose center was tapped with  $400\ \mu\text{m}$  diameter bore and whose face was machined at  $45^\circ$  such that  $\sim 500\ \mu\text{m}$  of fiber penetrated through the end of the bore. The fiber was then fixed into the bore by thermoset glue, Crystalbond<sup>®</sup>. The end of the fiber was scored with a diamond scribe and pressure on the fiber at the Crystalbond<sup>®</sup>-stainless steel interface was applied to provide the  $45^\circ$  cleave. The Crystalbond<sup>®</sup>-fiber end was then iteratively polished with emory paper and fiber polishing paper (ThorLabs, Inc.) down to  $0.1\ \mu\text{m}$  roughness. An optical microscope image of the fiber end is shown in Figure 2.34.

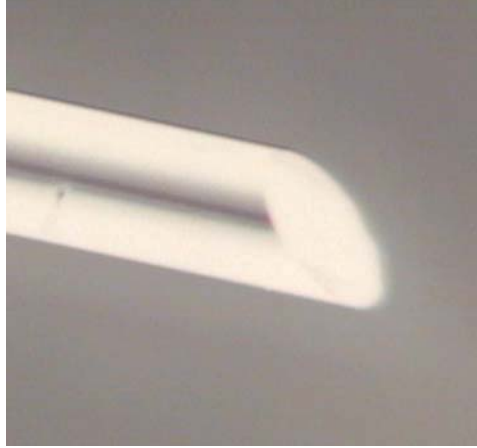


Figure 2.34: Optical microscope image of 45° cleaved, 125  $\mu\text{m}$  diameter fiber.

We may assume that the light exits through a plano-concave lens and this leads to a focal distance of

$$f = \frac{R_{cur}}{n - 1}$$

where  $R_{cur}$  is the radius of curvature and  $n$  is the index of refraction.  $R_{cur}$  is taken to be the core-cladding radius and  $n$  for the cladding at  $\lambda = 780 \text{ nm}$  is 1.4967, the index of refraction of the cladding is 1.5002.<sup>5</sup> Therefore, we calculate  $f$  to be 126  $\mu\text{m}$ . Experimentally, we find  $f$  to be 108  $\mu\text{m}$  from the center of the core, or an Fabry-Perot cavity size of 45  $\mu\text{m}$ . This was measured by placing the fiber directly on the measured surface, establishing a zero distance, and then adjusting the distance separation such that the amplitude of the interference fringe was maximized. During this measurement, the fiber was placed on a translation/goniometer stage controlled by micrometer actuation. Fine control and active feedback on the interferometer position (vide infra) of the positioning was accomplished by incorporation of a piezoelectric actuator. The goniometer served the purpose of adjusting the angle of the face of the cleaved fiber face with the surface of the mechanical oscillator. It should be noted that this experimental measurement is subject to some error in establishing the correct zero, due to monitoring the fiber being flush with the surface by eye. Furthermore, during the polishing process, it is possible the surface roughness at both the cleaved end and the exit end of the fiber are causing aberrations in the lens. It is suggested that after the polishing the fiber is sonicated in Syton®HT-50, a colloidal suspension of

<sup>5</sup>Oz Optics, Ontario, Canada. <http://www.ozoptics.com>

40 nm-sized silica particles.

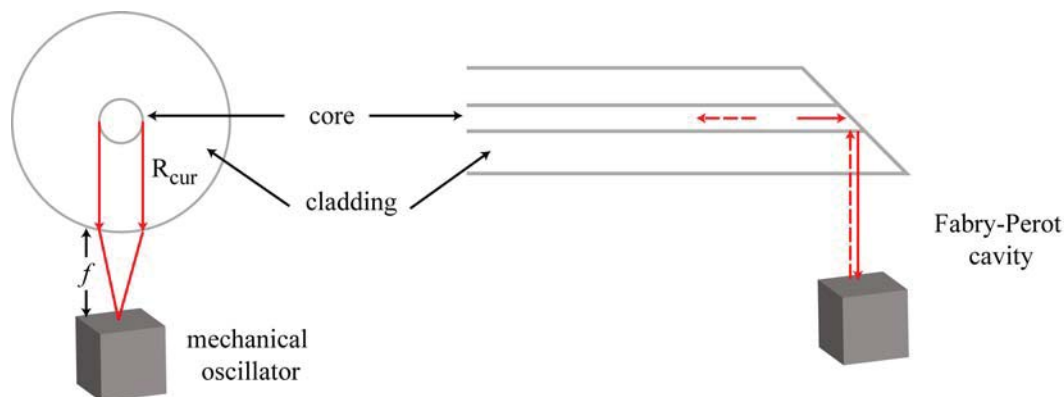


Figure 2.35: Transverse fiber-optic interferometer. A  $45^\circ$  polish at the fiber end causes light to be launched perpendicular to the fiber axis by total internal reflection. On the left, the longitudinal cross-section of the fiber is shown defining the radius of curvature  $R_c$  and the focal distance  $f$ . On the right, the transverse cross-section is shown where the Fabry-Perot cavity is defined by the cladding-air interface and the surface of the mechanical oscillator. The reflected light is shown as a dotted line. In both cases, the size of the core has been magnified by a factor of five for clarity.

We have also characterized the fringe visibility for the TFOI. Initial attempts to measure  $\bar{V}$  on silicon surfaces was not promising, where the optimum fringe visibility was found to be 4%. Acceptable fringe visibilities for locking (vide infra) on an interference fringe are greater than 10%. An identical experiment was performed with 200 nm of gold evaporated on a silicon substrate and showed an improvement of almost an order of magnitude in fringe visibility, 38%. This is presumably due the superior reflectivity of gold over silicon. Therefore, it is advisable to include gold on the buttress surface.

The fringe visibility measurements were performed by maximizing signal with respect to the goniometer angle to account for alignment issues of the fiber and oscillator. The oscillator was also mounted on a tilt stage to further correct for these issues. There is acceptable tolerance in the  $z$  positioning of the fiber: a working range of  $45 \mu\text{m} \pm 17 \mu\text{m}$  was found, where the lower and upper limits are referenced to  $\bar{V} = 10\%$ . This does require that a notch be etched in the silicon support to accommodate positioning of the fiber.

The angle sensitivity of the TFOI was also measured. The goniometer-mounted fiber was swept through angles of  $\pm 20^\circ$ . At each angular measurement, the height of the Fabry-Perot cavity was modulated to find the maximum fringe visibility. These results are shown

in Figure 2.36. We observed that the TFOI has an angular sensitivity of  $\pm 4^\circ$ . While we have used the fringe visibility as a measure of the practicality of the fiber-optic interferometer as a displacement sensor, its sensitivity actually depends upon the balance between shot noise and photon pressure noise.[11, 59] These noise sources will be quantified in the next section, but we will state here that they are insignificant compared to the thermal motion of the oscillator.

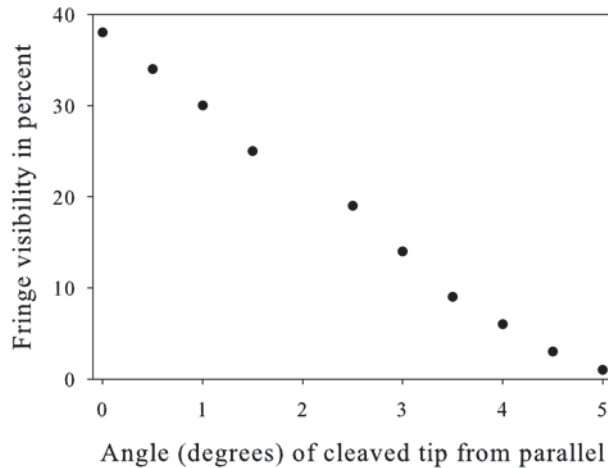


Figure 2.36: Angle sensitivity of the TFOI. Only positive angular deviations are shown due to the symmetry of the plot.

To correct for thermal drift and rf heating (drifts of  $\sim 1 \mu\text{m}$ ) we have incorporated a fiber position feedback circuit. Since the interferometer is most sensitive in its linear regime,  $V_{set}$  (Figure 2.33), active feedback on the fiber-oscillator gap is necessary. This is accomplished using the circuit shown in Figure 2.37.[58]  $V_{set}$  is controlled by a potentiometer and is sent through a voltage follower. The output of the transimpedance amplifier  $V_{pd}$  is sent through a second voltage follower and these signals are combined and sent to a differential amplifier. This error signal is then sent to an integrator via a single pole double throw (SPDT) switch which allows manual adjustments to be made with damage to the circuit. When the SPDT is off  $C_{int}$  is shorted and the output of the integrator is sent to ground. When the fringe has become “locked”, the output of the integrator, which is scaled by  $-(R_{int}C_{int})^{-1}$ , is amplified by  $\frac{R_1+R_2}{R_1}$  and an offset voltage  $V_{offset}$  is added to the amplified signal via the adder and is subtracted by the inverting amplifier whose output voltage

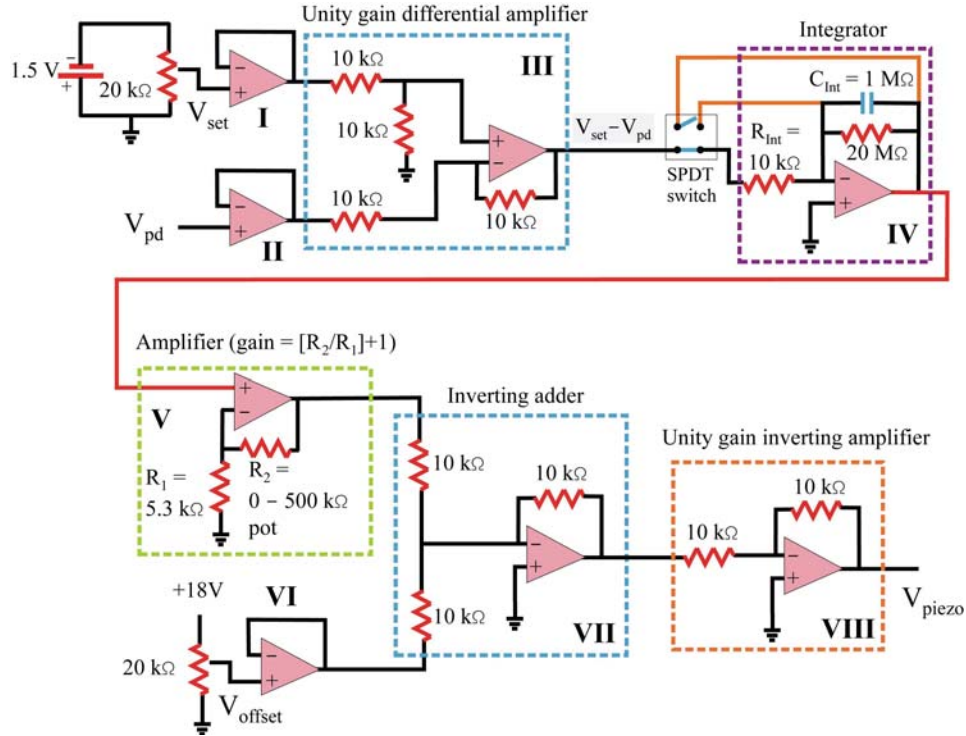


Figure 2.37: Feedback circuit for locking the interferometer to the sensitive portion of the interference waveform. All voltages shown were provided by dc power sources to minimize electrical noise.

is sent to the piezoelectric. If during experimental observations  $\Delta z_0 > 0$ , the error signal has a negative polarity and the output of the integrator **V** creates a positive voltage, which becomes amplified, expanding the piezoelectric. The opposite is true for  $\Delta z_0 < 0$ .

While in this configuration, the TFOI will be functional, it may be worthwhile to consider the following modification. Recently, it was reported that a cylindrical lens could be fabricated onto a optical fiber.[60] If the radius of curvature of the lens could be lengthened or if it was possible to design the lens with a low refractive index material which did not significantly distort the path of the light, the working distance could be improved. Alternatively, by fabricating a spherical mirror into the buttress, the focal distance may be increased to many times that shown in Figure 2.35. A spherical concave mirror has a focal distance given by

$$f = \frac{R_{cur}}{2} \quad (2.61)$$

where  $R_{cur}$  is the radius of curvature.  $R_{cur}$  is given by

$$R_{cur} = \frac{r^2 + h_m^2}{2h_m} \quad (2.62)$$

where  $r$  is the mirror radius and  $h_m$  is the the concavity depth as shown in Figure ?? . The mirror may be created in the buttress by selective etching if an appropriate photoresist mask is placed on top of the buttress. We can solve equation 2.62 for  $h_m$  and find that

$$h_m(R_{cur}, r) = R_{cur} - R_{cur} \sqrt{1 - \frac{r^2}{R_{cur}^2}}. \quad (2.63)$$

A focal distance of  $220 \mu\text{m}$  would remove the necessity for the etched notch, and this sets  $R_{cur}$  at  $440 \mu\text{m}$ . If we let  $r$  be  $20 \mu\text{m}$ , this sets  $h$  at  $0.5 \mu\text{m}$  which should be attainable using LIGA.[61, 62, 63]

## 2.8.2 Other Displacement Sensing Methods

Louis Madsen provided a comprehensive review of other sensing methods in his Ph.D. thesis. [30] These include piezoresistive [64] and capacitive [65] sensors which could be batch fabricated directly onto our spectrometer. Capacitive sensing may have the required noise floor, but as was previously mentioned due to charge counting statistics, their utility is limited at reduced size scales. A recent report of piezoelectric transducers [66] is exciting in light of its sensitivity and ability to allow multiplexed detection of multiple devices; which at present is not possible with fiber-optic interferometry. The sensor developed in the Roukes lab allows for detection of thermomechanical noise and can be used on devices with resonance frequencies as high as 71 MHz.

## 2.9 System Noise Analysis

The noise in the prototype spectrometer optimized for 3mm samples was considered by Leskowitz.[18] We will reinvestigate it here to compare the sources of noise in the  $50 \mu\text{m}$  spectrometer to the Brownian motion of the oscillator. The noise in oscillator may be characterized by the noise in the driving force whose rms fluctuation is given by

$$F_{z,rms} = \sqrt{4k_B T \alpha \Delta\nu} \quad (2.64)$$

with square-root force-noise spectral density  $S_F^{1/2} = \sqrt{4k_B T \alpha}$ . The NMR spectra will be recorded pointwise, where  $T_{1a} \gg \tau_h$ , such that  $\Delta\nu \ll \frac{1}{4\tau_h}$ . Thus, the oscillator is approximately in steady-state during driving. We may then express a square-root displacement-noise spectral density as

$$S_x^{1/2} = \frac{Q_h}{m\omega_h^2} \sqrt{4k_B T \alpha} = \sqrt{\frac{4k_B T}{m\omega_h^2 \gamma}} \quad (2.65)$$

recalling that  $\gamma = \frac{\omega_h}{Q}$  is the total damping parameter. If we assume a motional mass  $m$  of  $3.12 \times 10^{-13}$  kg, a frequency  $\frac{\omega_h}{2\pi}$  of 1 kHz, and a damping of 5.0 Hz we find that  $S_x^{1/2} = 6.5 \text{ nm}/\sqrt{\text{Hz}}$ . Each source of noise will then be compared to this value and will be appropriately converted to a square-root displacement-noise spectral density by the parameters shown in Figure A.6.

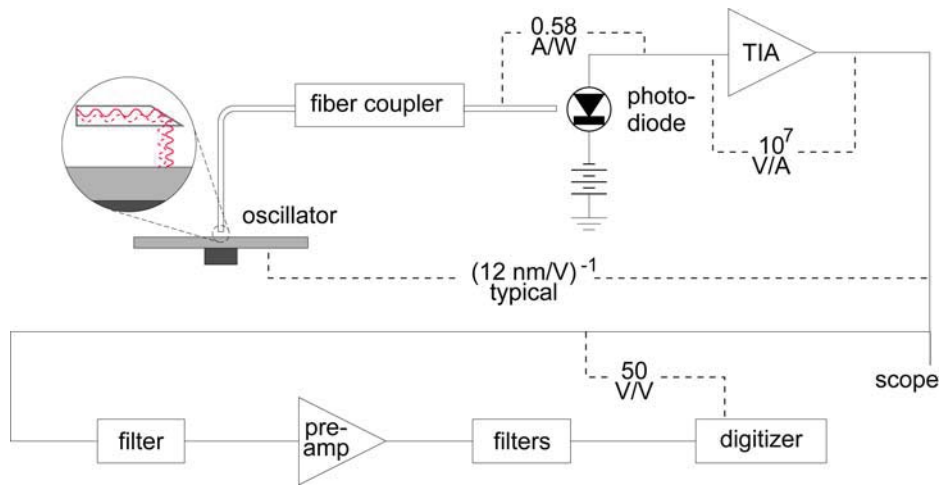


Figure 2.38: Signal conditioning path. The selected gain factors are shown for important connections in the signal path. TIA stands for transimpedance amplifier and converts a current to a voltage. The photodiode has a responsivity of  $0.58 \frac{\text{A}}{\text{W}}$ , the transimpedance is  $10^7 \Omega$ , and the displacement sensitivity as observed experimentally is  $12 \frac{\text{nm}}{\text{V}}$ . The transverse fiber-optic interferometer is shown in the inset and the interfering wave is depicted as a dotted line.

The motion of the oscillator is detected interferometrically, and as such two sources of noise are introduced: photon shot noise and photon pressure noise. Photon shot noise is due to Poisson statistics of independent light arrivals from the laser field.[67] For an optical power  $P$  incident on the photodiode, the number of photons  $N$  arriving on average is given by  $P\Delta t/\hbar\omega_p$ , where  $\Delta t$  is a given time interval and  $\hbar\omega_p$  is the energy of the photons. The

rms fluctuations is then given by

$$P_{rms} = \frac{\hbar\omega_p}{\Delta t} \sqrt{N} = \sqrt{2P\hbar\omega_p\Delta\nu} \quad (2.66)$$

where  $\Delta\nu = \frac{1}{2\Delta t}$ . The corresponding square-root noise spectral density is

$$S_{\hbar\omega_p}^{1/2} = \sqrt{2P\hbar\omega_p} \quad (2.67)$$

and with  $P = 1.6 \mu\text{W}$  and for  $\lambda = 780 \text{ nm}$ , this gives  $S_{\hbar\omega}^{1/2} = 597 \text{ fW}/\sqrt{\text{Hz}}$ . This may be converted to a displacement-noise by

$$597 \frac{\text{fW}}{\sqrt{\text{Hz}}} \times 0.58 \frac{\text{A}}{\text{W}} \times 10^7 \frac{\text{V}}{\text{A}} \times 12 \frac{\text{nm}}{\text{V}}$$

giving  $S_{x,\hbar\omega}^{1/2} = 64 \text{ fm}/\sqrt{\text{Hz}}$ . The displacement sensitivity of  $12 \frac{\text{nm}}{\text{V}}$  as shown in Figure A.6 relates the oscillator displacement to the observed voltage at the TIA. The trough-to-crest difference  $\Delta V$  in the interference fringe corresponds to a displacement of  $\frac{\lambda}{4}$ . The displacement sensitivity is then  $\frac{2}{\pi} \frac{\lambda/4}{\Delta V}$ .

Poisson statistics of the laser radiation also results in fluctuations in the radiation pressure.[68] If we assume that a single photon transfers a momentum  $2\hbar\omega_p/c$  to the oscillator and similarly have rms fluctuations  $\sqrt{N}$  in the number of photons, the rms fluctuations in the transferred momentum is

$$p_{rms} = \frac{2\hbar\omega_p}{c} \sqrt{N} = \sqrt{\frac{4P\hbar\omega_p\Delta t}{c^2}}. \quad (2.68)$$

This can be thought of inducing a random force  $F_p = \frac{p_{rms}}{\Delta t}$  which has a square-root spectral density

$$S_{F,\hbar k}^{1/2} = \sqrt{\frac{8P\hbar\omega_p}{c^2}} \quad (2.69)$$

with displacement-noise square-root spectral density

$$S_{x,\hbar k}^{1/2} = \frac{1}{m\omega_h\gamma} \sqrt{\frac{8P\hbar\omega_p}{c^2}}. \quad (2.70)$$

For our proposed device this gives  $S_{x,\hbar k}^{1/2} = 95 \text{ fm}/\sqrt{\text{Hz}}$ .

We now consider the noise in the elements along the signal conditioning path. The

photocurrent in the photodiode has a distinct associated shot noise. For a dc current  $I$  the square-root of the noise spectral density is

$$S_i^{1/2} = \sqrt{2Ie} \quad (2.71)$$

where  $e$  is the electron charge. We may assume that the photocurrents ( $\sim 1 \mu\text{A}$ ) in the MEMS experiments will be comparable to those in the millimeter-scale spectrometer and may calculate the square-root displacement-noise spectral density by multiplying equation 2.71 by the transimpedance and displacement sensitivity giving  $S_{x,i}^{1/2} = 68 \text{ fm}/\sqrt{\text{Hz}}$ . The transimpedance amplifier<sup>6</sup> converts the photocurrent to a voltage by use of a resistor which dominates the noise in the instrument. The square-root voltage-noise spectral density associated with the Johnson noise of the resistor with resistance  $R$  is

$$S_\Omega^{1/2} = \sqrt{4k_BTR} \quad (2.72)$$

and for  $R = 10^7 \Omega$ , this is  $S_\Omega^{1/2} = 400 \text{ nV}/\sqrt{\text{Hz}}$ . Similarly, we find that  $S_{x,\Omega}^{1/2} = 4.8 \text{ fm}/\sqrt{\text{Hz}}$ . The voltage noise at the input to the preamplifier<sup>7</sup> is given to be  $S_E^{1/2} = 1.5 \text{ nV}/\sqrt{\text{Hz}}$ , thus  $S_{x,E}^{1/2} = 0.0018 \text{ fm}/\sqrt{\text{Hz}}$ . Finally we consider the effects of digitization of analog signals. For a step-size  $\varepsilon$ , noise will be added in the range  $\pm \frac{\varepsilon}{2}$  corresponding to an rms fluctuation of  $\frac{\varepsilon}{\sqrt{12}}$  in the bandwidth  $\Delta\nu = \frac{1}{2\Delta t}$  with sampling time  $\Delta t$ . The square-root voltage-noise spectral density is

$$S_D^{1/2} = \frac{\varepsilon}{\sqrt{12}} \sqrt{2\Delta t} = \varepsilon \sqrt{\frac{\Delta t}{6}}. \quad (2.73)$$

For current state-of the art 16-bit digitization boards<sup>8</sup>, with a full range of 2.5 V, this corresponds to a  $\varepsilon$  of  $\frac{2.5\text{V}}{2^{32}} = 38.1 \mu\text{V}$ . For samples acquired every  $1 \mu\text{s}$ ,  $S_D^{1/2} = 15.6 \text{ nV}/\sqrt{\text{Hz}}$  giving  $S_{x,D}^{1/2} = 0.019 \text{ fm}/\sqrt{\text{Hz}}$ .

Therefore, for the experiments planned with the MEMS spectrometer the predominant noise source will be the Brownian motion noise of the oscillator. All other sources of noise, even when sums of squares are considered  $S_{x,inst}^{1/2} = 133 \text{ fm}/\sqrt{\text{Hz}}$  are roughly four orders of magnitude smaller than  $S_x^{1/2}$ .

<sup>6</sup>Model 181 Current Sensitive Preamplifier manual (Princeton Applied Research Corporation, 1978).

<sup>7</sup>Model SR530 Lock-In Amplifier manual (Stanford Research Systems, 1989).

<sup>8</sup>See for example, NI PXI-6250 from National instruments, <http://www.ni.com>. This multichannel board operates at 1 Ms/s.

## 2.10 Microfabrication Overview and Results

The microfabrication results presented here were due to the efforts of a collaboration with the Microdevices Laboratory at the Jet Propulsion Laboratory. The essential steps in microfabrication of the spectrometer include photolithography to pattern well-defined structures on a substrate, selective etching of these patterned substrates, and electrodeposition to create the magnetic and radiofrequency excitation structures. Details on earlier iterations of the process can be found in the Ph.D. thesis of Louis Madsen and for a comprehensive review of all of the fabrication techniques employed consult the text of May and Sze.[69]

The process flow chart utilized to construct the devices is shown in Figure 2.40. Because magnetic and oscillator structures were to be defined on a monolithic wafer and since alignment of the magnets with the oscillator is crucial we used double-side alignment. For the  $3\ \mu\text{m}$  size gap, we are no longer restricted to use a contact aligner in which the photolithography mask is placed directly onto the substrate wafer. Contact aligners have  $\sim 1\ \mu\text{m}$  tolerance during double-side alignment and requires considerable amounts of time to create structures. A more direct method which meets our tolerance goals for wider gaps is a stepper motor. The wider gap also eliminates the use of on milling to remove the metallic seed layer between the detector and annulus and should lead to much higher device throughput.

It is useful at this point to list the limitations presented by the microfabrication process. First, the thickness of the oscillator beams is restricted be greater than  $2\ \mu\text{m}$  to avoid stiction. Stiction occurs when surface adhesion forces are higher than the mechanical restoring force of the microstructure. When a device is removed from the aqueous solution after wet etching of an underlying sacrificial layer, the liquid meniscus formed on hydrophilic surfaces pulls the microstructure towards the substrate and stiction occurs. There are new methods to reduce stiction effects that include passivating the surface with an organic coating which not only reduces capillary forces and direct chemical bonding, but also reduce electrostatic forces if the thin organic layer is directly applied to the semiconducting substrate, without the intervening oxide layer.[70, 71] A second limitation is that the maximum aspect ratio in photoresist molds is 10:1. The detector and annular magnets are deposited into photoresist molds patterned such that radial slits are created to minimize eddy current damping. For  $8\ \mu\text{m}$  tall magnets, the width of slits must be greater than  $0.8\ \mu\text{m}$ . Larger slit sizes

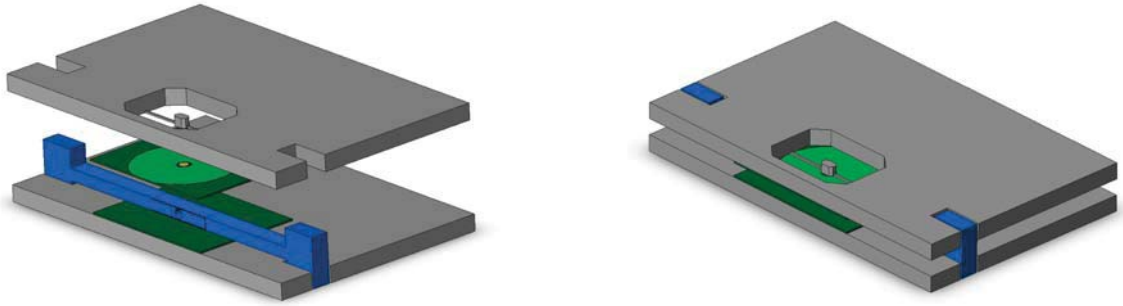


Figure 2.39: Proposed spectrometer assembly and arrangement. The optical fiber used for interferometry has been omitted for clarity.

both reduce detector sensitivity (removal of magnetic material) and homogeneity. A third limitation is internal stress in the magnetic film. As we have stated before, we require films with internal stresses lower than 80 MPa. Materials that typically have low-stress and large saturation magnetization such as iron or cobalt-iron alloys have poor corrosion resistance to buffered oxide etch (BOE). BOE primarily etches silicon preferentially, but due to long etch times, BOE diffuses into the magnet array and can degrade the magnetic material. This problem is dealt with by using beams with widths smaller than  $40\ \mu\text{m}$ .

We have eluded to how the spectrometer will be assembled. In addition to creating a stable structure to support the radiofrequency excitation coil, the I-beam shown in Figure 2.25 serves to align the two pieces of the spectrometer, the top piece containing the mechanical oscillator and magnetic assembly and the bottom piece containing the symmetric magnetic array. Additional I-beam-like structures may be necessary both in the front and the back of the spectrometer to give it improved structural rigidity.

The proposed spectrometer is shown schematically in Figure 2.39. With the aid of an optical microscope, the bottom half and I-beam may be secured into place by using a quick set epoxy resin. Similarly, the top piece and I-beam may be mated. The notch sizes should have a tolerance of no more than two microns to ensure reasonable alignment of the detector and sample.

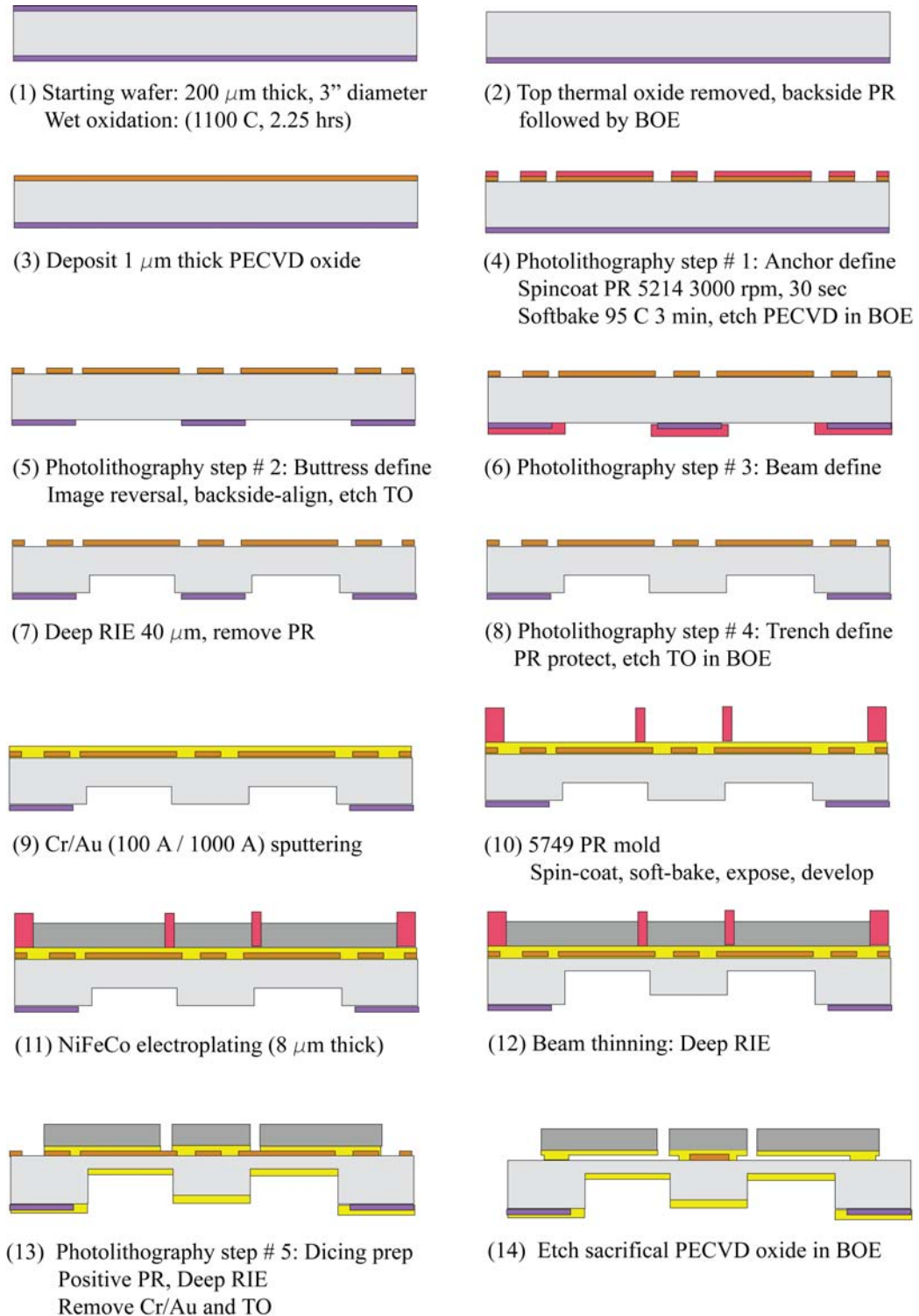


Figure 2.40: Microfabrication overview. There are five steps in the process that involve photolithography. PR stands for photoresist, BOE for buffered oxide etch, PECVD for plasma enhanced chemical vapor deposition, TO for thermal oxide, and RIE for reactive ion etch.

## 2.11 Parallel Analysis

The signal-to-noise assumptions we have considered so far are for a single detector. Given that our proposal is to use microfabrication methods to assemble a spectrometer, there is a potential to have order  $10^4$  detectors on a single wafer. If a sample is evenly distributed among these detectors there is an improvement in signal-to-noise over measuring the entire sample in one detector. Assuming that scale invariance of  $\tau_h$  holds and that each detector in the array is smaller by  $10^x$  than the single detector used to measure the entire sample, the sensitivity improvement is  $(10^4 \times 10^{-x})^{1/2}$ . A reasonable value of  $x$  for experiments is  $\frac{4}{3}$ , giving a SNR improvement of 22. Distributing a sample over inductive detectors leads to a decrease in SNR. Therefore, force-detection offers promise in both high-throughput spectroscopy and in combinatorial assays. This is shown schematically in Figure 2.41.

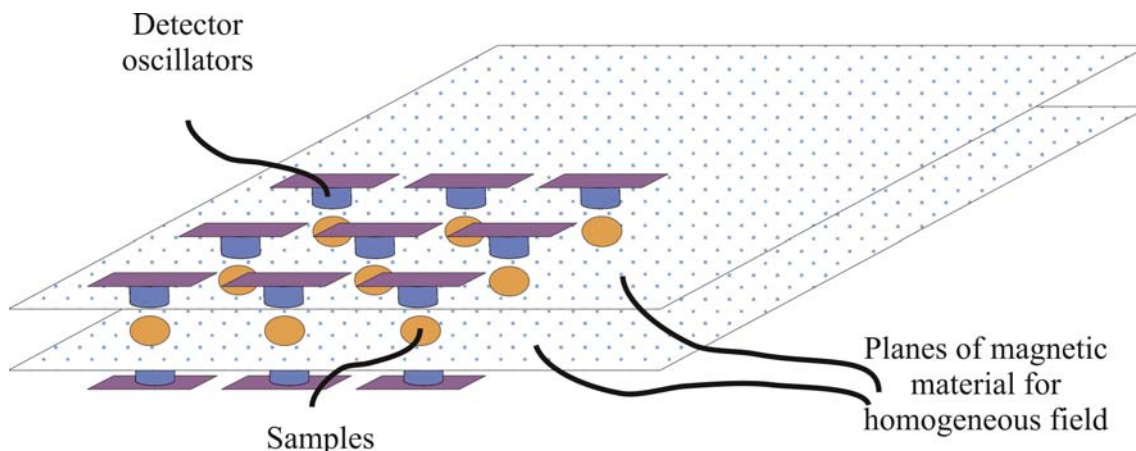


Figure 2.41: Massively parallel analysis with an array of BOOMERANG detectors.

## 2.12 Conclusions

In this chapter, we have provided a comprehensive study of the design issues relevant towards fabrication of a force-detected NMR spectrometer optimized for  $50 \mu\text{m}$  diameter samples. The use of finite element methods has facilitated the studies shown here and has provided many points of reference for the design of the silicon mechanical oscillator structures, the detector and annular magnet assembly, static-field magnets with focusing poles, incorporation of microfluidic channels to analyze liquid samples, and the design of radiofrequency excitation coils. Results from our microfabrication efforts were also shown, as well as

the fabrication procedure. We have successfully observed oscillation of silicon resonators with electroplated annular and ring magnets and are near completion of a full functional spectrometer.

Sources of damping in the experimental apparatus were rigorously considered and consistent with the observations from the millimeter-scale spectrometer built in our laboratory, eddy current damping was shown to be the predominant mechanism of loss. In addition to incorporation of radial slits in both the detector and annulus, we have shown that assembly of magnetic structures from packed nanoparticles should reduce this damping by roughly four orders of magnitude.

A new method of interferometric detection was demonstrated and we have suggested several modifications to improve its functioning and have considered new piezoelectric transducers that will assist in multiplexed and parallel analyses.

## Chapter 3

# Force-Detected $^{14}\text{N}$ Overtone NMR

### 3.1 Introduction

Traditional NMR experiments on nuclei with spin  $S \geq 1$  are complicated by quadrupolar induced broadening of the fundamental resonance through an interaction of the spins with surrounding electric field gradients. The resulting linewidths can span over several MHz, however excitation and detection bandwidths of pulsed NMR experiments are typically on the order of hundreds of kHz. As a result, the presence of a large quadrupolar coupling makes acquisition of a complete spectrum impossible without retuning of the spectrometer.

The application of solid-state NMR to the study of biological molecules is rapidly increasing and as a result the development of methods to exploit  $^{14}\text{N}$  and its 99.6% natural abundance while allowing for acquisition of high resolution spectra without spectrometer tuning would be of great interest.  $^{14}\text{N}$  is a spin-1 nucleus with two allowed Zeeman transitions with large first- and second-order quadrupolar interactions, as shown in Figure 3.1.

An analogy to optical spectroscopy that was applied to NMR is overtone spectroscopy.[72, 73, 74] In this approach weakly allowed transitions are directly excited and detected near multiples of the nuclear Larmor frequency. The size of the coupling, or mixing of spin states, determines the strength of the transition. For the case of integral spin quadrupolar nuclei, reduced spectral width is possible due to the invariance overtone transition frequencies to first order quadrupole splittings.

In this chapter we will present an introduction to overtone NMR, use an exact treatment of overtone NMR to compare the signal-to-noise ratios of force- and inductive-detection, and include simulations of force-detected NMR experiments on tholins and biological molecules.

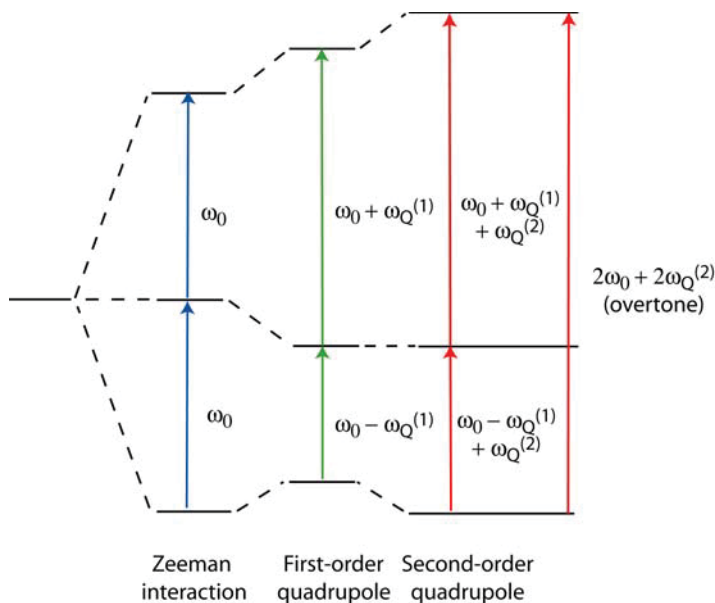


Figure 3.1: Spin energy level diagrams for  $^{14}\text{N}$  NMR. The traditional Zeeman interaction is observed in a static magnetic field with Larmor frequency  $\omega_0$ . The quadrupolar coupling splits the fundamental into a doublet with a splitting of  $2\omega_Q^{(1)}$ . For large quadrupolar couplings, a second-order shift  $\omega_Q^{(2)}$  is observed. Overtone transitions at  $2\omega_0 + 2\omega_Q^{(2)}$  become allowed and can be directly probed.

## 3.2 Theory

### 3.2.1 Coordinate Systems

Hamiltonians are typically created with an initial reference frame centered on the atom. We can think of the atomic frame as being the diagonal representation of the interaction. As soon as we move from this frame via some rotation, elements become mixed combinations of the atomic frame. This atomic frame is given the name Principle Axis System (PAS). In the PAS frame the arbitrary interaction in NMR can be reduced to three components. In the Cartesian frame these are typically given the labels  $\delta_x$ ,  $\delta_y$ , and  $\delta_z$  in the spherical frame they are given the labels  $\delta_{iso}$  (isotropic),  $\delta_{ani}$  (anisotropic) and  $\eta$  (asymmetry), and are related via

$$\delta_{iso} = \frac{\delta_x + \delta_y + \delta_z}{3} \quad (3.1)$$

$$\delta_{ani} = \delta_z \quad (3.2)$$

$$\eta = \frac{\delta_x - \delta_y}{\delta_z}$$

In the Cartesian interaction frame, PAS is given as

$$A_{car}^{PAS} = \begin{pmatrix} \delta_z & 0 & 0 \\ 0 & \delta_y & 0 \\ 0 & 0 & \delta_x \end{pmatrix}. \quad (3.3)$$

The spherical basis is reduced to a sum over the various rank  $l$  components as

$$A_{sph}^{PAS} = A_0 + A_1 + A_2 \quad (3.4)$$

$$A_{0,0} = -\sqrt{3}\delta_{iso} \quad (3.5)$$

$$A_{1,\pm 1} = A_{1,0} = 0 \quad (3.6)$$

$$A_{2,\pm 1} = 0, \quad A_{2,\pm 2} = \frac{1}{2}\delta_{ani}\eta, \quad A_{2,0} = \sqrt{\frac{3}{2}}\delta_{ani}. \quad (3.7)$$

Another relevant frame is the molecular frame, where the atoms are assumed to be fixed in space. This requires the definition of another axis system, in which rotations may be done either by a Cartesian Euler rotation or a spherical Wigner rotation as discussed in Chapter 1. The Euler angles used to perform this rotation will be called  $\Omega_{mol}$

$$A_{car}^{mol} = R(\Omega_{mol}) A_{car}^{PAS} R(\Omega_{mol})^{-1} \quad (3.8)$$

$$A_{sph}^{mol} = A_0^{PAS} + \sum_{m'=2}^2 D_{m,m'}(\Omega_{mol}) A_{l,m}^{PAS}. \quad (3.9)$$

### 3.2.2 Quadrupole Physics

The electrostatic energy from the charge distributions on a nucleus  $\rho_n(\mathbf{r}_n)$  to an electron  $\rho_e(\mathbf{r}_e)$  is given by [24]

$$E = \frac{1}{4\pi\epsilon_0} \int \int dr_n dr_e \frac{\rho_n(r_n) \rho_e(r_e)}{|\mathbf{r}_n - \mathbf{r}_e|} \quad (3.10)$$

and can be expressed in spherical coordinates by setting

$$\frac{1}{|\mathbf{r}_n - \mathbf{r}_e|} = 4\pi \sum_{l=0}^{\infty} \sum_{m=-l}^l \frac{1}{2l+1} \frac{r_n^l}{r_e^{l+1}} Y_l^{m*}(\theta_n, \theta_n) Y_l^m(\theta_e, \theta_e). \quad (3.11)$$

The energy can be reexpressed as

$$E = \sum_{l=0}^{\infty} \sum_{m=-l}^l A_l^m T_l^{m*}$$

where

$$A_l^m = \sqrt{\frac{4\pi}{2l+1}} \int dr_n \rho_n(r_n) r_n^l Y_l^m(\theta_n, \theta_n) \quad (3.12)$$

and

$$T_l^m = \frac{1}{4\pi\epsilon_0} \sqrt{\frac{4\pi}{2l+1}} \int dr_e \rho_e(r_e) r_e^{-(l+1)} Y_l^m(\theta_e, \theta_e). \quad (3.13)$$

The quantum mechanical picture is constructed by correspondence and gives

$$\rho_n(r_n) = \langle \Psi_n | \sum_{i=1}^A e_i \delta(r_n - R_i) | \Psi_n \rangle \quad (3.14)$$

where  $r_{e,n}$ ,  $Y_l^m$ , and  $\rho_{e,n}$  are operators and  $A_l^m$  and  $T_l^m$  are expectation values. A similar case holds for electrons.

The Hamiltonian is now expressed in terms of tensor operators

$$\mathcal{H} = \sum_{l=0}^{\infty} \sum_{m=-l}^l \mathbf{A}_{l,m} \mathbf{T}_{l,m}^\dagger = \sum_{l=0}^{\infty} \sum_{m=-l}^l (-1)^m \mathbf{A}_{l,m} \mathbf{T}_{l,-m} \quad (3.15)$$

where operators  $\mathbf{A}_{l,m}$  and  $\mathbf{T}_{l,-m}$  generate the corresponding expectation values.

The electric field gradients at a nucleus may be considered by using the principal axis system to describe both the spin and electric field gradient coordinates. The Hamiltonian becomes

$$\mathcal{H} = \frac{e^2 q Q}{4I(I-1)} \left\{ 3\mathbf{S}_z^2 - \mathbf{S}(\mathbf{S}+1) + \frac{1}{2}\eta(\mathbf{S}_+^2 + \mathbf{S}_-^2) \right\} \quad (3.16)$$

where  $\eta$  is the asymmetry parameter

$$\eta = \frac{|V_{xx} - V_{yy}|}{V_{zz}}. \quad (3.17)$$

### 3.2.3 Overtone NMR

For a quadrupolar nucleus of spin  $\mathbf{I}$ , the Hamiltonian is given by [74]

$$\mathcal{H}_Q = -\omega_0 \mathbf{S}_z + \omega_Q [3\mathbf{S}_{z'}^2 - \mathbf{S}^2 + \eta(\mathbf{S}_{x'}^2 - \mathbf{S}_{y'}^2)] \quad (3.18)$$

where the prime denotes the principal axis of the electric field gradient with quadrupolar coupling constant,  $\omega_0$  is the nuclear Larmor frequency and  $\omega_Q = \frac{e^2Q}{4S(2S-1)\hbar}$  where  $e$  is the electron charge,  $eQ$  is the nuclear quadrupole coupling constant, and  $\eta$  is the asymmetry parameter. The asymmetry parameter  $\eta$ , depends on the electronic environment of the nucleus as we saw above. The Hamiltonian may be transformed to the laboratory frame by rotations yielding

$$\mathcal{H}_Q = -\omega_0 \mathbf{S}_z + \omega_Q \left\{ \frac{\sqrt{6}}{2} (3 \cos^2 \beta - 1 + \eta (\cos 2\alpha \sin^2 \beta)) \mathbf{T}_0^2 + f \mathbf{T}_1^2 - f^* \mathbf{T}_{-1}^2 + g \mathbf{T}_2^2 + g^* \mathbf{T}_{-2}^2 \right\} \quad (3.19)$$

where  $f$  and  $g$  are functions of the Euler angles  $(\alpha, \beta, \gamma)$  which are used to relate the laboratory and principal axis coordinates:

$$f(\alpha, \beta, \gamma) = e^{i\gamma} [3 \sin \beta \cos \beta - \eta (\cos 2\alpha \sin \beta \cos \beta + i \sin 2\alpha \sin \beta)] \quad (3.20)$$

$$g(\alpha, \beta, \gamma) = e^{2i\gamma} \left[ \frac{3}{2} \sin^2 \beta + \eta \left( \frac{1}{2} (1 + \cos^2 \beta) \cos 2\alpha + i \sin 2\alpha \sin \beta \right) \right]. \quad (3.21)$$

$\mathbf{T}_m^2$  are the spherical rank tensor operators of rank two and component  $m$  and are expressible in terms of the spin operators as shown below.

Operator	Expression
$\mathbf{T}_0^2$	$\frac{1}{\sqrt{6}} (3I_z^2 - \mathbf{I}(\mathbf{I} + 1))$
$\mathbf{T}_{\pm 1}^2$	$\mp \frac{1}{2} (\mathbf{I}_z \mathbf{I}_{\pm} + \mathbf{I}_{\pm} \mathbf{I}_z)$
$\mathbf{T}_{\pm 2}^2$	$\frac{1}{2} \mathbf{I}_{\pm} \mathbf{I}_{\pm}$

Table 3.1: Spherical tensor operators.

In a high magnetic field, defined by  $\omega_0 \gg e^2Q/h$ ,  $\mathcal{H}_Q$  has  $2I + 1$  eigenstates, which are the  $|m\rangle$  eigenstates of  $\mathbf{I}_z$ . When the high field limit does not apply, the eigenstates are now linear superpositions

$$|\varphi_m\rangle = \sum_{m'=1}^1 C_{mm'} |m'\rangle \quad (3.22)$$

where  $C_{mm'}$  are the coupling coefficients.

The matrix elements of the operator  $\mathbf{S}(\hat{\mathbf{n}})$  determine the magnetic dipole transitions between two spin states, where  $\hat{\mathbf{n}}$  is a unit vector along the axis of the radiofrequency excitation coil and  $\mathbf{S}$  is the laboratory frame spin operator for the nucleus. The resulting

matrix elements  $\mathbf{S}_{1,-1}(\hat{\mathbf{n}})$  between two spin states  $|\varphi_1\rangle$  and  $|\varphi_{-1}\rangle$  is given by

$$\mathbf{S}_{1,-1}(\hat{\mathbf{n}}) = \langle \varphi_1 | \mathbf{S}(\hat{\mathbf{n}}) | \varphi_{-1} \rangle \quad (3.23)$$

where this double quantum transition is induced by irradiation at  $2\omega_0$ . This transition probability depends upon coupling coefficients between these two states  $C_{mm'}$ .

For an rf coil defined by polar angle  $\theta$  and azimuthal angle  $\phi$ , the coupling operator  $\mathbf{M}$  becomes

$$\mathbf{M} = (\sin \theta \cos \phi) \mathbf{S}_x + (\sin \theta \sin \phi) \mathbf{S}_y + (\cos \theta) \mathbf{S}_z. \quad (3.24)$$

For the overtone transition [74],

$$\begin{aligned} \langle \varphi_1 | \mathbf{M} | \varphi_{-1} \rangle &= \frac{\sqrt{2} \sin \theta \cos \phi}{2} [C_{-1,0} (C_{1,-1} + C_{1,1})^* + C_{1,0} (C_{-1,-1} + C_{-1,1})] \\ &+ \frac{i\sqrt{2} \sin \theta \sin \phi}{2} [C_{-1,0} (C_{1,-1} - C_{1,1})^* + C_{1,0}^* (C_{-1,1} - C_{-1,-1})] \\ &+ \cos \theta (C_{-1,1} C_{1,1}^* - C_{-1,-1} C_{1,-1}^*). \end{aligned} \quad (3.25)$$

These mixing coefficients were exactly solved by diagonalizing the Hamiltonian in equation 3.19 and will be used in the signal-to-noise analysis below.

### 3.3 Signal-to-Noise

In Chapter 1, we considered the signal-to-noise expressions of force and inductive detection. The case for force detection is given by

$$SNR_F = \frac{\kappa_F \mu_0^{\frac{1}{2}} (\langle \varphi_1 | \mathbf{S}_z | \varphi_1 \rangle - \langle \varphi_{-1} | \mathbf{S}_z | \varphi_{-1} \rangle) V_s M_s M_d}{R_{\max} \sqrt{8k_B T \alpha (\Delta\nu)}} \quad (3.26)$$

where the relevant parameters are described in Chapter 1. The matrix elements  $\langle \varphi_{\pm 1} | \mathbf{S}_z | \varphi_{\pm 1} \rangle$  arise from the fact that  $\mathbf{S}_z$  is usually not along the  $z$ -axis in the principal axis system of the electric field gradient tensor. For inductive detection the expression as derived in Tycko and Opella [74] becomes

$$SNR_I = \frac{\kappa_I \mu_0 V_s (|\langle \varphi_1 | \mathbf{I}_x | \varphi_{-1} \rangle|) M_s \omega_0}{R_{\max} \sqrt{8k_B T R (\Delta\nu)}} \quad (3.27)$$

$\langle \varphi_1 | \mathbf{M} | \varphi_{-1} \rangle$  for the detection coil along the  $x$ -axis,  $\theta = \frac{\pi}{2}$  and  $\phi = 0$ , becomes

$$\langle \varphi_1 | \mathbf{S}_x | \varphi_{-1} \rangle = \frac{\sqrt{2}}{2} C_{-1,0} (C_{1,-1} + C_{1,1})^* + C_{1,0}^* (C_{-1,-1} + C_{-1,1}) \quad (3.28)$$

We find  $\langle \varphi_1 | \mathbf{S}_x | \varphi_{-1} \rangle$  is strongly dependent upon the magnetic field strength, of order unity for low magnetic fields and of order 0.1 for high magnetic fields.

$|\langle \varphi_1 | \mathbf{I}_x | \varphi_{-1} \rangle|$  scales as  $\omega_0^{-1}$ ,  $R$  scales as  $\omega_0^{1/2}$  as discussed in Chapter 1, and therefore  $SNR_I$  scales as  $\omega_0^{3/4}$ . For force detection,  $SNR_F$  scales as  $\omega_0$  and we see that for samples with diameters of 50  $\mu\text{m}$  force-detection becomes superior for magnetic field strengths above  $8 \times 10^{-13}$  T, essentially in all cases. A similar analysis for the size dependence shows that for samples smaller than 500  $\mu\text{m}$ , force detection becomes the preferred method of detection.

## 3.4 Simulations

### 3.4.1 Electric Field Gradients

The electrostatic potentials and electric field gradients were calculated in GAMESS.[75] Accurate calculation of electric field gradients typically requires that at least double zeta basis sets be used as well as uncontracting the inner  $p$  and  $d$  functions.[76] The basis sets used in these simulations 6-311G\*\* at the MP2 level of theory. Even for the small organic molecules studied, converge took three days using a 2.7 GHz processor with 2GB of RAM.

The electrostatic potentials are shown for three molecules. Aminopyridine and a leucine-like molecule were recently shown to be components of tholins, a class of nitrogen containing compounds on Titan.[77] These molecules are thought to be progenitors for amino acids. Also included is a simulation on histidine. On these potential maps, red is the most negative and blue the most positive. The ordering is as follows: red < orange < yellow < green < blue.

	$V_{xx}$	$V_{yy}$	$V_{zz}$	$\eta$	$\nu_Q$ (MHz)
aminopyrdine-1	-0.04	-0.08	0.12	0.37	4.62
aminopyrdine-2	-0.21	-0.29	0.50	0.16	1.94
leucine-like	-0.22	-0.31	0.53	0.29	2.06
histidine-1	-0.37	-0.45	0.82	0.09	3.18
histidine-2	-0.13	-0.42	0.55	0.47	2.11
histidine-3	-0.36	-0.56	0.92	0.22	3.54

Table 3.2: Electric field gradient tensor elements, asymmetry parameters, and quadrupolar coupling constant.

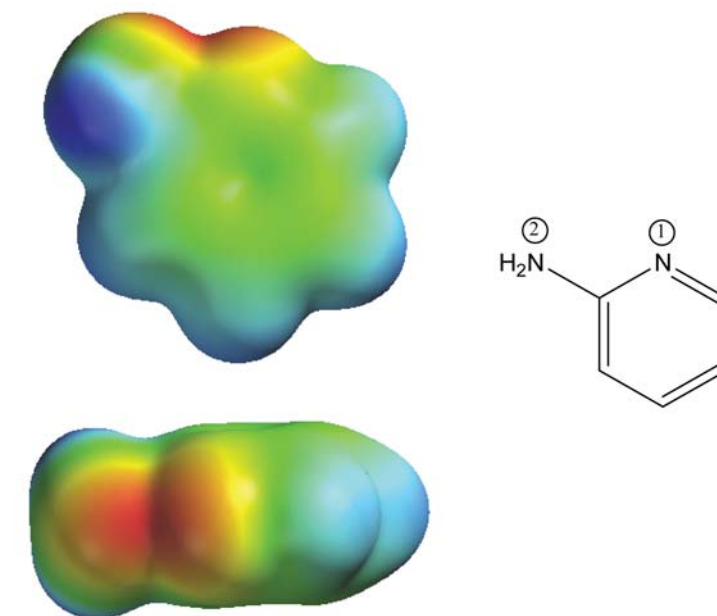


Figure 3.2: Electrostatic potential surfaces for aminopyridine.

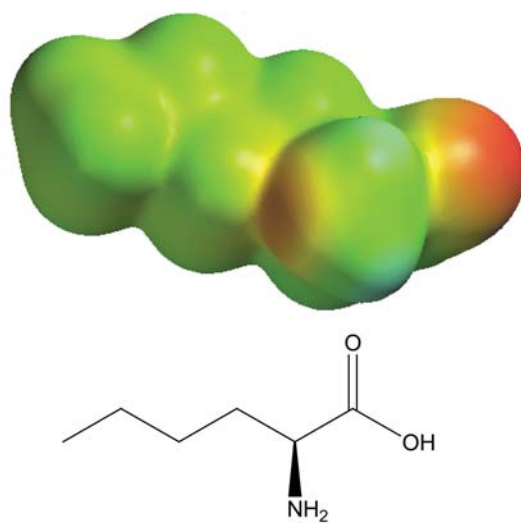


Figure 3.3: Electrostatic potential surfaces for leucine-like molecule.

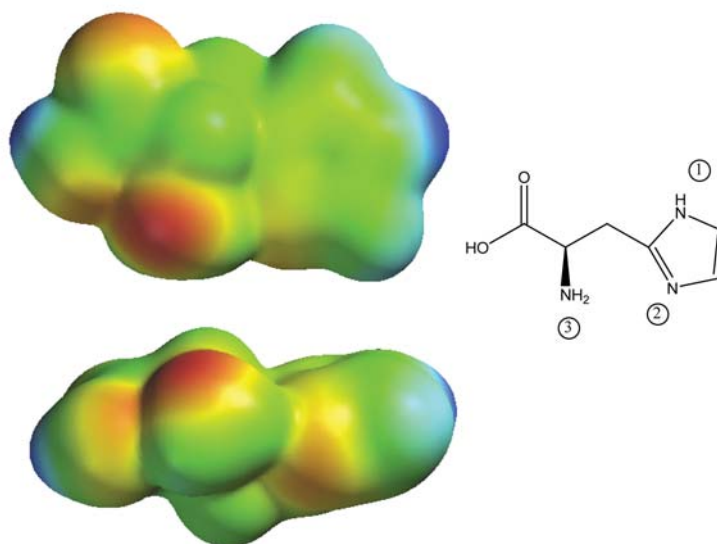


Figure 3.4: Electrostatic potential surfaces for histidine.

### 3.4.2 NMR Simulations

The first- and second-order quadrupolar transitions for the leucine-like molecule were simulated in GAMMA.[78] This simulation was done using the parameters in Table 3.2 and

assuming a 2 T magnetic field. We observe a reduction in linewidth of more than two orders of magnitude for the overtone spectrum.

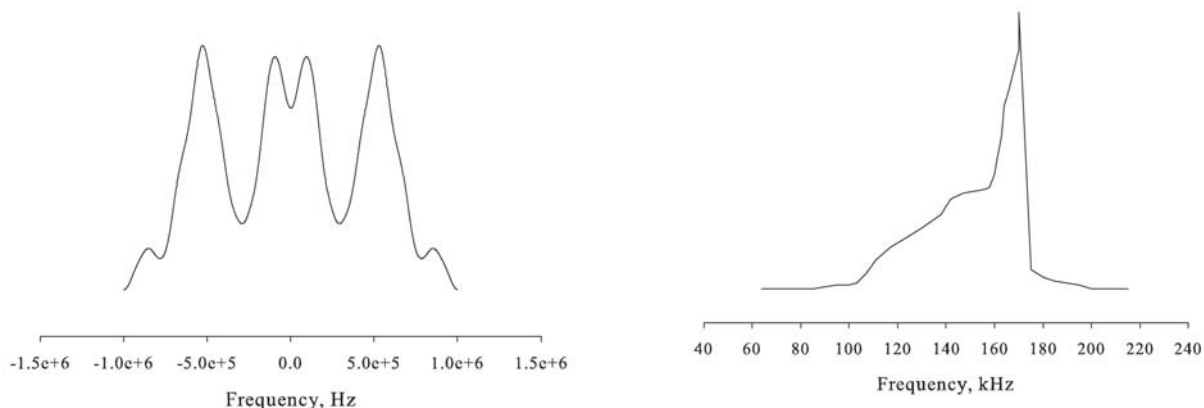


Figure 3.5: Calculated first-order quadrupole (left) and second-order quadrupole (right) spectrum for the leucine-like derivative. The overtone spectrum (right) has a line width over two orders of magnitude smaller than the first-order spectrum.

### 3.5 Conclusions

We have shown that detecting  $^{14}\text{N}$  overtone transitions by force-detection is favorable for over all magnetic field strengths and that the size scales of practical interest for in situ detection of  $^{14}\text{N}$  overtone transitions also significantly favor force detection. The removal of quadrupolar broadening by observing the overtone transition should allow for modest chemical identification, even for mixtures of compounds. Recently, density matrix methods were applied to overtone NMR for both static and rotating samples.[79] It will be of future interest to use these results along with observing other methods that include nonsecular terms in the Hamiltonian. Finally, composite pulse sequences may be utilized both for further line narrowing and for dealing with the very short nutation time of  $^{14}\text{N}$  nuclei.[80, 81]

## Appendix A

# Torsional BOOMERANG

### A.1 Introduction

As samples are scaled down to the sub-micron range, force-detection with longitudinal magnetization can become impractical. Fabrication of mechanical oscillator structures with flexural mode resonance frequencies in the audiofrequency range is a significant challenge, even with considerations of balancing the elastic and magnetic spring constants. Furthermore, this device would have Brownian motion large compared to its size. Therefore, in order to develop an appropriate spectrometer for nanoscale samples it will be necessary to detect transverse magnetization. This is shown schematically in Figure A.1.

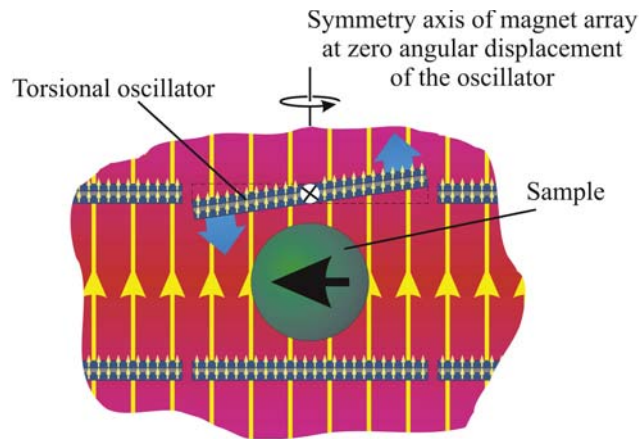


Figure A.1: Cross-sectional view showing a sample's spin magnetization precessing at the Larmor frequency via a dipole-dipole coupled torque to a cylindrical detector magnet suspended about a torsion axis.

The detection will be most sensitive for spin-locked magnetization, whereby the spin magnetization time is lengthened by setting it along  $\mathbf{B}_{eff}$  for a time  $T_{1\rho}$  while the  $B_1$  field

is on. After the  $B_1$  field is removed, the magnetization decays in a time of order the inverse line width. In this Appendix we will present a signal-to-noise analysis for this type of detection.

## A.2 Signal-to-Noise

The detector oscillates (librates) in response to a torque from the sample magnetization, which we take to be a single proton moment  $\mu = 1.41 \times 10^{-26} \text{ J T}^{-1}$ . The configuration for the maximum torque is shown below. The magnetization of the detector is along the  $z$ -axis. The sample moment precesses about the  $z$ -axis, exerting a torque on the detector at the Larmor frequency or the frequency of the spin-lock field.

The total torque is

$$\mathbf{N} = \int \int \mathbf{s} \times d\mathbf{F} \quad (\text{A.1})$$

where  $d\mathbf{F}$  is the force on an element of surface current on the magnet, and  $\mathbf{s}$  is the vector connecting the axis to the element, which is perpendicular to the axis. The surface current is that current that gives the same field outside the magnet as the magnetization of the detector

$$\mathbf{J} = \mathbf{M} \times \hat{\mathbf{n}} = M(\hat{\mathbf{z}} \times \hat{\mathbf{n}}). \quad (\text{A.2})$$

No volume or current density is required for the problem if we assume  $\nabla \times \mathbf{M} = 0$ , i.e. the magnetization is uniform. Also, since  $\mathbf{M} \times \hat{\mathbf{n}} = 0$  on the top and bottom, only the round sides contribute to the torque. The Lorentz force on the current element is

$$d\mathbf{F} = \mathbf{J} \times \mathbf{B} d\sigma \quad (\text{A.3})$$

where  $\mathbf{B}$  is the signal field and  $d\sigma$  is the area of the element.

Consider the geometric illustration below. Let  $\mathbf{s}$  denote the moment arm of the surface current element  $d\sigma$ .  $\mathbf{s} = -\zeta\hat{\mathbf{z}} + a \cos\phi\hat{\mathbf{x}}$  where  $\zeta$  is the distance from the top of the sensor,  $\phi$  is the azimuthal angle of the position of  $d\sigma$  and is measured from the  $x$ -axis. The sample points along the  $x$ -axis and the rotation axis of the detector is the  $y$ -axis. Let  $z$  denote the  $z$ -coordinate of  $d\sigma$  with respect to the sample as the origin. Let  $\mathbf{r}$  denote the position of  $d\sigma$  with respect to the origin. We will denote  $r_d$  as the detector radius,  $h_d$  as its height,

and  $R$  as the distance of closest approach of the sensor to the sample dipole.

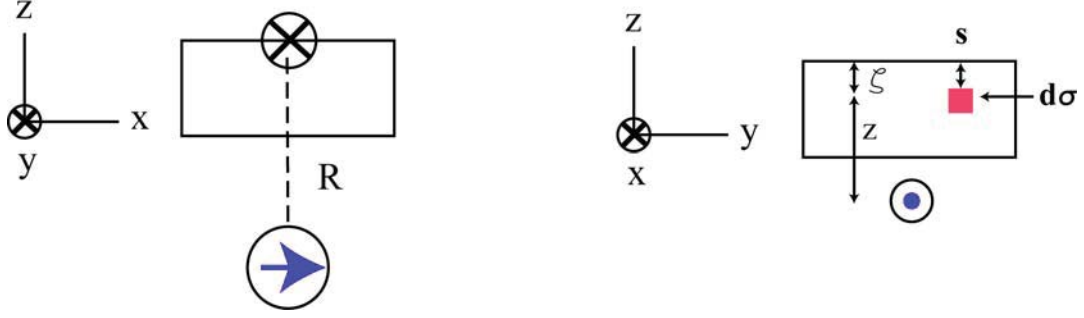


Figure A.2: Side views of torque-based detector showing relevant geometric parameters.

At position  $\mathbf{r}$  in the field of the sample dipole

$$\mathbf{B} = \frac{\mu_0}{4\pi} \boldsymbol{\mu} \cdot \frac{(3\hat{\mathbf{r}}\hat{\mathbf{r}} - 1)}{r^3} = \frac{\mu_0}{4\pi} \mathbf{x} \cdot \frac{(3\hat{\mathbf{r}}\hat{\mathbf{r}} - 1)}{r^3} \quad (\text{A.4})$$

so

$$\begin{aligned} \mathbf{N} &= \int_0^{h_d} d\zeta \int_0^{2\pi} d\phi r_d \mathbf{s} \times \mathbf{F} = \int_0^b d\zeta \int_0^{2\pi} d\phi r_d (-\zeta \hat{\mathbf{z}} + r_d \cos \phi \hat{\mathbf{x}}) \times \mathbf{F} \\ &= \int_0^{h_d} d\zeta \int_0^{2\pi} d\phi r_d (-\zeta \hat{\mathbf{z}} + r_d \cos \phi \hat{\mathbf{x}}) \times (\mathbf{J} \times \mathbf{B}) \\ &= \int_0^{h_d} d\zeta \int_0^{2\pi} d\phi r_d (-\zeta \hat{\mathbf{z}} + r_d \cos \phi \hat{\mathbf{x}}) \times \left[ \mathbf{M} (\hat{\mathbf{z}} \times \hat{\mathbf{n}}) \times \left( \frac{\mu_0}{4\pi} \mathbf{x} \cdot \frac{(3\hat{\mathbf{r}}\hat{\mathbf{r}} - 1)}{r^3} \right) \right] \\ &= \frac{\mu_0 \mu M r_d}{4\pi} \int_0^{h_d} d\zeta \int_0^{2\pi} d\phi r_d (-\zeta \hat{\mathbf{z}} + r_d \cos \phi \hat{\mathbf{x}}) \\ &\quad \times \left[ (\hat{\mathbf{y}} \cos \phi - \hat{\mathbf{x}} \sin \phi) \times \frac{3r_d \cos \phi \hat{\mathbf{r}} - r \hat{\mathbf{x}}}{r^4} \right]. \end{aligned} \quad (\text{A.5})$$

Equation (A.5) can then be further simplified to give

$$\mathbf{N} = \frac{\mu_0 \mu M}{4} \mathbf{y} \left[ \frac{1}{\sqrt{z^2 + r_d^2}} \left( 2z + (R + h_d) \frac{r_d^2}{z^2 + r_d^2} \right) \right]_R^{R+h_d} \quad (\text{A.6})$$

where  $z = R + h_d - \zeta$ . The torque expression in equation (A.6) is expression for the signal.

We can express equation A.6 in terms of scaled coordinates  $\tilde{h} = h_d/R$ ,  $\tilde{r} = r_d/R$ , and

$$\tilde{z} = z/R$$

$$\mathbf{N} = \frac{\mu_0 \mu M}{4} \mathbf{y} \left[ \frac{1}{\sqrt{\tilde{z}^2 + \tilde{r}^2}} \left( 2\tilde{z} + (1 + \tilde{h}) \frac{\tilde{r}^2}{\tilde{z}^2 + \tilde{r}^2} \right) \right]_1^{1+\tilde{h}}. \quad (\text{A.7})$$

The noise is considered by evaluating the moment of inertia about the torsion axis.

$$\mathbf{N}_{noise} = \mathbf{y} \sqrt{4k_B T \alpha_\theta \Delta \nu} \quad (\text{A.8})$$

where  $\alpha_\theta = I\gamma$  with damping parameter  $\gamma$  and moment of inertia  $I$ .

$$\begin{aligned} \frac{I}{\eta} &= \int \int \int \rho d\phi d\rho dz s^2 \\ &= \int \int \int \rho^3 \cos^2 \phi d\rho d\phi dz + \int \int \int \rho z^2 d\rho d\phi dz \\ &= 2\pi \int \int z^2 \rho d\rho dz + \pi \int \rho^3 d\rho dz \\ &= \pi^2 r_d^2 \frac{1}{3} h_d^3 + \pi h_d \frac{1}{4} r_d^4 \end{aligned} \quad (\text{A.9})$$

where  $\eta$  is the density of the detector magnet. The moment of inertia  $I$  is conveniently expressed as

$$I = \eta \pi r_d^2 h_d \left( \frac{1}{3} h_d^2 + \frac{1}{4} r_d^2 \right) \quad (\text{A.10})$$

which can be reexpressed as

$$I = \eta \pi R^5 \left[ r_d^2 h_d \left( \frac{\tilde{h}^2}{3} + \frac{\tilde{r}^2}{4} \right) \right] \quad (\text{A.11})$$

and

$$\mathbf{N}_{noise} = \mathbf{y} \sqrt{4k_B T \eta \pi R^5 \Delta \nu} \left[ r_d^2 h_d \left( \frac{\tilde{h}^2}{3} + \frac{\tilde{r}^2}{4} \right) \right]^{1/2}. \quad (\text{A.12})$$

For a detector with saturation magnetization  $2 \text{ T}/\mu_0$ , with density  $\eta = 7800 \text{ kg}/\text{m}^3$ , a damping time of 1 s, a bandwidth of 1 Hz, and a radius  $R$  of we observe that the optimally sized detector has a radius of  $1.52R$  and height of  $0.26R$ . A contour plot is shown below.

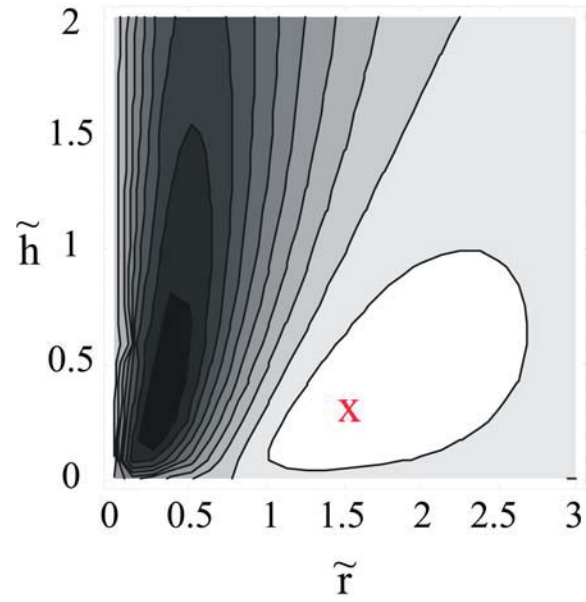


Figure A.3: Signal-to-noise contour plot for torque-detected NMR as a function of scaled height and radius. The global maximum is marked by an “ $x$ .”

# References

- [1] F. Bloch, W. W. Hansen, and M. Packard, “The nuclear induction experiment,” *Physical Review*, vol. 69, pp. 474–485, 1946.
- [2] I. I. Rabi, J. R. Zacharias, S. Millman, and P. Kusch, “A new method of measuring nuclear magnetic moments,” *Physical Review*, vol. 69, p. 318, 1938.
- [3] M. Bloom and K. Erdman, “Transverse Stern-Gerlach experiment,” *Canadian Journal of Physics*, vol. 40, pp. 179–193, 1962.
- [4] M. Bloom, E. Enga, and H. Lew, “Observation of transverse Stern-Gerlach effect in neutral potassium,” *Canadian Journal of Physics*, vol. 45, pp. 1481–1495, 1967.
- [5] P. J. Pizarro and D. P. Weitekamp, “Magnetic resonance of trapped ions by spin-dependent cyclotron acceleration,” *Bulletin of Magnetic Resonance*, vol. 14, pp. 220–223, 1992.
- [6] G. Alzetta and A. Gozzini, “Mechanical effect due to magnetic resonance,” *Annales de Physique*, vol. 8, p. 510, 1963.
- [7] G. Alzetta, E. Arimondo, C. Ascoli, and A. Gozzini, “Paramagnetic resonance experiments at low fields with angular-momentum detection,” *Nuovo Cimento B*, vol. 52, pp. 392–402, 1967.
- [8] J. A. Sidles, “Folded Stern-Gerlach experiment as a means for detecting nuclear magnetic resonance in individual nuclei,” *Physical Review Letters*, vol. 68, pp. 1124–1127, 1992.
- [9] J. A. Sidles and D. Rugar, “Signal-to-noise ratios in inductive and mechanical detection of magnetic resonance,” *Physical Review Letters*, vol. 70, pp. 3506–3509, 1993.

- [10] D. Rugar, O. Zuger, S. Hoen, C. S. Yannoni, H. M. Vieth, and R. D. Kendrick, “Force detection of nuclear magnetic resonance,” *Science*, vol. 264, pp. 1560–1563, 1994.
- [11] J. A. Sidles, J. L. Garbini, K. J. Bruland, D. Rugar, O. Zuger, S. Hoen, and C. S. Yannoni, “Magnetic resonance force microscopy,” *Reviews of Modern Physics*, vol. 67, pp. 249–265, 1995.
- [12] M. M. Midzor, P. E. Wigen, D. Pelekhov, W. Chen, P. C. Hammel, and M. L. Roukes, “Imaging mechanisms of force detected FMR microscopy,” *Journal of Applied Physics*, vol. 87, pp. 6493–6495, 2000.
- [13] D. Rugar, R. Budakian, H. J. Mamin, and B. W. Chui, “Single spin detection by magnetic resonance force microscopy,” *Nature*, vol. 430, pp. 329–332, 2004.
- [14] P. J. Carson, L. A. Madsen, G. M. Leskowitz, and D. P. Weitekamp, “Method for suppressing noise in measurements,” U.S. Patent No. 6,081,119, 2000.
- [15] G. M. Leskowitz, L. A. Madsen, and D. P. Weitekamp, “Force-detected magnetic resonance without field gradients,” *Solid State Nuclear Magnetic Resonance*, vol. 11, pp. 73–86, 1998.
- [16] L. A. Madsen, G. M. Leskowitz, and D. P. Weitekamp, “Observation of force-detected nuclear magnetic resonance in a homogeneous field,” *Proceedings of the National Academy of Sciences*, vol. 101, pp. 12 804–12 808, 2004.
- [17] C. W. McCombie, “Fluctuation theory in physical measurements,” *Reports on Progress in Physics*, vol. 16, pp. 266–320, 1953.
- [18] G. M. Leskowitz, “Force-Detected Nuclear Magnetic Resonance Independent of Field Gradients,” Ph.D. Thesis, California Institute of Technology, 2003.
- [19] D. I. Hoult and R. E. Richards, “Signal-to-noise ratio of nuclear magnetic resonance experiment,” *Journal of Magnetic Resonance*, vol. 24, pp. 71–85, 1976.
- [20] D. L. Olson, T. L. Peck, A. G. Webb, R. L. Magin, and J. V. Sweedler, “High-resolution microcoil H-1 NMR for mass-limited, nanoliter-volume samples,” *Science*, vol. 270, pp. 1967–1970, 1995.

- [21] K. R. Minard and R. A. Wind, “Solenoidal microcoil design. Part II: Optimizing winding parameters for maximum signal-to-noise performance,” *Concepts In Magnetic Resonance*, vol. 13, pp. 190–210, 2001.
- [22] B. M. Lambert, “Ph.D. Candidacy Report, California Institute of Technology,” 1999.
- [23] I. Babuska and T. Strouboulis, *The Finite Element Method and its Reliability*. London, UK: Oxford University Press, 2001.
- [24] J. D. Jackson, *Classical Electrodynamics*, 3rd ed. New York, NY: John Wiley and Sons, 1999.
- [25] M. Saito, N. Ishiwata, and K. Ohashi, “Evaluation of the crystal structure, film properties, and  $B_s$  of electroplated CoNiFe films,” *Journal of the Electrochemical Society*, vol. 149, pp. C642–C647, 2002.
- [26] T. Miyazaki, T. Oomori, F. Sato, and S. Ishio, “Zero magnetostriction composition in Fe-Ni-Co ternary alloy system,” *Journal of Magnetism and Magnetic Materials*, vol. 129, pp. L135–L136, 1994.
- [27] S. H. Liao, “High moment CoFe thin-films by electrodeposition,” *IEEE Transactions on Magnetics*, vol. 23, pp. 2981–2983, 1987.
- [28] H. J. Cho, S. Bhansali, and C. H. Ahn, “Electroplated thick permanent magnet arrays with controlled direction of magnetization for MEMS application,” *Journal of Applied Physics*, vol. 87, pp. 6340–6342, 2000.
- [29] K. Noguchi, S. Araki, T. Chou, D. Miyauchi, Y. Honda, A. Kamijima, O. Shinoura, and Y. Narumiya, “Linearity and hysteresis in the magnetoresistive response of (NiFe,NiFeCo)/Cu and Co/Cu/NiFe multilayers in patterned stripes,” *Journal of Applied Physics*, vol. 75, pp. 6379–6381, 1994.
- [30] L. A. Madsen, “Force-Detected NMR in a Homogeneous Field: Experiment Design, Apparatus, and Observations,” Ph.D. Thesis, California Institute of Technology, 2002.
- [31] M. G. Abele, *Structures of Pemanent Magnets*. New York, NY: John Wiley and Sons, Inc., 1993.

- [32] M. G. Abele and J. H. Jensen, “Hybrid pole pieces for permanent magnets,” *Journal of Applied Physics*, vol. 79, pp. 5199–5201, 1996.
- [33] K. Pawluk and Z. Zycki, “The working state of cone-shaped permanent magnets determined by boundary-integral approach,” *COMPEL: The International Journal for Computation and Mathematics*, vol. 19, pp. 632–638, 2000.
- [34] K. Halbach, “Design of permanent multipole magnets with oriented rare-earth cobalt material,” *Nuclear Instruments and Methods*, vol. 169, pp. 1–10, 1980.
- [35] G. Moresi and R. Magin, “Miniature permanent magnet for table-top NMR,” *Concepts in Magnetic Resonance Part B: Magnetic Resonance Engineering*, vol. 19B, pp. 35–43, 2003.
- [36] M. Kumada, E. I. Antokhin, Y. Iwashita, M. Aoki, and E. Sugiyama, “Super strong permanent dipole magnet,” *IEEE Transactions on Applied Superconductivity*, vol. 14, pp. 1287–1289, 2004.
- [37] H. Raich and P. Blumler, “Design and construction of a dipolar halbach array with a homogeneous field from identical bar magnets: NMR mandhalas,” *Concepts in Magnetic Resonance Part B: Magnetic Resonance Engineering*, vol. 23B, pp. 16–25, 2004.
- [38] *Properties of Silicon*. New York, NY: INSPEC, The Institution of Electrical Engineers, 1994.
- [39] W. D. Pilkey, *Stress, Strain, and Structural Matrices*. New York, NY: John Wiley and Sons, Inc., 1994.
- [40] D. Hyman and M. Mehregany, “Contact physics of gold microcontacts for MEMS switches,” *IEEE Transactions of Computer Packing Technology*, vol. 22, pp. 357–364, 1999.
- [41] F. R. Blom, S. Bouwstra, M. Elwenspoek, and J. H. J. Fluitman, “Dependence on the quality factor of micromachined silicon resonators on pressure and geometry,” *Journal of Vacuum Science and Technology B*, vol. 10, pp. 19–26, 1992.
- [42] C. Zener, “Internal friction in solids II. General theory of thermoelastic internal friction,” *Physical Review*, vol. 53, pp. 90–99, 1938.

- [43] C. Zener, W. Otis, and R. Nuckolls, “Internal friction in solids III. Experimental demonstration of thermoelastic internal friction,” *Physical Review*, vol. 53, pp. 100–101, 1938.
- [44] R. Lifshitz and M. L. Roukes, “Thermoelastic damping in micro- and nanomechanical systems,” *Physical Review B*, vol. 61, pp. 5600–5609, 2000.
- [45] H. Hosaka, K. Itao, and S. Kuroda, “Damping characteristics of beam-shaped micro-oscillators,” *Sensors and Actuators A*, vol. 49, pp. 87–95, 1995.
- [46] K. Y. Yasumura, T. D. Stowe, E. M. Chow, T. Pfafman, T. W. Kenny, B. C. Stipe, and D. Rugar, “Quality factors in micron- and submicron-thick cantilevers,” *Journal of Microelectromechanical Systems*, vol. 9, pp. 117–125, 2000.
- [47] H. Takao and M. Ishida, “An analytical model for support loss in micromachined beam resonators with in-plane flexural vibrations,” *Sensors and Actuators A*, vol. 12, pp. 497–505, 2003.
- [48] M. Garwood and L. Delabarre, “The return of the frequency sweep: Designing adiabatic pulses for contemporary NMR,” *Journal of Magnetic Resonance*, vol. 153, pp. 155–177, 2001.
- [49] C. J. Hardy and W. A. Edelstein, “Tailoring broadband inversion with efficient adiabatic fast passage,” *Journal of Magnetic Resonance*, vol. 69, pp. 196–199, 1986.
- [50] C. J. Hardy, W. A. Edelstein, and D. Vatis, “Efficient adiabatic fast passage for NMR population inversion in the presence of radiofrequency field inhomogeneity and frequency offsets,” *Journal of Magnetic Resonance*, vol. 66, pp. 470–482, 1986.
- [51] K. R. Minard and R. A. Wind, “Solenoidal microcoil design. Part I: Optimizing rf homogeneity and coil dimensions,” *Concepts in Magnetic Resonance*, pp. 128–142, 2001.
- [52] A. Han, M. Graff, O. Wang, and A. B. Fraizer, “An approach to multilayer microfluidic systems with integrated electrical, optical, and mechanical functionality,” *IEEE Sensors Journal*, vol. 5, pp. 82–89, 2005.

- [53] D. C. S. Bien, N. S. J. Mitchell, and H. S. Gamble, "Fabrication and characterization of a novel microvalve for microfluidic applications," *Journal of Microlithography Microfabrication and Microsystems*, vol. 3, pp. 486–492, 2004.
- [54] D. Roberts, H. Li, J. Steyn, O. Yaglioglu, S. M. Spearing, M. A. Schmidt, and N. W. Hagood, "A piezoelectric microvalve for compact high-frequency, high-differential pressure hydraulic micropumping systems," *Journal of Microelectromechanical Systems*, vol. 12, pp. 81–92, 2003.
- [55] J. Voldman, M. L. Gray, and M. A. Schmidt, "An integrated liquid mixer/valve," *Journal of Microelectromechanical Systems*, vol. 9, pp. 295–302, 2000.
- [56] C. S. Yih, *Fluid Mechanics: A Concise Introduction to the Theory*, 3rd ed. Ann Arbor, MI: West River Press, 1988.
- [57] D. Rugar, H. J. Mamin, R. Erlandsson, J. E. Stern, and B. D. Terris, "Force microscope using a fiber-optic displacement sensor," *Review of Scientific Instruments*, vol. 59, pp. 2337–2340, 1988.
- [58] B. M. Lambert, "Force-Detected, Single Molecule Spectroscopy and Imaging Using Nanoscale Mechanical Resonators," Ph.D. Thesis, California Institute of Technology, 2005.
- [59] D. Rugar and P. Grutter, "Mechanical parametric amplification and thermomechanical noise squeezing," *Physical Review Letters*, vol. 67, pp. 699–702, 1991.
- [60] K.-W. Jo, M.-S. Kim, J. H. Lee, E.-K. Kim, and K.-H. Park, "Optical characteristics of a self-aligned microlens fabricated on the sidewall of a 45 degree-angled optical fiber," *IEEE Photonics Technology Letters*, vol. 16, pp. 138–140, 2004.
- [61] J. Zhang, M. B. Chan-Park, and S. R. Conner, "Effect of exposure dose on the replication fidelity and profile of very high aspect ratio microchannels in SU-8," *Lab on a Chip*, vol. 4, no. 6, pp. 646–653, 2004.
- [62] C. K. Malek and V. Saile, "Applications of LIGA technology to precision manufacturing of high-aspect-ratio micro-components and -systems: a review," *Microelectronics Journal*, vol. 35, no. 2, pp. 131–143, 2004.

- [63] T. Wang, A. B. Mccandless, R. M. Lienau, K. W. Kelly, D. Hensley, Y. Desta, and Z. G. Ling, “Fabrication of monolithic multilevel high-aspect-ratio ferromagnetic devices,” *Journal of Microelectromechanical Systems*, vol. 14, no. 2, pp. 400–409, 2005.
- [64] J. A. Harley and T. W. Kenny, “High-sensitivity piezoresistive cantilevers under 1000 angstroms thick,” *Applied Physics Letters*, vol. 75, pp. 289–291, 1999.
- [65] B. R. Schiffer, A. Burstein, and W. J. Kaiser, “An active charge cancellation system for switched-capacitor sensor interface circuits,” *IEEE Journal of Solid-State Circuits*, vol. 33, pp. 2134–2138, 1998.
- [66] I. Baratin, E. B. Myers, J. Arlett, B. Gudlewski, and M. L. Roukes, “Sensitive detection of nanomechanical motion using piezoresistive signal downmixing,” *Applied Physics Letters*, vol. 86, p. 133109, 2005.
- [67] A. Yariv, *Quantum Electronics*, 3rd ed. New York, NY: John Wiley and Sons, 1989.
- [68] C. Baxter, M. Babiker, and R. Loudon, “Canonical approach to photon pressure,” *Physical Review A*, vol. 47, pp. 1278–1287, 1993.
- [69] G. S. May and S. M. Sze, *Fundamentals of Semiconductor Fabrication*. New York, NY: John Wiley and Sons, 2004.
- [70] R. Maboudian, “Surface processes in MEMS technology,” *Surface Science Reports*, vol. 30, pp. 209–270, 1998.
- [71] M. P. de Boer and T. M. Mayer, “Tribology of MEMS,” *MRS Bulletin*, vol. 26, pp. 302–304, 2001.
- [72] R. Tycko, P. L. Stewart, and S. J. Opella, “Peptide plane orientations determined by fundamental and overtone N-14 nmr,” *Journal Of The American Chemical Society*, vol. 108, pp. 5419–5425, 1986.
- [73] R. Tycko and S. J. Opella, “High-resolution N-14 overtone spectroscopy - an approach to natural abundance nitrogen nmr of oriented and polycrystalline systems,” *Journal Of The American Chemical Society*, vol. 108, pp. 3531–3532, 1986.
- [74] —, “Overtone nmr-spectroscopy,” *Journal Of Chemical Physics*, vol. 86, pp. 1761–1774, 1987.

- [75] M. W. Schmidt, K. K. Baldridge, J. A. Boatz, S. T. Elbert, M. S. Gordon, J. H. Jensen, S. Koseki, N. Matsunaga, K. A. Nguyen, S. J. Su, T. L. Windus, M. Dupuis, and J. A. Montgomery, "General atomic and molecular electronic-structure system," *Journal Of Computational Chemistry*, vol. 14, pp. 1347–1363, 1993.
- [76] W A Goddard III, "personal communication."
- [77] R. Hodyss, G. McDonald, N. Sarker, M. A. Smith, P. A. Beauchamp, and J. L. Beauchamp, "Fluorescence spectra of Titan tholins: in-situ detection of astrobiologically interesting areas on Titan's surface," *Icarus*, vol. 171, pp. 525–530, 2004.
- [78] S. A. Smith, T. O. Levante, B. H. Meier, and R. R. Ernst, "Computer-simulations in magnetic-resonance - an object-oriented programming approach," *Journal Of Magnetic Resonance Series A*, vol. 106, pp. 75–105, 1994.
- [79] L. Marinelli, S. Wi, and L. Frydman, "A density matrix description of N-14 overtone nuclear magnetic resonance in static and spinning solids," *Journal Of Chemical Physics*, vol. 110, pp. 3100–3112, 1999.
- [80] D. K. Lee and A. Ramamoorthy, "Cross-polarization in N-14 overtone NMR spectroscopy of solids," *Chemical Physics Letters*, vol. 286, pp. 398–402, 1998.
- [81] —, "Off-resonance proton-decoupling in overtone NMR spectroscopy of solids," *Chemical Physics Letters*, vol. 286, pp. 403–407, 1998.